ADSORPTION EQUILIBRIUM AND MASS TRANSFER IN METAL-ORGANIC FRAMEWORKS AND ADSORPTION ON CARBON SURFACES IN THE HENRY'S LAW REGION

by

Jian Liu

Dissertation
Submitted to the Faculty of the
Graduate School of Vanderbilt University
in partial fulfillment of the requirements
for the degree of

DOCTOR OF PHILOSOPHY

in

Chemical Engineering

May, 2011
Nashville, Tennessee

Approved:

M. Douglas LeVan

G. Kane Jennings

Peter N. Pintauro

Kenneth A. Debelak

Sandra J. Rosenthal

To Qian & Alvin

ACKNOWLEDGEMENTS

I would like to give my deepest gratitude to my adviser, Prof. M. Douglas LeVan, for his patience, guidance, encouragement, and tremendous support during my Ph.D. degree studies. His professionalism and curious attitude toward science nourished and inspired me through my scientific exploration at Vanderbilt University. I really appreciate his patience when helping me with my mistakes and his encouragement toward my progress. He is my scientific idol as well as a gentleman.

I want to thank all of the members of my Ph.D. committee and the staff in the Department of Chemical and Biomolecular Engineering for helping me and improving my graduate school experience. Thanks to Margarita, Mary, Susan, Rae, and Mark for helping me with all the documents and every order that I placed. I am also grateful to all of the members of the LeVan group for their company, help, and memorable friendships. Yu Wang, Bryan Schindler, Grant Glover, Joe Moate, Amanda Furtado, Timothy Giesy, and Lucas Mitchell are names and faces that I will never forget.

I gratefully acknowledge the U.S. Department of Energy and the National Energy Technology Laboratory for providing funds for this research (Award No. DE-FC26-07NT43092). In addition, I want to thank all the project collaborators from UOP, Northwestern University, University of Michigan, and the University of Edinburgh. I appreciate their friendly sharing and helpful suggestions during those over 20 teleconferences.

Finally, I want to thank my parents for their unconditional and endless love. It would be impossible for me to accomplish my dream without their support. They raised me up to be more than I can be. I also thank my wife and my son for sharing happiness and woe with me. I own them a lot more than what I can give. There is always a hidden chapter of love to them in my dissertation and in my heart.

TABLE OF CONTENTS

DEDICATION v

ACKNOWLEDGEMENTS vi

LIST OF TABLES xi

LIST OF FIGURES xvi

Chapter

I. INTRODUCTION 1

II. SCREENING MOF CANDIDATES FOR CO_2 ADSORPTION AT SUB-ATMOSPHERIC PRESSURES 10

- 2.1 Introduction 10
- 2.2 Experimental Section 11
- 2.3 Results and Discussion 12
  - Mg/DOBDC case study 12
  - Screening MOF candidates 17
- 2.4 Conclusions 24

III. CO_2 ADSORPTION RATE STUDY FOR MOF PELLETS USING THE CONCENTRATION SWING FREQUENCY RESPONSE METHOD . 27

- 3.1 Introduction 27
- 3.2 FR Model and Theory 28
- 3.3 Apparatus and Procedures 32
- 3.4 Results and Discussion 34
- 3.5 Conclusions 38
- References 39

IV. H_2O ADSORPTION AND SIMULATED FLUE GAS CONDITIONING EFFECTS ON CO_2 ADSORPTION IN MOFS 41

- 4.1 Introduction 41
- 4.2 Synthesis 42
- 4.3 Adsorption Equilibrium and Conditioning Apparatus 43
- 4.4 Pure CO_2 and H_2O Isotherms 49

4.5 H_2O effect on CO_2 adsorption 53
4.6 Simulated Flue Gas Conditioning 60
4.7 Conclusions 64
References 65

V. ISOSTERIC HEATS OF ADSORPTION IN THE HENRY'S LAW RE GION FOR CARBON SINGLE WALL CYLINDRICAL NANOPORES AND SPHEREICAL NANOCAVITIES 69
5.1 Introduction 69
5.2 Theory 71
5.3 Results and Discussion 75
    Cylindrical carbon nanopore 77
    Spherical carbon nanocavity 81
    LJ parameter effects 84
    External wall potential 87
    Geometrical effects 90
5.4 Conclusions 94

VI. HENRY'S LAW CONSTANTS AND ISOSTERIC HEATS OF ADSORP TION AT ZERO LOADING FOR MULTI-WALL CARBON SURFACES WITH DIFFERENT GEOMETRIES 98
6.1 Introduction 98
6.2 Theory 100
6.3 Results and Discussion 103
    Pore width and curvature dependence of Henry's law constant 103
    Isosteric heats of adsorption for multi-wall carbon surfaces 110
6.4 Conclusions 119
6.5 Appendix 120

VII. ACCESSIBLE VOLUME FOR ADSORPTION IN CARBON NANOPORES OF DIFFERENT GEOMETRIES AND WALL THICKNESSES 129
7.1 Introduction 129
7.2 Theory 130
7.3 Results and Discussion 134
    Accessible pore space for pores with single layer walls 134
    Effect of number of wall layers on the accessible pore space 139
7.4 Conclusions 145

VIII. CONCLUSIONS AND RECOMMENDATIONS 149

Appendix

A. STABILITY OF MG/DOBDC AND NI/DOBDC 155
  A.1 Steaming effects 155
  A.2 Aging effects 158

Appendix

B. PYRIDINE MODIFICATION OF NI/DOBDC 162
  B.1 Pyridine modification and sample characterization 162
  B.2 Water and carbon dioxide adsorption for pyridine-modified Ni/DOBDC 163

LIST OF TABLES

2.1 Summary of regeneration conditions for adsorbents. 15

2.2 Isosteric heats of adsorption for Mg/DOBDC powder at different loadings 17

2.3 Summary of CO_2 capacity and average isosteric heat of adsorption results at 100 °F and 0.1 atm CO_2 for adsorbents. 22

3.1 Summary of the diffusivity parameters for MOF pellets with different thicknesses. 37

5.1 Model parameters for different molecules. 77

5.2 Isosteric heat of adsorption in the Henry's law region for cylindrical carbon nanopores. 80

5.3 Isosteric heat of adsorption in the Henry's law region for spherical carbon nanocavities. 83

5.4 Empirical constant relationships between pore diameter for maximum and zero $q^{\mathrm{o}}_{\mathrm{st}}$ for different geometries. 84

6.1 Henry's law constants for single wall and multi-wall carbon surfaces. . . 109

6.2 Isosteric heats of adsorption at zero loading for multi-wall carbon surfaces. 118

7.1 LJ parameters and surface carbon number densities for different geometries. 130

7.2 Limiting dimensionless inaccessible pore spaces for pores with different geometries and numbers of wall layers. Values are $(R_2 - R_1)/\sigma_{\mathrm{sf}}$. 144

A.1 Steaming effects on CO_2 adsorption in DOBDC series MOFs 155

B.1 BET surface areas and porosities for Ni/DOBDC and pyridine-modified Ni/DOBDC 163

LIST OF FIGURES

2.1 Schematic diagram of Cahn gravimetric system for pure CO_2 isotherm measurements. 13

2.2 Schematic diagram of Rubotherm gravimetric system for pure CO_2 isotherm measurements. 14

2.3 Gravimetric CO_2 capacities for Mg/DOBDC powder at different temperatures. Data points are shown. Curves are multi-temperature Toth equation fits. 16

2.4 Isosteres of CO_2 adsorption by Mg/DOBDC powder at different loadings. Points have been interpolated from Fig. 2.3, and the lines are linear fit. . 18

2.5 Summary of the CO_2 capacities at the POI for all samples that we have considered (s denotes steamed; p denotes powder; pt denotes pellet; s p denotes steamed powder; s pt denotes steamed pellet). 20

2.6 Summary of the average isosteric heats of adsorption for all samples that we have considered (s denotes steamed; p denotes powder; pt denotes pellet; s p denotes steamed powder; s pt denotes steamed pellet). 21

2.7 CO_2 isotherms for DOBDC-series MOFs at 100 °F based on per metal atom. 23

3.1 Schematic diagram of the mass balance in a FR system. 30

3.2 CSFR system for CO_2 adsorption rate study. 33

3.3 Frequency response results for HKUST-1 pellets with different thicknesses. The pellets are labeled as Cu-1, Cu-2, and Cu-3 in the order of increasing thickness. 35

3.4 Frequency response results for Ni/DOBDC pellets with different thicknesses. The pellets are labeled as Ni-1, Ni-2, and Ni-3 in the order of increasing thickness. 36

4.1 Scanning electron microscope (SEM) images for the MOF samples. (a) HKUST-1; (b) Ni/DOBDC. 44

4.2 Volumetric system for CO_2/H_2O adsorption equilibrium measurement. . 46

4.3 H_2O loadings during the CO_2 adsorption equilibrium measurement for HKUST-1 pellet. The three dashed lines are horizontal. 47

4.4 Simulated flue gas conditioning apparatus. 48

4.5 CO_2 isotherms at 25 °C for MOF and zeolite pellets. Curves are multi-temperature Toth equation fits. Zeolite results are taken from reference [17]. 50

4.6 H_2O isotherms at 25 °C for MOF pellets. (a) HKUST-1 pellet; Kusgens et al.,[8] Yazaydin et al.[9] (b) Ni/DOBDC pellet. Lines are guides for the eyes. 52

4.7 CO_2 isotherms at 25 °C and high pressure for HKUST-1 and Ni/DOBDC samples. 54

4.8 CO_2 isotherms at 25 °C for HKUST-1 pellet with different H_2O loadings. Curves are multi-temperature Toth equation fits. 56

4.9 CO_2 isotherms at 25 °C for Ni/DOBDC pellet with different H_2O loadings. Curves are multi-temperature Toth equation fits. 57

4.10 CO_2 isotherms at 25 °C for Mg/DOBDC pellet with different H_2O loadings. Curves are multi-temperature Toth equation fits. 58

4.11 H_2O effects on CO_2 adsorption for MOF and zeolite pellets at 25 °C. Data points are CO_2 capacities at 0.1 atm for different samples at various H_2O loadings and lines are guides for the eyes. Zeolite results are taken from reference [26]. 59

4.12 CO_2 isotherms at 25 °C for MOF samples at different stages. (a) HKUST-1 pellet; (b) Ni/DOBDC pellet. Lines are guides for the eyes. 61

4.13 CO_2 isotherms at 25 °C for HKUST-1 pellet before and after different simulated flue gas conditionings. 62

4.14 CO_2 isotherms at 25 °C for Ni/DOBDC pellet before and after different simulated flue gas conditionings. 63

5.1 Diagrams of carbon nanopore and nanocavity. (a) Cylindrical pore; (b) Spherical cavity. 74

5.2 Surface number density of SWNT determined from graphite sheet. . . . 76

5.3 Isosteric heat of adsorption as a function of pore width and dimensionless pore diameter in cylindrical carbon nanopore. (a) pore width results; (b) dimensionless pore diameter results. 79

5.4 Isosteric heat of adsorption as a function of pore width and dimensionless pore diameter in spherical carbon nanocavity. (a) pore width results; (b) dimensionless pore diameter results. 82

5.5 The effect of LJ parameters on the pore diameter for the maximum $q_{\mathrm{st}}^{\mathrm{o}}$ for the three geometries. σ_{sf} increases from 2.9 Å to 5.0 Å (top to bottom) for each geometry. 85

5.6 Three possible results for the superposition of LJ potentials. 88

5.7 External wall potentials at the center of pores as functions of dimensionless pore diameters for all six gas molecules in a cylindrical nanopore. 91

5.8 Isosteric heats of adsorption of argon in three different geometries. . . . 92

6.1 Henry's law constant as a function of pore width for Ar adsorbed in single wall cylindrical carbon nanopores at different temperatures. T = 70, 100, 150, 200, 250, 300, 350, 400, 450, 500, 600, 700, 800 K, increasing in the positive z direction. 104

6.2 Van't Hoff plots for Ar adsorbed in single wall cylindrical carbon nanopores with different pore widths. 106

6.3 Van't Hoff plots for N_2 adsorbed in 5.0 Å multi-wall cylindrical carbon nanopores with different layers of walls. 107

6.4 Henry's law constants for Ar adsorbed on single wall carbon surfaces with different geometries at 298.15 K. 108

6.5 Isosteric heats of adsorption as a function of pore width for Ar adsorbed in multi-wall slit-shaped carbon nanopores at room temperature. Results obtained by using Steele's 10-4-3 potential are included for comparison. The inserted figure is a magnified image. The curves are labeled from top to bottom. 114

6.6 Isosteric heats of adsorption as a function of pore width for Ar adsorbed in multi-wall cylindrical carbon nanopores at room temperature. The inserted figure is a magnified image. The curves are labeled from top to bottom. 115

6.7 Isosteric heats of adsorption as a function of pore width for Ar adsorbed in multi-wall spherical carbon nanopores at room temperature. The inserted figure is a magnified image. The curves are labeled from top to bottom. 116

6.8 The contributions to the total maximum isosteric heats of adsorption from different layer of walls for Ar adsorbed on multi-wall carbon surfaces. (a) slit-shaped geometry; (b) cylindrical geometry; (c) spherical geometry. . 117

6.9 Positions of surfaces where zero solid-fluid potentials occur for gas molecules adsorbed in single layer carbon pores with different geometries. 122

6.10 Difference between the Henry's law constants obtained by using accessible void volume and absolute void volume for Ar adsorbed in single wall carbon cylindrical nanopores with different geometries and pore widths. 123

7.1 Schematic for definition of accessible pore radius. 133

7.2 Inaccessible pore space for Ar adsorbed on graphene and in pores with slit-shaped, cylindrical, and spherical geometries as a function of pore diameter. 135

7.3 Effect of reducing pore radius on accessible volume for slit-shaped pores. Left: walls far apart, $R_2 - R_1 = 0.8584\,\sigma_{\mathrm{sf}}$. Middle: wall B attracting, $R_2 - R_1 < 0.8584\,\sigma_{\mathrm{sf}}$. Right: tightest accessible pore, $R_2 - R_1 = 0.8584\,\sigma_{\mathrm{sf}}$. 138

7.4 Inaccessible pore space for slit-shaped pores with multilayered walls. . . 141

7.5 Inaccessible pore space for cylindrical pores with multilayered walls. . . . 142

7.6 Inaccessible pore space for spherical pores with multilayered walls. . . . 143

A.1 CO_2 isotherms at 100 °F for Ni/DOBDC powder before and after 5% steaming for 4h. 156

A.2 CO_2 isotherms at 100 °F for Mg/DOBDC powder before and after 5% steaming for 4h. 157

A.3 CO_2 isotherms at 100 °F for fresh Ni/DOBDC powder and aged sample. 159

A.4 CO_2 isotherms at 100 °F for fresh Mg/DOBDC powder and aged sample. 160

B.1 CO_2 isotherms at 25 °C for Ni/DOBDC and pyridine-modified Ni/DOBDC. 164

B.2 H_2O isotherms at 25 °C for Ni/DOBDC and pyridine-modified Ni/DOBDC. 165

B.3 CO_2 isotherms at 25 °C for pyridine-modified Ni/DOBDC with different amount of preloaded water. 167

CHAPTER I

INTRODUCTION

The global climate change phenomenon, which is caused mainly by the discharge of CO_2 into the atmosphere, has attracted more and more attention.[1,2] Some research results reveal that the concentration of CO_2 in the atmosphere has increased from about 310 ppm to over 380 ppm during the last half century.[3]

According to a report from the U.S. Department of State,[4] the total annual amount of U.S. CO_2 emissions will increase by 17 percent every year between 2000 and 2020 to an absolute level of 6,843 million tons. The estimated level of U.S. CO_2 emissions from fossil fuel combustion for the year 2020 is 6,447 million tons. Of this total amount, about 94% is from the combustion of carbon-based fossil fuels.[5] Moreover, the energy requirement is increasing every day both in the United States and in other countries. Therefore, we can expect the amount of CO_2 emissions to keep increasing in the near future. The U.S. Department of Energy (DOE) issued a carbon sequestration program in 2009 aiming to achieve 90% CO_2 capture at an increase in the cost of electricity of no more than 35% by 2020.[6]

Many techniques have been adopted to try to resolve the CO_2 emission issue. The main methods include strategies of separating and sequestering CO_2 into oceans, terrestrial ecosystems, or geologic formations and capturing CO_2 from energy systems.[7] The separation methods are relatively more mature and more economical than the sequestration strategies considering the relatively lower cost of equipment and the recycling uses of captured CO_2.

The conventional way for removal of CO_2 from flue gas is to use some basic solid or solvent to capture the CO_2, which is a somewhat acidic gas. Hughes *et al.*[8] studied *in-situ* CO_2 capture using CaO to react with CO_2 at about 700 °C. The product $CaCO_3$ could be regenerated to CaO by providing heat from a secondary fuel. Obviously, this *in-situ* method will consume a huge amount of energy. Another commercial process to remove CO_2 is using monoethanoamine (MEA) solvent to absorb CO_2 gas. Low CO_2 capacity and high energy cost for the MEA solvent regeneration reflect the necessity of further improvement for this technology.[9] Yeh *et al.*[10] used aqueous ammonia instead of amine solvent to absorb CO_2 gas. The results showed this method saved about 60% of the energy required in the MEA method. However, the energy comsumption is still unsatisfactory and the byproduct ammonia bicarbonate has an uncertain market. Recently, some scientists used MCM-41 modified with polyethylenimine (PEI) as an adsorbent to capture CO_2 gas. Although this composite material has a higher CO_2 capacity than either the MCM-41 or PEI alone, the absolute CO_2 capacity of the composite material is still very low.[11] Moreover, it takes a long time to regenerate the composite material.

As discussed above, the acid-base chemical reactions between CO_2 and a solvent or solid do not make it easy to reuse the absorbents or the CO_2 gas after reaction. In contrast, physisorption between certain adsorbents and CO_2 could allow conveniently reversible processes to capture the CO_2 gas. The adsorbents can be repeatedly used after regeneration. Moreover, the CO_2 gas, which might be converted into fuel through solar energy according to one study,[12] can be stored and used as well.

A considerable amount of research has been done on separating CO_2 gas by using physisorption processes. Activated carbon, carbon molecular sieves, and zeolites have been extensively studied as adsorbents for CO_2 gas.[13–16] The common shortfalls for these traditional adsorbents are either low capacities or difficult regeneration processes.

It is clear that physisorption can be an effective and economical method to separate CO_2 from the flue gas of power plants. However, the key is to improve the

CO_2 capacities of the adsorbents and to make them easier to regenerate. Rather than limiting interest on modifying the traditional adsorbents, this dissertation focusses on exploring novel adsorbents to capture CO_2 from flue gas. The novel adsorbents should have large CO_2 capacities at sub-atmospheric pressures. The CO_2 adsorption processes should be reversible and should have fast rates. The novel adsorbents should also have repeatable performance and good selectivity toward CO_2 over other species in the flue gas.

Some results have indicated that metal-organic frameworks (MOFs) might become promising adsorbents for CO_2 separation.[17–21] Metal-organic frameworks, also known as coordination networks or coordination polymers, are novel materials constructed by coordinate bonds between multi-dentate ligands and metal atoms or small metal-containing clusters (referred to as secondary building units or SBU). Most of the MOF materials have 3D structures incorporating uniform pores and a network of channels. The integrity of these pores and channels can be retained after careful removal of the guest species that have filled them. The remaining voids within the 3D structures then can adsorb other guest molecules.[2] The structure of a typical MOF, Zn_4O $(O_2C\text{-}C_6H_4\text{-}CO_2)_3$, which is also known as IRMOF-1, is constructed with zinc atoms as metal centers and terephthalic acid molecules as ligands. The central cavity formed by the metal centers and ligands is much larger compared with other adsorbents and is essential for gas storage.[2]

Considerable effort has been expended on the synthesis of MOF materials in the last several years.[22,23] They are synthesized mainly by hydrothermal or solvothermal methods. The state of the art is in the choice of metal centers and design and synthesis of ligands. Different combinations of metal centers and ligands based on rational design ideas will generate MOF materials with various structures and properties. Besides large surface areas and pore volumes, many MOF materials are well known to have unsaturated metal centers (UMCs)[24,25] within their 3D structures which can offer extra binding sites to the guest molecules.[26,27]

In the part of this dissertation on MOF research, we will first identify some of the best MOF candidates that have the highest carbon dioxide capacities at our point of interest. Then, we will understand carbon dioxide adsorption kinetics and some important factors that may affect carbon dioxide adsorption, including preloaded water and coexisting acid gases. The first part of this dissertation, on MOF research, includes chapters 2 to 4.

Also as part of this dissertation, some thermodynamic properties of gas adsorption in carbon nanopores in the Henry's law region are calculated and compared for pores with different geometries and numbers of wall layers. Relationships are developed for the estimation of pore diameters where maximum isosteric heats of adsorption occur for gas molecules adsorbed in carbon nanopores. Number of wall layer effects and accessibility of pores are also investigated. The second part of this dissertation, on adsorption thermodynamic properties research, includes chapters 5 to 7.

The dissertation is organized as follows. In Chapter 2, we screen out several promising MOFs from about 30 candidates based on their carbon dioxide capacities at our point of interest (POI), which is 0.1 atm and 100 °F. The CO_2 partial pressure in flue gas is approximately 0.1 atm, and 100 °F (37.8 °C) represents a cooled flue gas. Average isosteric heats of adsorption are also obtained from the MOF's carbon dioxide isotherm data.

In Chapter 3, we use a concentration swing frequency response (CSFR) method to study carbon dioxide adsorption rates for two MOF candidates, HKUST-1 and Ni/DOBDC, which were selected based on the results in Chapter 2. Results for HKUST-1 and Ni/DOBDC pellets with different thicknesses are obtained and analyzed to proposed a mass transfer mechanism for carbon dioxide adsorption in these two MOFs.

In Chapter 4, we measure adsorption equilibrium for carbon dioxide, water vapor, and their mixture for HKUST-1, Ni/DOBDC, and Mg/DOBDC pellets and compare results with those for some benchmark zeolite pellets. The preloaded water effects on carbon dioxide adsorption for the three MOFs are studied and compared with NaX and 5A zeolites. Ni/DOBDC is proposed as a promising candidate for capturing carbon dioxide from flue gas because it can maintain a significant carbon dioxide capacity at moderate water loadings and has desirable stability properties.

In Chapter 5, we calculate the isosteric heats of adsorption for six gases adsorbed in carbon nanopores with slit-shaped, cylindrical, and spherical geometries in the Henry's law region. Maximum isosteric heats of adsorption are found at certain pore size for pores for all of the three geometries. General plots are generated to predict pore diameters at which maximum isosteric heats of adsorption occur for non-polar or weakly polar molecules adsorbed in carbon nanopores. Surface mean curvature is related to the isosteric heat of adsorption for gas molecules adsorbed in carbon nanopores.

In Chapter 6, we extend the study in the previous chapter to carbon nanopores with multilayer walls. A simple summation method is used to derive the external wall potentials for pores with multilayer walls based on the single layer external wall potential. Contributions to the maximum isosteric heat of adsorption from individual layers of wall are studied and compared. Henry's law constants are also calculated for several gas molecules and compared with results in the literature. An accessible pore volume is adopted to replace the absolute void volume in order to avoid negative Henry's law constant at high temperatures.

In Chapter 7, we investigate the accessible pore volume in gas adsorption. Accessible pore radius is calculated as a function of pore radius for gas adsorbed in carbon nanopores with different geometries and numbers of wall layers. A superposition effect is found that can help improve the accessibility of pores when reducing the pore radii. The different accessible pore radii found for pores with different geometries at fixed pore size is attributed to the different surface mean curvatures. The effect of number of wall layers on the accessible pore radius is studied as well.

In Chapter 8, we draw conclusions from this research and provide some recommendations for possible extensions of the current work.

In Appendix A, we present data on the hydrothermal stabilities of two MOFs in the DOBDC series. Carbon dioxide isotherms are compared for Ni/DOBDC and Mg/DOBDC samples before and after steaming and aging processes. Ni/DOBDC is found to be more stable than Mg/DOBDC although it has a smaller carbon dioxide capacity at 0.1 atm.

In Appendix B, we present data on the use of pyridine to modify the surface of Ni/DOBDC in order to reduce its hydrophilicity. Surface area and pore volume for the pyridine modified Ni/DOBDC is characterized, and the effects of pyridine modification on carbon dioxide and water adsorption in Ni/DOBDC are examined. The selectivity between water and carbon dioxide is calculated for pyridine modified Ni/DOBDC and compared with that of the unmodified Ni/DOBDC.

References

[1] Yang, H.Q.; Xu, Z.H.; Fan, M.H.; Gupta, R.; Slimane, R.B.; Bland, A.E.; Wright, I. Progress in Carbon Dioxide Separation and Capture: A Review. *J. Enviro. Sci.* **2008**, *20*, 14–27.

[2] *Acid Rain and Related Programs: 2006 Progress Report*, Enviromental Protection Agency, Washington, DC, United States, 2006

[3] Watts, R.G. *Global Warming and the Future of the Earth*, Chapter 2, Morgan & Claypool Publishers, 2007.

[4] Part 5: Projected Greenhouse Gas Emissions *The Fourth United States Climate Action Report.* U.S. Department of State, 2006

[5] *Inventory of U.S. Greenhouse Gas Emissions and Sinks: 1990-2006*, Enviromental Protection Agency, Washington, DC, United States, 2008

[6] Ciferno, J. P.; Fout, T. E.; Jones, A. P.; Murphy, J. T. Capturing Carbon from Existing Coal-Fired Power Plants. *Chem. Eng. Prog.* **2009**, *105*, 33–41.

[7] DOE/OS-FE. Carbon Sequestration. State of the Science. Office of Science and Office of Fossil Energy, U.S. Department of Energy, February 1999.

[8] Hughes, R.W.; Lu, D.Y.; Anthony, E.J.; Macchi, A. Design, Process Simulation and Construction of an Atmospheric Dual Fluidized Bed Combustion System for *in situ* CO_2 Capture Using High-Temperature Sorbents. *Fuel Process. Technol.* **2005**, *86*, 1523–1531.

[9] Yamasaki, A. An Overview of CO_2 Mitigation Options for Global Warming-Emphasizing CO_2 Sequestration Options. *J. Chem. Eng. Jpn.* **2003**, *36*, 361–375.

[10] Yeh, J.T.; Resnik, K.P.; Rygle, K.; Pennline, H.W. Semi-Batch Absorption and Regeneration Studies for CO_2 Capture by Aqueous Ammonia. *Fuel Process. Technol.* **2005**, *86*, 1533–1546.

[11] Xu, X.; Song, C.S.; Andresen, J.M.; Miller, B.G.; Scaroni, A.W. Novel Polyethyleneimine-Modified Mesoporous Molecular Sieve of MCM-41 Type as High-Capacity Adsorbent for CO_2 capture. *Energy & Fuels* **2002**, *16*, 1463–1469.

[12] Varghese, O. K.; Paulose, M.; LaTempa, T. J.; Grimes, C. A. High-Rate Solar Photocatalytic Conversion of CO_2 and Water Vapor to Hydrocarbon Fuels. *Nano. Lett.* **2009**, *9*, 731–737.

[13] Chue, K.T.; Kim, J.N.; Yoo, Y.J.; Cho, S.H.; Yang, R.T. Comparison of Activated Carbon and Zeolite 13X for CO_2 Recovery from Flue Gas by Pressure Swing Adsorption. *Ind. Eng. Chem. Res.* **1995**, *34*, 591–598.

[14] Soares, J.L.; Jos, H.J.; Moreira, R.F.P.M. Preparation of a Carbon Molecular Sieve and Application to Separation of N_2, O_2 and CO_2 in A Fixed Bed. *Braz. J. Chem. Eng.* **2003**, *20*, 75–80.

[15] IEA (International Energy Agency) Carbon Dioxide Capture from Power Stations, 1998. Available at www.ieagreen.org.uk/sr2p.htm.

[16] Diaz, E.; Munoz, E.; Vega, A.; Ordonez, S. Enhancement of the CO_2 Retention Capacity of X zeolites by Na- and Cs-treatments. *Chemosphere* **2008**, *70*, 1375–1382.

[17] Millward, A.R.; Yaghi, O.M. Metal-Organic Frameworks with Exceptionally High Capacity for Storage of Carbon Dioxide at Room Temperature. *J. Am. Chem. Soc.* **2005**, *127*, 17998–17999.

[18] Li, H.L.; Eddaoudi, M.; O'Keeffe, M.; Yaghi, O.M. Design and Synthesis of an Exceptionally Stable and Highly Porous Metal-Organic Framework. *Nature* **1999**, *402*, 276–279.

[19] Yang, Q. Y.; Xue, C. Y.; Zhong, C. L.; Chen, J. F. Molecular Simulation of Separation of CO_2 From Flue Gases in Cu-BTC Metal-Organic Framework. *AICHE J.* **2007**, *53*, 2832–2840.

[20] Arstad, B.; Fjellvag, H.; Kongshaug K. O.; Swang, O.; Blom, R. Amine Functionalised Metal Organic Frameworks (MOFs) as Adsorbents for Carbon Dioxide. *Adsorption* **2008**, *14*, 755-762.

[21] Vaidhyanathan, R.; Iremonger, S. S.; Dawson, K. W.; Shimizu, G. K. U. An Amine-Functionalized Metal Organic Framework for Preferential CO_2 Adsorption at Low Pressures. *Chem. Comm.* **2009**, *35*, 5230–5232.

[22] Eddaoudi, M.; Kim, J.; Rosi, N.L.; Vodak, D.; Wachter, J.; O'Keeffe, M.; Yaghi, O.M. Systematic Design of Pore Size and Functionality in Isoreticular MOFs and Their Application in Methane Storage. *Science* **2002**, *295*, 469–472.

[23] Rosi, N.L.; Eckert, J.; Eddaoudi, M.; Vodak, D.T.; Kim, J.; O'Keeffe, M.; Yaghi, O.M. Hydrogen Storage in Microporous Metal-Organic Frameworks. *Science* **2003**, *300*, 1127–1129.

[24] Babarao, R.; Jiang, J.W. Molecular Screening of Metal-Organic Frameworks for CO_2 Storage. *Langmuir*, **2008**, *24*, 6270–6278.

[25] Li, H.L.; Davis, C.E.; Groy, T.L.; Kelley, D.G.; Yaghi, O.M. Coordinatively Unsaturated Metal Centers in the Extended Porous Framework of $Zn_3(BDC)_3 \cdot 6CH_3OH$ (BDC=1,4-Benzenedicarboxylate). *J. Am. Chem. Soc.* **1998**, *120*, 2186–2187.

[26] Dietzel, P.D.C.; Morita Y.; Blom, R.; Fjellvag, H. An In Situ High-Temperature Single-Crystal Investigation of a Dehydrated Metal-Organic Framework Compound and Field-Induced Magnetization of One-Dimensional Metal Oxygen Chains. *Angew. Chem. Int. Ed.* **2005**, *44*, 6354–6358.

[27] Collins, D.J.; Zhou, H.C. Hydrogen Storage in Metal-Organic Frameworks. *J. Mater. Chem.* **2007**, *17*, 3154–3160.

CHAPTER II

SCREENING MOF CANDIDATES FOR CO_2 ADSORPTION AT SUB-ATMOSPHERIC PRESSURES

2.1 Introduction

MOF materials are widely regarded as promising candidates for applications in catalysis, separation, and gas storage because of their large surface areas and pore volumes. Compared with conventional microporous inorganic materials such as zeolites, MOF materials have more flexible and rational design possibilities through the control of metal centers and ligands.[1] Recently, research on the ability of MOF materials to support permanent porosity in the absence of solvent molecules has made significant progress.[2] This progress is leading MOF materials to practical applications as adsorbents.

Pure CO_2 adsorption equilibrium measurement on MOF materials is the most fundamental step for their application as CO_2 adsorbents. Given the large number of possible pairs of metal atoms and linkers, there is an almost unlimited number of MOFs that could be synthesized. Therefore, screening and understanding of the fundamental structure/function relationships are very important for CO_2 capture using MOFs.

Several studies have been published recently on CO_2 adsorption in MOFs. Millward *et al.*[3] studied saturated CO_2 capacities at room temperature and 42 bar for 10 MOF materials. Their saturated CO_2 capacities are generally larger than those of traditional zeolites mainly due to larger surface areas and pore volumes of the MOF materials. Dietzel *et al.*[4] studied CO_2 adsorption in Ni/DOBDC and found that CO_2 coordinated to unsaturated nickel sites gives rise to high CO_2 capacity at sub-atmospheric pressures and ambient temperatures. Liang *et al.*[5] investigated the potential of using CuBTC (HKUST-1) to selectively separate CO_2 from N_2 and CH_4. They obtained a four fold increase in working capacity for CO_2 adsorption in CuBTC compared to zeolite 13X over the same pressure range. In addition, they found that the selectivities of CO_2/N_2 and CO_2/CH_4 increased with an increase in pressures.

The CO_2 adsorption process in some MOF materials is fully reversible, which is desirable for pressure swing adsorption (PSA), a promising process that can be used to separate CO_2 from flue gases.[6] However, because the CO_2 partial pressures in flue gases are usually well below 1 bar,[7] it is of greater importance to understand CO_2 adsorption in MOF materials in the sub-atmospheric pressure region than at high pressures.

2.2 Experimental Section

MOF samples were synthesized through solvothermal methods by our collaborators at UOP, LLC (Des Plaines, Illinois) and the University of Michigan following procedures in the literature.[8] Metal salts and organic linkers were added to a solution composed of water and organic solvents at various ratios. The mixtures then were placed into either a glass jar or a Parr reactor and held for certain amounts of time at preset temperatures to produce different MOF samples. Before drying samples, solvent exchange procedures were usually conducted to help remove residual solvents and enhance surface areas of the MOFs.

Pure CO_2 adsorption equilibrium measurements were conducted using a gravimetric system, either a Cahn balance or a Rubotherm balance. The gravimetric method is a quite direct way to measure the adsorption equilibrium. The change of sample weight and the corresponding pressure are recorded to calculate the adsorption capacities. A schematic diagram of the Cahn system (Cahn D-200 balance, accuracy 0.01 mg) is shown in Fig. 2.1. A schematic diagram of the Rubotherm system (Rubotherm balance, accuracy 1 μg) is shown in Fig. 2.2. The Cahn system is operated manually and limited to sub-atmospheric pressure measurements. In contrast, the Rubotherm system is automated and able to measure adsorption equilibrium at high pressures due to its isolated electromagnetic balance system and stainless steel measuring cell.

CO_2 isotherms were measured at three different temperatures, 25 °C, 100 °F (37.8 °C), and 50 °C for about 30 MOFs. A point of interest (POI) of 0.1 atm, 100 °F was selected for CO_2 adsorption testing. Results of some zeolite samples have also been included for comparison purposes, even though these would not be effective for removing CO_2 from flue gas because of strong water adsorption.

All of the adsorbents were regenerated before isotherm measurements. The MOF samples were regenerated at preset temperatures which are typically set by stability considerations. The regeneration conditions are summarized in Table 2.1.

2.3 Results and Discussion

Mg/DOBDC case study

As an example, CO_2 isotherms at three different temperatures for Mg/DOBDC powder are displayed in Fig. 2.3. The isotherms are typical type I isotherms[9] which indicate strong interactions between the Mg/DOBDC structure and CO_2 molecules even in the sub-atmospheric pressure range. The CO_2 adsorption capacity at the POI is 4.93 mol/kg. A multi-temperature Toth equation fits the CO_2 isotherms in Fig. 2.3 very well.[10]

Isosteres were obtained from points interpolated from Fig. 2.3 and are displayed in Fig. 2.4. The isosteric heats of adsorption at different loadings were calculated and are summarized in Table 2.2. The average heat of adsorption is 51.6 kJ/mol. The CO_2 capacity at the POI for Mg/DOBDC powder is large, which can be ascribed to the unsaturated metal centers (UMCs) in its crystal structure.[11] The strong interactions between CO_2 molecules and the UMCs is consistent with the large

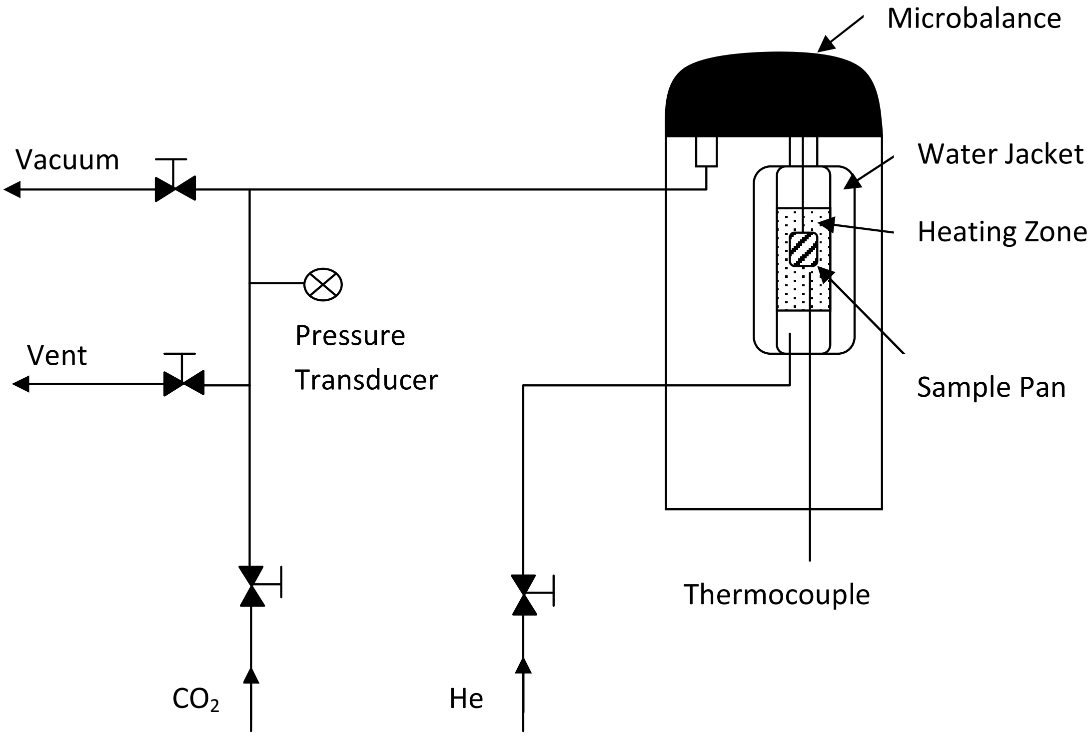

Figure 2.1: Schematic diagram of Cahn gravimetric system for pure CO_2 isotherm measurements.

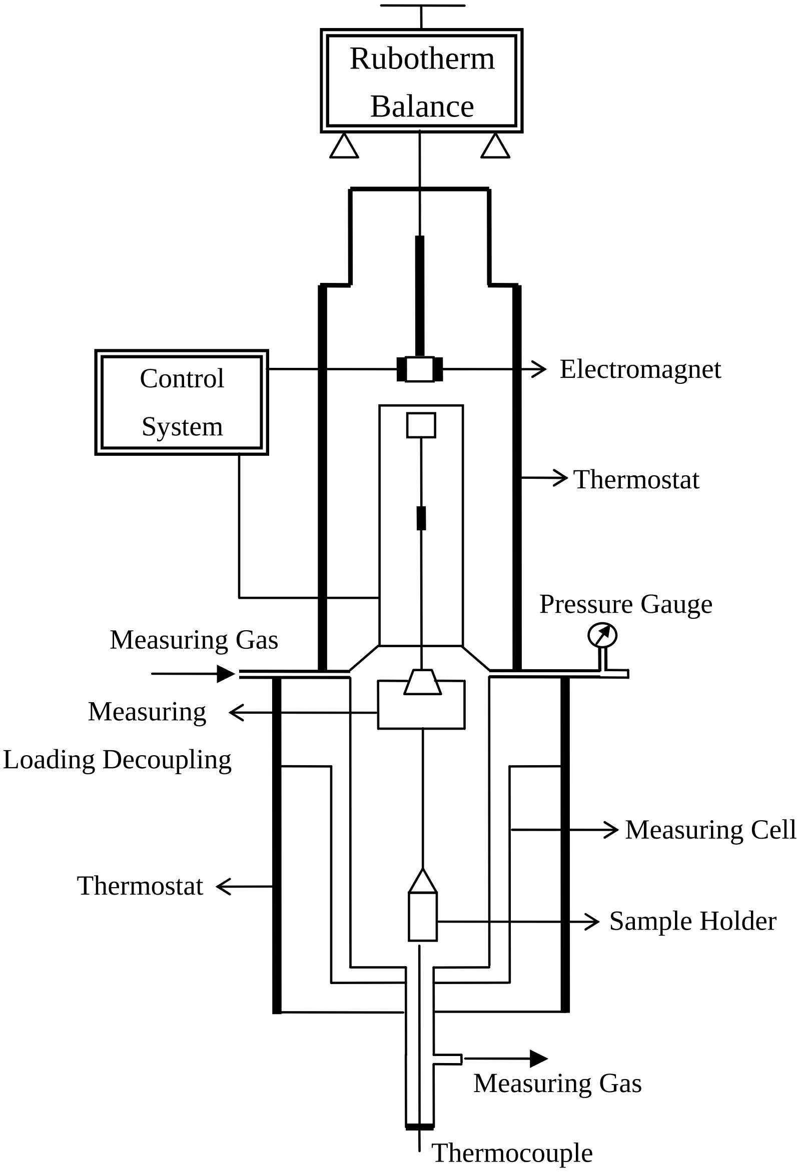

Figure 2.2: Schematic diagram of Rubotherm gravimetric system for pure CO_2 isotherm measurements.

Table 2.1: Summary of regeneration conditions for adsorbents.

Adsorbent	Regeneration Condition	System
Mg/DOBDC p	200 °C + high Vac (1×10^{-7} mbar), 12h	Rubotherm
Mg/DOBDC pt	200 °C + high Vac (1×10^{-7} mbar), 12h	Rubotherm
5A powder	400 °C + high Vac (1×10^{-7} mbar), 3h	Rubotherm
Ni/DOBDC p	150 °C + high Vac (1×10^{-7} mbar), 6h	Rubotherm
Ni/DOBDC extruded	150 °C + high Vac (1×10^{-7} mbar), 6h	Rubotherm
Ni/DOBDC s p	150 °C + high Vac (1×10^{-7} mbar), 6h	Rubotherm
Ni/DOBDC pt	150 °C + high Vac (1×10^{-7} mbar), 6h	Rubotherm
5A pellet	400 °C + high Vac (1×10^{-7} mbar), 3h	Rubotherm
Ni/DOBDC s pt	150 °C + high Vac (1×10^{-7} mbar), 6h	Rubotherm
Co/DOBDC	125 °C + high Vac (1×10^{-7} mbar), 6h	Rubotherm
Silicalite	400 °C + high Vac (1×10^{-7} mbar), 3h	Rubotherm
HKUST-1 (CuBTC)	150 °C + helium + Vac (1×10^{-4} mbar), 12h	Cahn
MOF-74 (Zn/DOBDC)	125 °C + helium + Vac (1×10^{-4} mbar), 12h	Cahn
Gold HKUST-1 pt	170 °C + high Vac (1×10^{-7} mbar), 8h	Rubotherm
HKUST-1 BASF	150 °C + high Vac (1×10^{-7} mbar), 8h	Rubotherm
Al-MIL-110	85 °C + high Vac (1×10^{-7} mbar), 5h	Rubotherm
MIL-101	200 °C + helium + Vac (1×10^{-4} mbar), 12h	Cahn
Tb-MOF-76	150 °C + high Vac (1×10^{-7} mbar), 5h	Rubotherm
Ga-MIL-68	150 °C + high Vac (1×10^{-7} mbar), 8h	Rubotherm
MIL-53 (cal)	125 °C + helium + Vac (1×10^{-4} mbar), 12h	Cahn
MIL-53	230 °C + helium + Vac (1×10^{-4} mbar), 12h	Cahn
Pt/Y-MOF	125 °C + helium + Vac (1×10^{-4} mbar), 12h	Cahn
IRMOF-1	200 °C + helium + Vac (1×10^{-4} mbar), 12h	Cahn
Zn BDC-DABCO	125 °C + high Vac (1×10^{-7} mbar), 6h	Rubotherm
ZIF-8-T	260 °C + helium + Vac (1×10^{-4} mbar), 12h	Cahn
ZIF-8-P	260 °C + helium + Vac (1×10^{-4} mbar), 12h	Cahn
La-PDA	125 °C + helium + Vac (1×10^{-4} mbar), 12h	Cahn
BAsolite Z1200	300 °C + high Vac (1×10^{-7} mbar), 8h	Rubotherm
UMCM-1	75 °C + high Vac (1×10^{-7} mbar), 5h	Rubotherm
Ni-bpe	85 °C + high Vac (1×10^{-7} mbar), 5h	Rubotherm
Ni-MAMS-1	200 °C + helium + Vac (1×10^{-4} mbar), 12h	Cahn

* s denotes steamed; p denotes powder; pt denotes pellet; s p denotes steamed powder; s pt denotes steamed pellet; cal denotes calcined; Vac denotes vacuum.

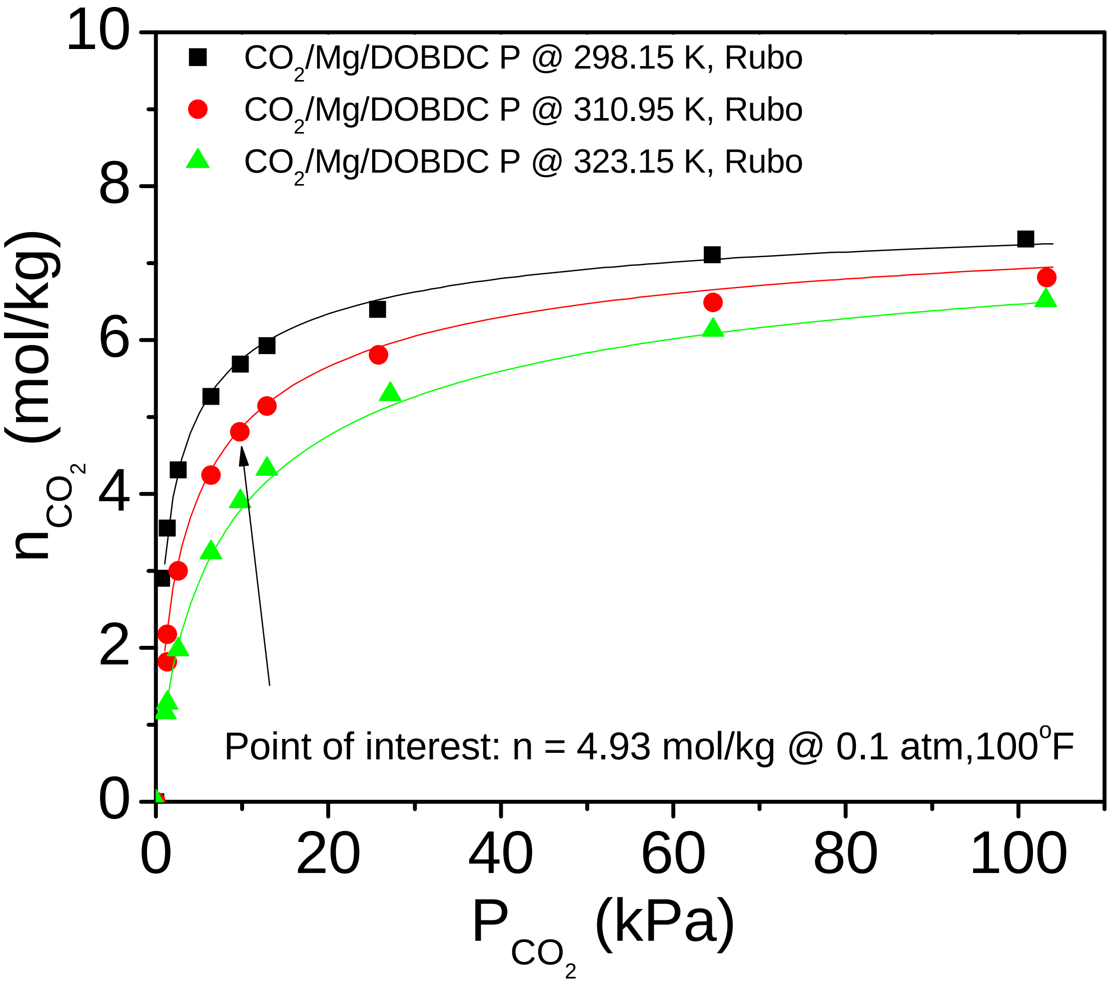

Figure 2.3: Gravimetric CO_2 capacities for Mg/DOBDC powder at different temperatures. Data points are shown. Curves are multi-temperature Toth equation fits.

Table 2.2: Isosteric heats of adsorption for Mg/DOBDC powder at different loadings

Sample	Loadings (mol/kg)			
	n = 4.0	n = 5.0	n = 6.0	Average
Mg/DOBDC p	53.24 kJ/mol	52.29 kJ/mol	49.33 kJ/mol	51.6 kJ/mol

* p denotes powder.

isosteric heat of adsorption. However, because of the less steep isotherm slope at low loadings, Mg/DOBDC can be regenerated at a much lower temperature than a conventional zeolite.

Screening MOF candidates

Following a similar procedure, we measured CO_2 isotherms at three different temperatures for all other MOF candidates. The results, including some results for zeolites, are summarized in a bar graph shown in Fig. 2.5. The MOF samples are sorted in decreasing order of their CO_2 capacities at the POI. We did not find any general correlation between the sequence of CO_2 capacities at the POI for the MOF samples and their surface areas or pore volumes.

The average isosteric heats of adsorption that were determined from the isotherm data are summarized in Fig. 2.6. The average heats of adsorption for the MOFs samples are found to follow a trend similar to the CO_2 capacities at the POI with some exceptions, such as Ni-bpe. Actually, some research has shown that the H_2 capacity of the IRMOF series materials can be correlated with the heat of adsorption at low pressure, the surface area at intermediate pressure, and the free volume at high pressure.[12]

CO_2 capacity and average isosteric heat of adsorption results for all the adsorbents at 0.1 atm CO_2, 100 °F are summarized in Table 2.3 in order of decreasing CO_2 capacity at the POI.

Our collaborators at Northwestern University used Monte Carlo molecular

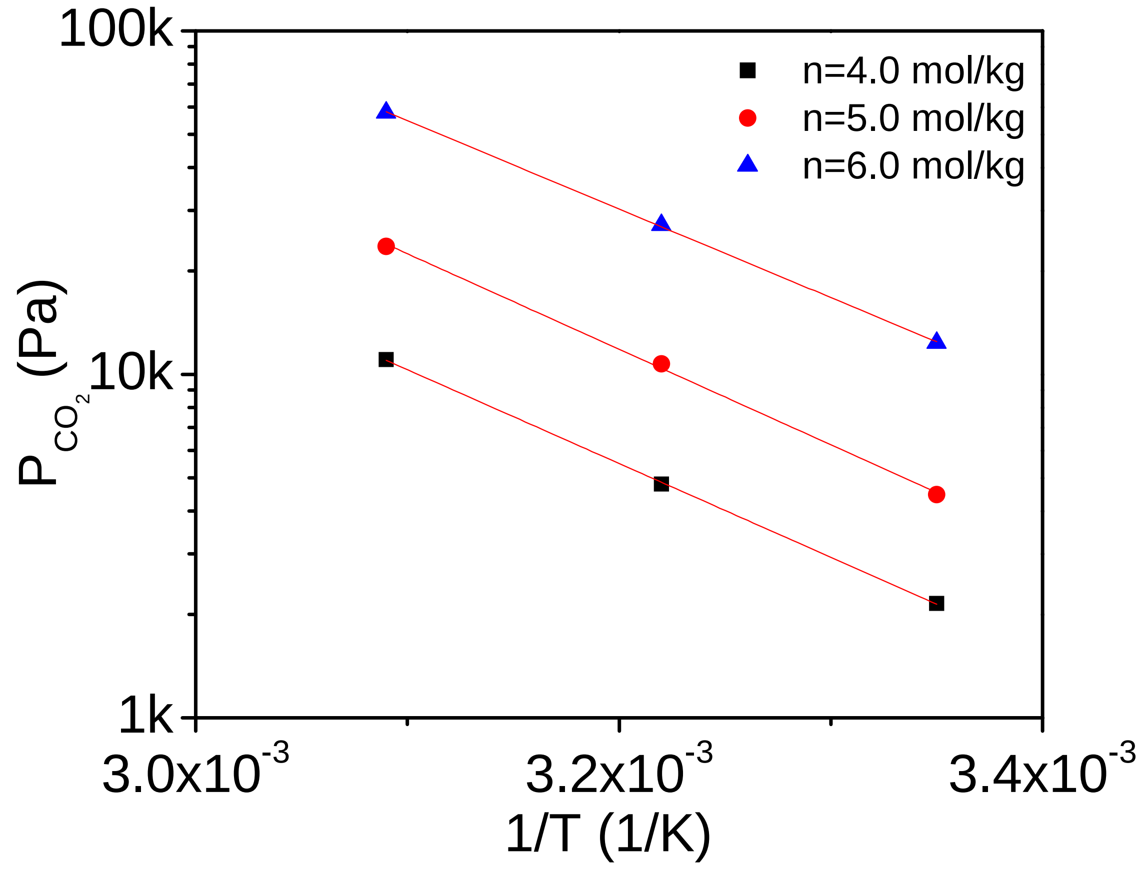

Figure 2.4: Isosteres of CO_2 adsorption by Mg/DOBDC powder at different loadings. Points have been interpolated from Fig. 2.3, and the lines are linear fit.

simulation to screen out the best MOF candidates for CO_2 adsorption in the low pressure region.[8] They used the MuSic code[13] to simulate CO_2 isotherms for many different MOFs. As expected, UMCs play a key role in CO_2 adsorption due to their coordination interactions with CO_2 molecules.

The DOBDC series of MOFs with UMCs are found to be the best MOF candidates for CO_2 adsorption in the low pressure range. The MOF structure units of the DOBDC series are constructed with metal centers (Zn, Ni, Co, Mg) and 2,5-dihydroxyterephthalic acid molecules. Both the aryloxide and carboxylate moieties in the 2,5-dihydroxyterephthalic acid molecules act as ligands to the metals. The DOBDC-series MOF structure units have 1D pores with a uniform pore size of 11 Å after the removal of solvent molecules.[14]

Based on the isotherm data, we found that the DOBDC-series MOFs with different metal centers have quite different CO_2 capacities at the POI. Metal substitution in the DOBDC series can impact the CO_2 capacity significantly.[11] In order to exclude the difference in molecular weights for different metal atoms, CO_2 isotherms for DOBDC-series MOFs are plotted in Fig. 2.7 based on per metal atom. It is clear that Mg/DOBDC has the highest per atom-based CO_2 capacity at the POI, which is about 0.58 CO_2 molecule. The per atom-based CO_2 capacities at the POI for Ni/DOBDC, Co/DOBDC, and Zn/DOBDC are 0.41, 0.29, and 0.07 CO_2 molecule, respectively. This metal substitution effect may be caused by the difference in the ionic character of the metal-oxide bonds in the DOBDC-series MOFs.[8,15]

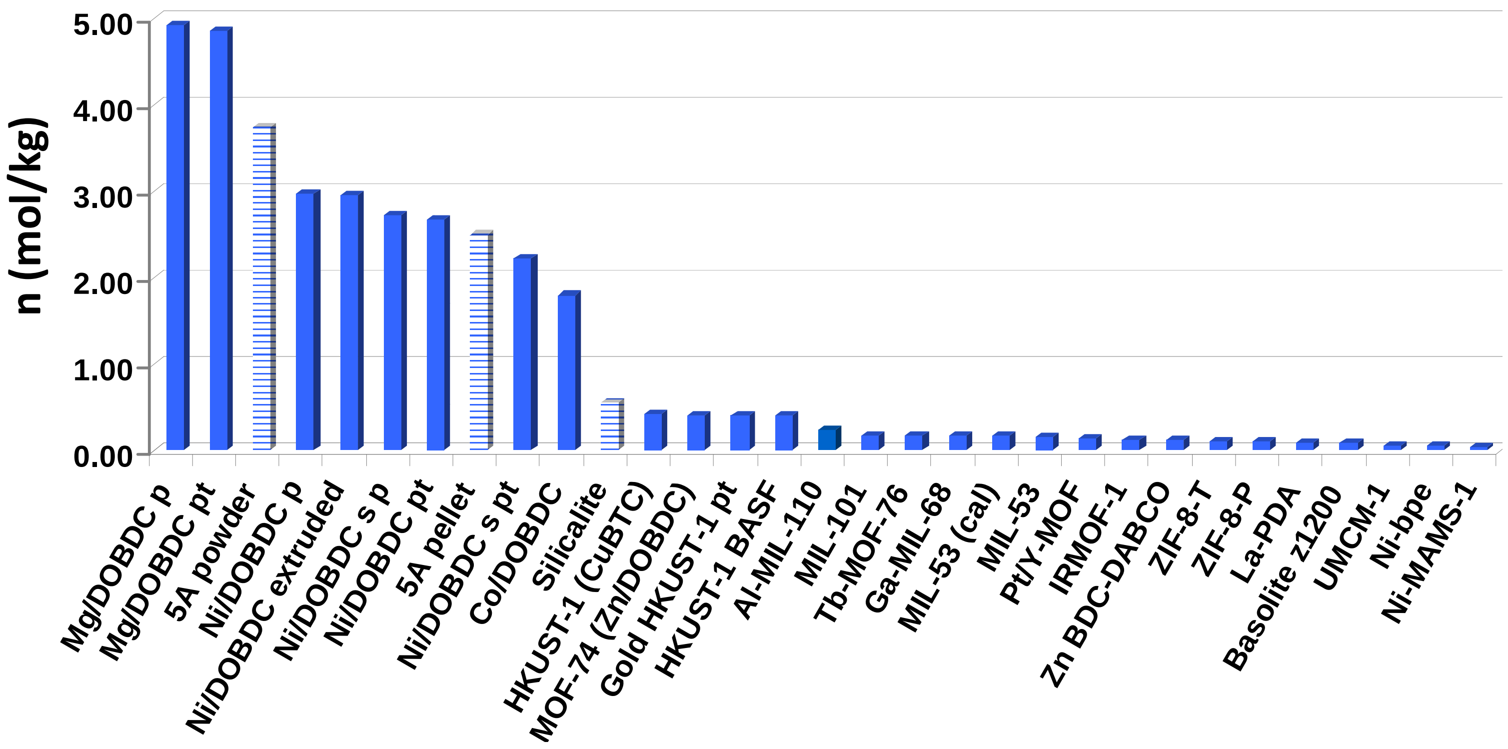

Figure 2.5: Summary of the CO_2 capacities at the POI for all samples that we have considered (s denotes steamed; p denotes powder; pt denotes pellet; s p denotes steamed powder; s pt denotes steamed pellet).

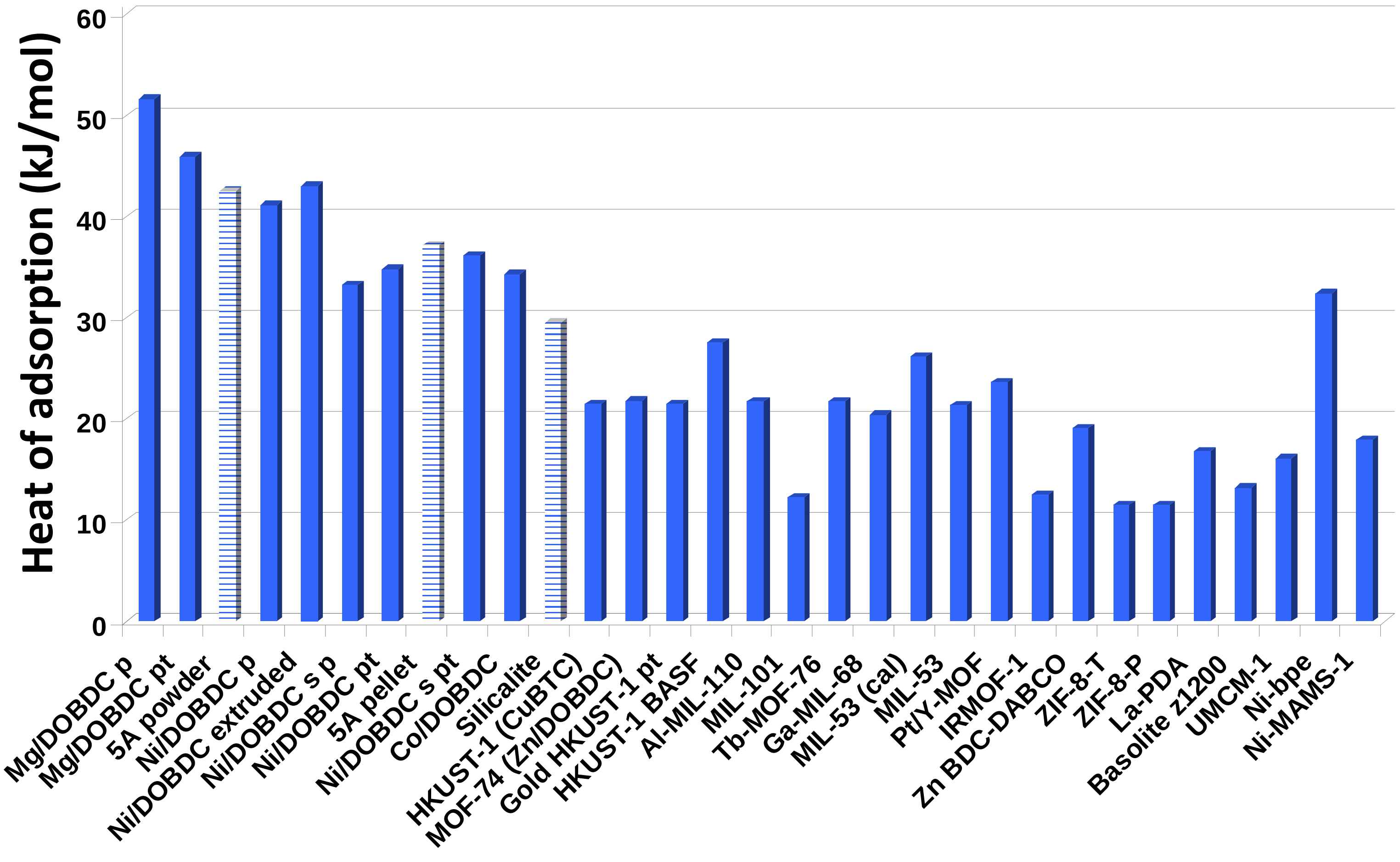

Figure 2.6: Summary of the average isosteric heats of adsorption for all samples that we have considered (s denotes steamed; p denotes powder; pt denotes pellet; s p denotes steamed powder; s pt denotes steamed pellet).

Table 2.3: Summary of CO_2 capacity and average isosteric heat of adsorption results at 100 °F and 0.1 atm CO_2 for adsorbents.

Adsorbent	Loading (mol/kg)	Average $-\Delta H$ (kJ/mol)	System
Mg/DOBDC p	4.93	51.6	Rubotherm
Mg/DOBDC pt	4.86	45.9	Rubotherm
5A powder	3.75	42.5	Rubotherm
Ni/DOBDC p	2.98	41.1	Rubotherm
Ni/DOBDC extruded	2.96	43.0	Rubotherm
Ni/DOBDC s p	2.73	33.2	Rubotherm
Ni/DOBDC pt	2.68	34.8	Rubotherm
5A pellet	2.50	37.1	Rubotherm
Ni/DOBDC s pt	2.23	36.1	Rubotherm
Co/DOBDC	1.80	34.3	Rubotherm
Silicalite	0.56	29.5	Rubotherm
HKUST-1 (CuBTC)	0.42	21.5	Cahn
MOF-74 (Zn/DOBDC)	0.41	21.8	Cahn
Gold HKUST-1 pt	0.40	21.5	Rubotherm
HKUST-1 BASF	0.40	27.5	Rubotherm
Al-MIL-110	0.24	21.7	Rubotherm
MIL-101	0.18	12.2	Cahn
Tb-MOF-76	0.18	21.7	Rubotherm
Ga-MIL-68	0.18	20.4	Rubotherm
MIL-53 (cal)	0.17	26.1	Cahn
MIL-53	0.15	21.3	Cahn
Pt/Y-MOF	0.14	23.6	Cahn
IRMOF-1	0.13	12.5	Cahn
Zn BDC-DABCO	0.13	19.1	Rubotherm
ZIF-8-T	0.11	11.5	Cahn
ZIF-8-P	0.10	11.5	Cahn
La-PDA	0.09	16.8	Cahn
BAsolite Z1200	0.09	13.2	Rubotherm
UMCM-1	0.06	16.1	Rubotherm
Ni-bpe	0.05	32.4	Rubotherm
Ni-MAMS-1	0.04	17.9	Cahn

* s denotes steamed; p denotes powder; pt denotes pellet; s p denotes steamed powder; s pt denotes steamed pellet; cal denotes calcined.

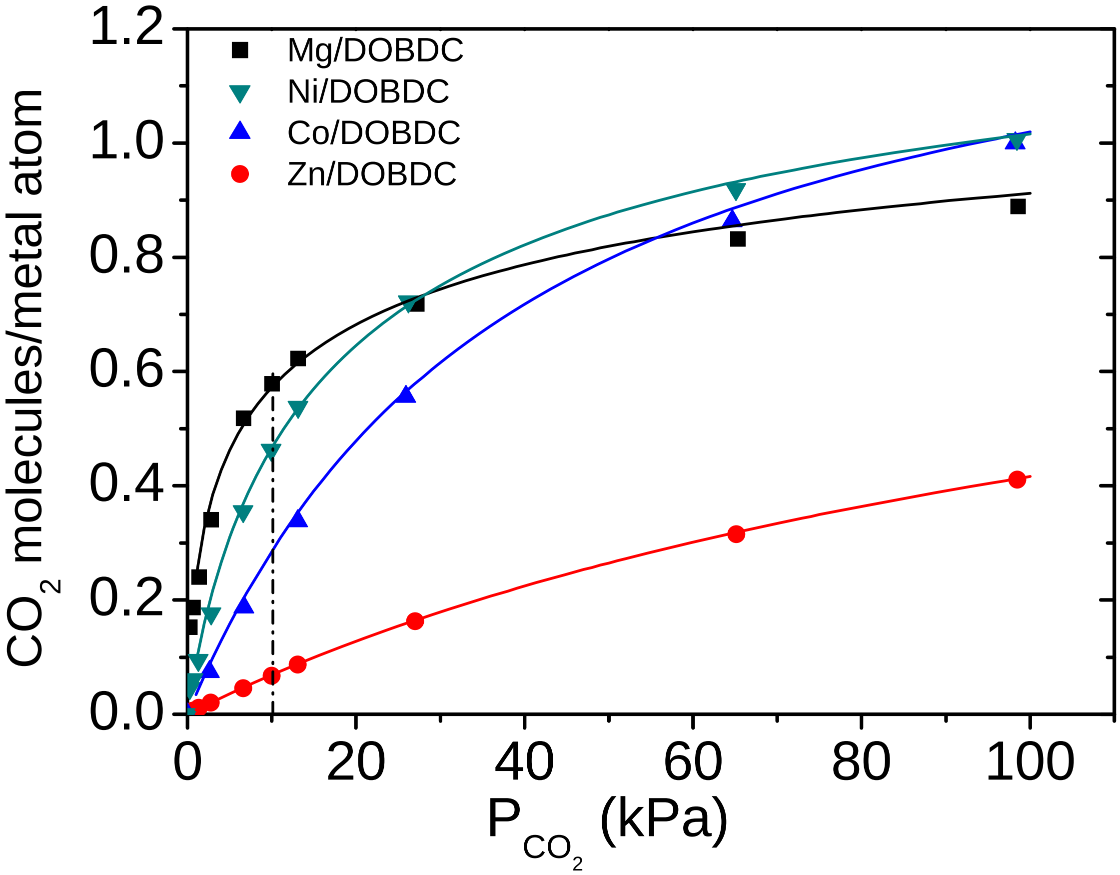

Figure 2.7: CO_2 isotherms for DOBDC-series MOFs at 100 °F based on per metal atom.

2.4 Conclusions

About 30 MOF samples were screened for CO_2 adsorption at sub-atmospheric pressures and 100 °F using a gravimetric method. We found no correlation between CO_2 capacity of a MOF sample and its surface area or pore volume. CO_2 capacities at the POI for most of the MOFs considered follow a similar trend to the average isosteric heats of adsorption with high capacity corresponding to high heat of adsorption. The DOBDC series of MOFs with UMCs in their structures are very good for CO_2 adsorption, especially in the low pressure range, because UMCs offer extra adsorption sites for CO_2 adsorption and enhance the heat of adsorption.

References

[1] Sudik, A.C.; Millward, A.R.; Ockwig, N.W.; Cote, A.P.; Kim, J.; Yaghi, O.M. Design, Synthesis, Structure, and Gas (N_2, Ar, CO_2, CH_4, and H_2) Sorption Properties of Porous Metal-Organic Tetrahedral and Heterocuboidal Polyhedra. *J. Am. Chem. Soc.* **2005**, *127*, 7110–7118.

[2] Li, H.L.; Eddaoudi, M.; O'Keeffe, M.; Yaghi, O.M. Design and Synthesis of An Exceptionally Stable and Highly Porous Metal-Organic Framework. *Nature* **1999**, *402*,276–279.

[3] Millward, A.R.; Yaghi, O.M. Metal-Organic Frameworks with Exceptionally High Capacity for Storage of Carbon Dioxide at Room Temperature. *J. Am. Chem. Soc.* **2005**, *127*, 17998–17999.

[4] Dietzel, P. D. C.; Johnsen, R. E.; Fjellvag, H.; Bordiga, S.; Groppo, E.; Chavan, S.; Blom, R. Adsorption Properties and Structure of CO_2 Adsorbed on Open Coordination Sites of Metal-Organic Framework Ni_2(dhtp) from Gas Adsorption, IR Spectroscopy and X-Ray Diffraction. *Chem. Commun.* **2008**, *41*, 5125–5127.

[5] Liang, Z. J.; Marshall, M.; Chaffee, A. L. CO_2 Adsorption-Based Separation by Metal Organic Framework (Cu-BTC) versus Zeolite (13X). *Energy & Fuels* **2009**, *23*, 2785–2789.

[6] Yang, R.T. *Gas Separation by Adsorption Process*, Chapter 3, Butterworths Publishers, Maryland, 1987.

[7] Mofarahi, M.; Khojasteh, Y.; Khaledi, H.; Farahnak, A. Design of CO_2 Absorption Plant for Recovery of CO_2 from Flue Gases of Gas Turbine. *Energy* **2008**, *33*, 1311–1319.

[8] Yazaydin, A. O.; Snurr, R. Q.; Park, T. H.; Koh, K.; Liu, J.; LeVan, M. D.; Benin, A. I.; Jakubczak, P.; Lanuza, M.; Galloway, D. B; Low, J. J.; Willis, R. R. Screening of Metal-Organic Frameworks for Carbon Dioxide Capture from Flue Gas Using a Combined Experimental and Modeling Approach. *J. Am. Chem. Soc.* **2009**, *131*, 18198–18199.

[9] Ruthven, D.M.; Farooq, S.; Knaebel, K. S. *Pressure Swing Adsorption*, VCH Publishers, Inc., New York, 1994.

[10] Taqvi, S. M.; Appel, W. S.; LeVan, M. D. Coadsorption of Organic Compounds and Water Vapor on BPL Activated Carbon. 4. Methanol, Ethanol, Propanol, Butanol, and Modeling. *Ind. Eng. Chem. Res.* **1999**, *38*, 240–250.

[11] Caskey, S. R.; Wong-Foy, A. G.; Matzger, A. J. Dramatic Tuning of Carbon Dioxide Uptake via Metal Substitution in a Coordination Polymer with Cylindrical Pores. *J. Am. Chem. Soc.* **2008**, *130*, 10870–10871.

[12] Frost, H.; Düren, T.; Snurr, R.Q. Effects of Surface Area, Free Volume, and Heat of Adsorption on Hydrogen Uptake in Metal-Organic Frameworks. *J. Phys. Chem. B* **2006**, *110*, 9565–9570.

[13] Gupta, A.; Chempath, S.; Sanborn, M. J.; Clark, L. A.; Snurr, R. Q. Object-oriented Programming Paradigms for Molecular Modeling . *Molecular Simulation* **2003**, *29*, 29–46.

[14] Rosi, N.L.; Kim, J.; Eddaoudi, M.; Chen, B.L.; O'Keeffe, M.; Yaghi, O.M. Rod Packings and Metal-Organic Frameworks Constructed from Rod-Shaped Secondary Building Units. *J. Am. Chem. Soc.* **2005**, *127*, 1504–1518.

[15] Liu, J.; Wang, Y.; Benin, A. I.; Jakubczak, P.; Willis, R. R.; LeVan, M. D. CO_2/H_2O Adsorption Equilibrium and Rates on Metal-Organic Frameworks: HKUST-1 and Ni/DOBDC. *Langmuir* **2010**, *26*, 14301–14307.

CHAPTER III

CO_2 ADSORPTION RATE STUDY FOR MOF PELLETS USING THE CONCENTRATION SWING FREQUENCY RESPONSE METHOD

3.1 Introduction

Physical adsorption at a surface is generally so fast that in a porous adsorbent the overall rate of adsorption is controlled by mass or heat transfer resistances, instead of the intrinsic adsorption kinetics.[1] Therefore, an understanding of the mass transfer resistance is important for the design of an isothermal adsorption process.

Besides equilibrium studies on CO_2 adsorption in MOFs, we have investigated rates of CO_2 adsorption in MOF materials for practical industrial applications. Some prior research work has been done on this topic. Bracia *et al.*[2] obtained an intracrystalline diffusivity for CO_2 adsorption in MOF-508b by fitting breakthrough data. Babarao *et al.*[3] calculated the self, corrected, and transport diffusivities for CO_2 adsorption in IRMOF-1 using molecular dynamics simulation. Based on their results the self-diffusivity of CO_2 in IRMOF-1 is several times higher than in silicalite (MFI). Yang *et al.*[4] also obtained similar self-diffusivities for CO_2 adsorption in several MOFs with large pores. Liu *et al.*[5] found that the self-diffusivities of CO_2 in ZIF-68 and ZIF-69 are one order of magnitude smaller than for MOFs with large pores because of steric hindrance caused by narrow pores in the structures of the ZIF materials. Zhao *et al.*[6] measured the diffusion coefficient for CO_2 adsorption in MOF-5 using a gravimetric method and assumed that intracystalline diffusion is the mass transfer mechanism. All of these studies help in understanding rates for CO_2 adsorption in MOF materials. Generally, self-diffusivities or intracrystalline diffusivities for CO_2 adsorption in MOFs are larger than in zeolites because of larger pores and open structures in MOF materials. It would be helpful to determine the controlling mass transfer mechanism directly and measure corresponding rate coefficients as compared to fitting diffusivities by pre-assuming a micropore diffusion mechanism or some other controlling resistance for CO_2 adsorption in MOFs.

The frequency response (FR) method has been widely used to investigate the kinetic behaviors of gas adsorption processes because of its capability to distinguish among different rate limiting mechanisms.[7,8] The FR method is one of the most effective methods for the study of the adsorption kinetics. This method, first used by Polinski and Naphtali to study the adsorption dynamics, allows for easy probing of different mass transfer resistances as the frequency is changed.[9]

The most common means of applying the FR method is periodically varying the system volume by a slight amount, typically 1 to 2% of the total volume, and recording the pressure changes within a closed batch system. While batch systems are in the majority, more recently invented flow systems have several advantages compared with batch system FR methods, including reduction of heat transfer effects and convenience in measuring multicomponent adsorption effects.[10] Flow-through frequency response methods have been explored to provide more practical advantages, such as easily implementing a wide range of frequencies, having the possibility of using large relative amplitudes, and having reduced heat effects.[11–13]

3.2 FR Model and Theory

Due to the introduction of a very small perturbation in the frequency response methods, most studies have assumed isothermal conditions in the mathematical models. A simple model assuming isothermal operation and uniform gas concentration in the adsorption region will be used in our study.[7] The total system can be divided into three parts: the inlet region, the adsorption region, and the outlet region as shown in Fig. 3.1. In our system, the outlet volume is very small and is considered negligible. Only the inlet and the adsorption region will be considered here. For pure gas adsorption, only a one component mass balance will be considered.

For the inlet region, the material balance for the adsorbable component (component 1) is

$$\frac{dy_{1,out,V_1}}{dt} = \frac{F}{V_1}\left(y_{1,in,V_1}(t) - y_{1,out,V_1}(t)\right) \tag{3.1}$$

where V_1 is the volume of the inlet region, $y_{1,in}$ and $y_{1,out}$ are the mole fractions for component 1 in the inlet stream and outlet stream for the inlet region, and F is a constant total flow rate entering the system. Helium is component 2 and is treated as inert.

For the adsorption region, the material balance for component 1 can be written

$$\frac{dy_{1,out,V_b}}{dt} + \frac{M_b}{V_b c_0}\frac{dn_1}{dt} = \frac{F}{V_b}(y_{1,in,V_b}(t) - y_{1,out,V_b}(t)) \tag{3.2}$$

where V_b is the void volume in the adsorption bed, and M_b is the adsorbent amount.

The gas composition which enters the adsorption region is the same as that coming out from the inlet region, giving

$$y_{1,in,V_b}(t) = y_{1,out,V_1}(t) \tag{3.3}$$

The adsorbed-phase concentration n_1 can be related to the gas phase concentration y_1 in a general way in the Laplace domain giving

$$\bar{n}_1 = G_n\,\bar{y}_1 \tag{3.4}$$

Substituting eq 3.3 and eq 3.4 into eq 3.2 and combining the obtained equation with eq 3.1 gives the transfer function for the total system[14]

$$G_T = \frac{\bar{y}_{1,out,V_b}}{\bar{y}_{1,in,V_1}} = \frac{(F/V_1)(F/V_b)}{(s + F/V_1)[s(1 + M_b/(V_b c_0)G_n) + F/V_b]} \tag{3.5}$$

The adsorbed-phase transfer function G_n depends only on the properties of the adsorbate, which are determined by the mass transfer mechanisms within the adsorbent particles. Our group has developed different models to describe different

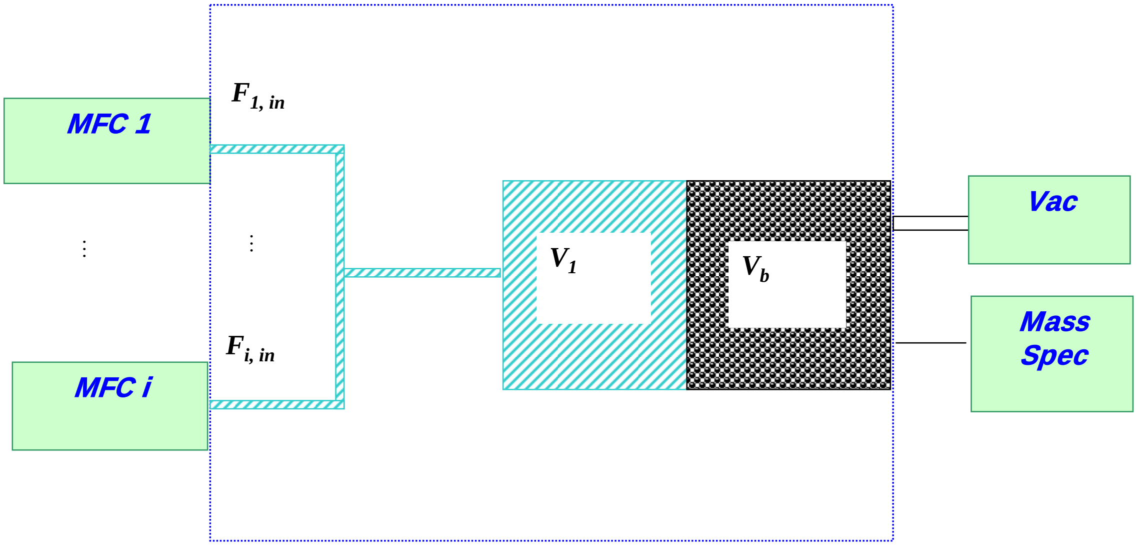

Figure 3.1: Schematic diagram of the mass balance in a FR system.

controlling mechanisms, including nanopore diffusion, a barrier resistance characterized by a linear driving force (LDF), a combined resistance model, as well as a kinetic distribution model.[7]

We consider the nanopore diffusion case here as a first example. For an isothermal condition and spherical geometry, the real and imaginary parts of G_n for the nanopore diffusion model are given by[14]

$$\begin{aligned} \mathrm{Re}[G_n(j\omega)] &= 3K\frac{1}{\nu}\frac{\sinh\nu - \sin\nu}{\cosh\nu - \cos\nu} \\ \mathrm{Im}[G_n(j\omega)] &= 6K\frac{1}{\nu^2}\left[\frac{\nu}{2}\frac{\sinh\nu + \sin\nu}{\cosh\nu - \cos\nu} - 1\right] \end{aligned} \tag{3.6}$$

where $\nu = \sqrt{2\omega R^2/D}$ with R being the radius of the controlling domain for nanopore diffusion, and K is the local slope of the isotherm.

If we substitute eq 3.6 into eq 3.5 and use $s = j\omega$, where ω is the experimental frequency, the transfer function for the total system is a complex number at each frequency. The modulus of the complex number corresponds to the amplitude ratio of the outlet and inlet gas mole fraction obtained from the experimental results. If the ratios of the experimental outlet and inlet gas mole fractions and the modulus of total transfer function agree well at every frequency, the controlling mechanism for the gas transport within the particles would be considered as nanopore diffusion. The diffusivity term D/R^2 can be determined by parameter estimation methods. If the ratios of the gas mole fraction and the modulus of transfer function do not agree well, other mass transfer controlling mechanisms can be selected to describe the gas transport.

Another familiar mass transfer mechanism for gas adsorption is macropore diffusion, which usually indicates that the main mass transfer resistance is from diffusion between intercrystal structures.[15] Macropore diffusion has an analogical adsorption rate equation to micropore diffusion for the linearized models.[15] Thus, they share the same adsorbed-phase transfer function G_n shown above. However, macropore diffusion has a different diffusivity term from micropore diffusivity, and the diffusivity term of macropore diffusion can be related with that of the micropore diffusion by

$$D_p/R_p^2 = D_s/r^2(\eta(1 + \rho_p K/\epsilon_p) \tag{3.7}$$

where D_p is the macropore diffusivity, R_p is the characteristic radius of macropore diffusion, D_s is the micropore diffusivity, r is the micropore radius, ρ_p is the particle density (kg/m^3), K is the local isotherm slope (m^3/kg), and ϵ_p is the porosity of the particle.[15] Therefore, the macropore diffusivity term can be estimated similarly as mentioned in the micropore diffusion case. A usual way to distinguish between the two diffusion resistances is to study and determine whether the mass transfer rate depends on particle size. Macropore diffusion resistance depends on particle size, whereas micropore diffusion resistance do not for formed particles.[15]

3.3 Apparatus and Procedures

Fig. 3.2 shows the diagram of the concentration swing frequency response (CSFR) system we used to study the CO_2 adsorption rates in MOFs. The CO_2 gas was fed to the system at a mean flow rate of 1 sccm with a sinusoidal pertubation of 0.5 sccm amplitude. Simultaneously, helium was fed to the system at a mean flow rate of 49 sccm with the sinusoidal pertubation of 0.5 sccm amplitude but reversed in phase. The resulting mixtures, having a constant flow rate of 50 sccm but a sinusoidally modulated CO_2 concentration, were passed through a shallow adsorption bed packed with MOF pellets and were exhausted through a vacuum pump. The flow rate was controlled by a mass flow controller (MKS 1479A). The system pressure was maintained by a pressure controller (MKS 640) downstream of the adsorption bed. The inlet and outlet concentrations of CO_2 were analyzed by a mass spectrometer (HP 5971A), and amplitude ratios of the outlet concentration to the inlet concentration were used to extract mass transfer rates with developed mathematical models.[10]

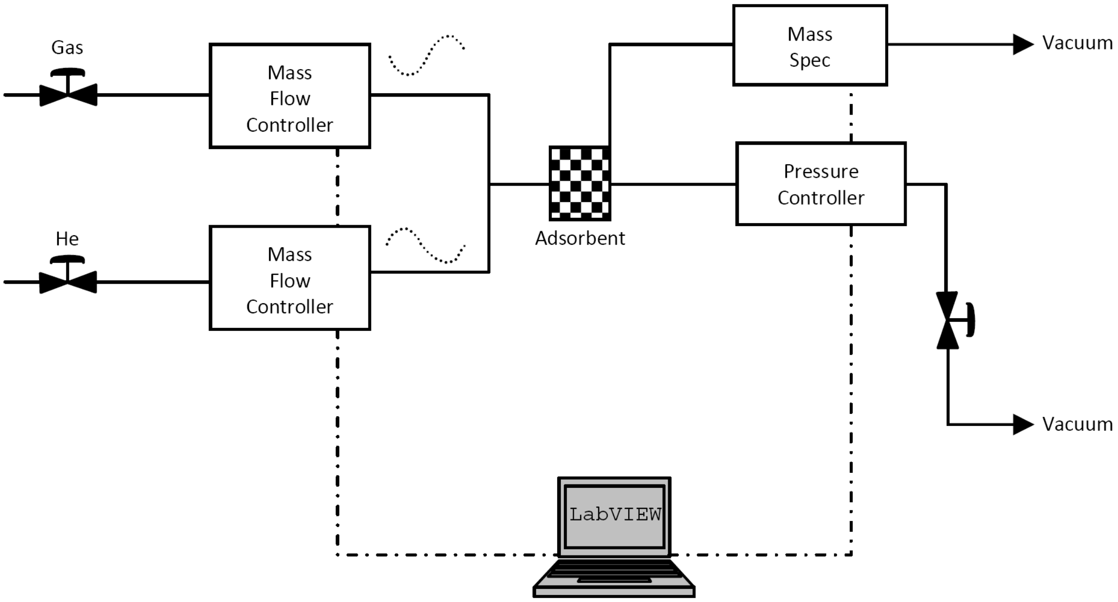

Figure 3.2: CSFR system for CO_2 adsorption rate study.

The use of a small adsorption bed makes this method suitable for the study of new materials, which may exist in small quantities. Also, the small volume helps to measure relatively fast kinetics because of less void space involved. Utilizing a small amount of adsorbent has been shown to eliminate axial dispersion effects, which results in a simpler mathematical model of the system and reduces thermal effects present in the system.[8,14]

Calibration and blank control experiments were conducted before all measurements. Experiments were conducted under preset CO_2 concentrations with an empty adsorption bed to calibrate the mass spectrometer. Blank control experiments were conducted under the same conditions as real measurements with the adsorption bed loaded with non-adsorbed glass beads instead of MOF samples.

3.4 Results and Discussion

In our CO_2 adsorption rate study, we examined mass transfer rates for HKUST-1 and Ni/DOBDC pellets both with three different thicknesses. The results for HKUST-1 pellets and Ni/DOBDC pellets are shown in Fig. 3.3 and Fig. 3.4, respectively. The pellets are labeled as M-1, M-2 and M-3 (M = Cu for HKUST-1 and M = Ni for Ni/DOBDC) in the order of increasing thickness in these figures. Data points are from experiments and the values of the diffusivity parameter η were obtained by fitting the experimental data. Predicted curves are also included to verify the fitting results. The relative positions between experimental data points and the predicted curves change from one pellet to another, which indicates a dependency of the estimated diffusivity parameters on the pellet thickness and also shows good agreement between the predicted curves and fitting results.

The estimated diffusivity parameters for all of the HKUST-1 and Ni/DOBDC pellets are summarized in Table. 3.1. The diffusivity parameters shown in Fig. 3.3 and Fig. 3.4 are several orders of magnitude larger than we have found for some other ad-

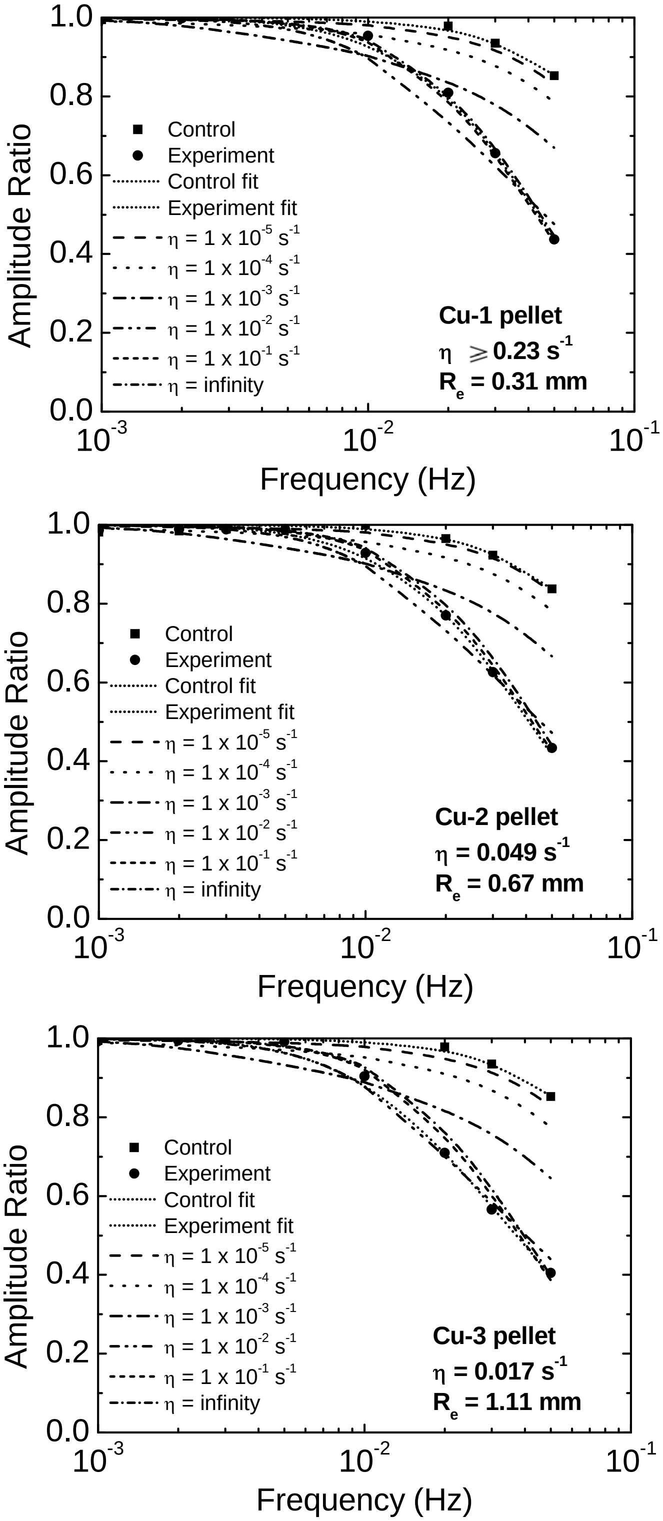

Figure 3.3: Frequency response results for HKUST-1 pellets with different thicknesses. The pellets are labeled as Cu-1, Cu-2, and Cu-3 in the order of increasing thickness.

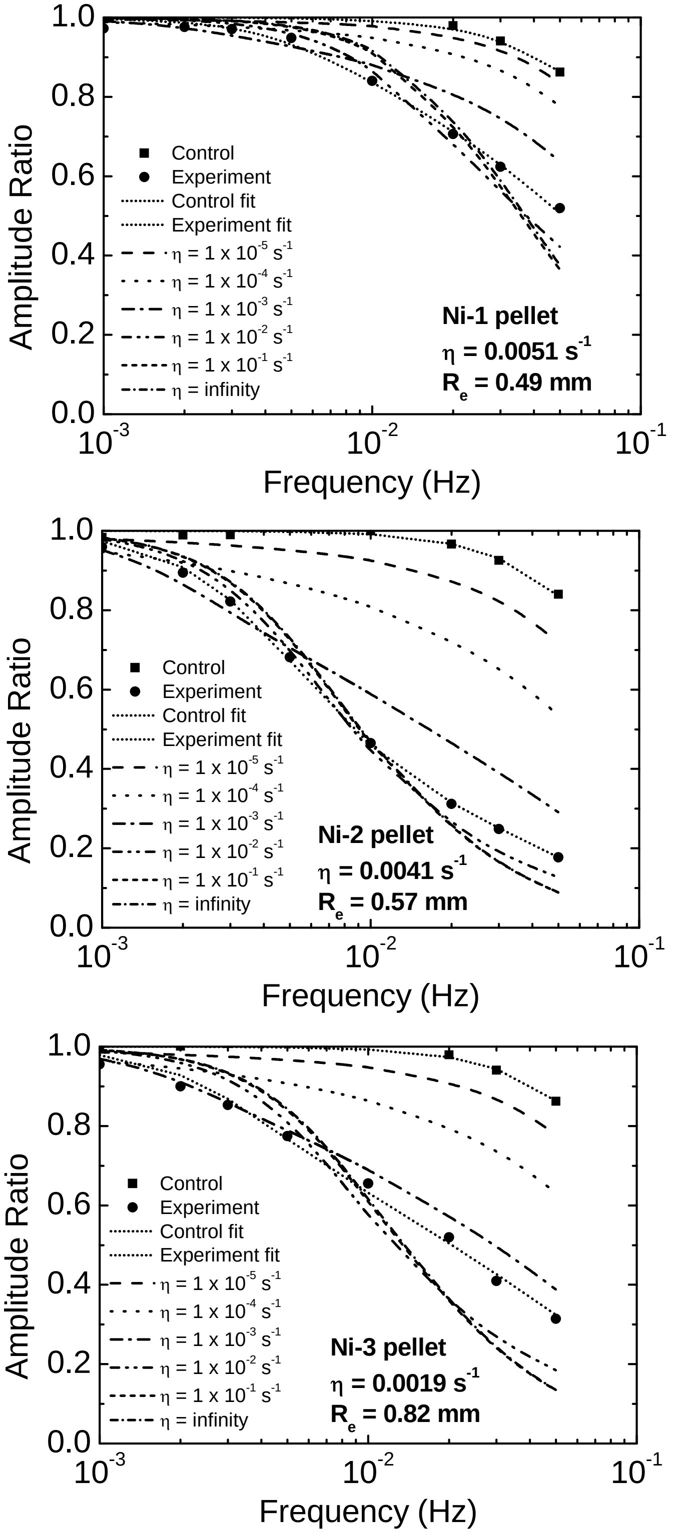

Figure 3.4: Frequency response results for Ni/DOBDC pellets with different thicknesses. The pellets are labeled as Ni-1, Ni-2, and Ni-3 in the order of increasing thickness.

Table 3.1: Summary of the diffusivity parameters for MOF pellets with different thicknesses.

Sample	Equivalent radius (mm)	η-exp (s^{-1})	η-calc (s^{-1})
Cu-1 pellet	0.31	≥ 0.23	0.44
Cu-2 pellet	0.67	0.049	0.096
Cu-3 pellet	1.11	0.017	0.035
Ni-1 pellet	0.49	0.0051	0.0043
Ni-2 pellet	0.57	0.0041	0.0031
Ni-3 pellet	0.82	0.0019	0.0015

sorbents,[14,16] which indicates very fast rates for CO_2 transport in both HKUST-1 and Ni/DOBDC pellets. The dependency of the measured rates on the equivalent pellet radii suggests that the mass transfer mechanism for CO_2 adsorption in HKUST-1 and Ni/DOBDC pellets is macropore diffusion control because external film resistance is found to be much smaller than the pore diffusion resistance. The macropore diffusivity term D_p/R_e^2 and the diffusivity parameter η that we obtain in our study are related by[15]

$$D_p/R_e^2 = \eta(1 + \rho_p K/\epsilon_p) \tag{3.8}$$

where D_p is the macropore diffusivity, ρ_p is the pellet density (kg/m^3), K is the local isotherm slope (m^3/kg), ϵ_p is the macropore porosity, and R_e is the equivalent radius given by[17]

$$R_e = 3 \times \frac{\text{volume of pellet}}{\text{surface area of pellet}} \tag{3.9}$$

The identification of macropore diffusion as the controlling resistance is consistent with the open structures of these two MOFs. Furthermore, if we replace the LHS of equation 3.8 with the bulk diffusivity term, $D_{bulk}/R_e^2\tau$, where D_{bulk} is the CO_2 diffusivity in He and τ is the tortuosity, we obtain diffusivity parameters that have the same order of magnitude as the diffusivity parameters estimated from our experiments. This indicates that CO_2 molecules diffuse through the MOF pellets much like binary diffusion in the bulk gas phase, and the main resistance is diffusion through the intercrystal macropores. This is in contrast to a rate limitation dominated by diffusion in intracrystal micropores, which has previously been considered.[4–6]

3.5 Conclusions

A CSFR system was used to study the CO_2 adsorption rate in HKUST-1 and Ni/DOBDC pellets. The small adsorption bed in the system needs only a small quantity of sample and can help minimize any heat effects. Generally, CO_2 mass transfer rates for MOF pellets of HKUST-1 and Ni/DOBDC are fast. The CSFR method can distinguish among different mass transfer resistances. Macropore diffusion was determined to be the rate controlling mechanism for CO_2 adsorption in both HKUST-1 and Ni/DOBDC pellets after comparing and analyzing results for pellets with different thicknesses.

References

[1] Ruthven, D. M. *Principles of Adsorption and Adsorption Process*; John Wiley & Sons, Inc: New York, 1984.

[2] Bracia, P. S.; Bastin L.; Hurtado, E. J.; Silva, J. A. C.; Rodrigues, A. E.; Chen, B. Single and Multicomponent Sorption of CO_2, CH_4 and N_2 in a Microporous Metal-Organic Framework. *Sep. Sci. Technol.* **2008**, 43, 3494–3521.

[3] Babarao, R.; Jiang, J. W. Diffusion and Separation of CO_2 and CH_4 in Silicalite, C_{168} Schwarzite, and IRMOF-1: A Comparative Study from Molecular Dynamics Simulation. *Langmuir* **2008**, 24, 5474–5484.

[4] Yang, Q. Y.; Zhong, C. L.; Chen, J. F. Computational Study of CO_2 Storage in Metal-Organic Frameworks. *J. Phys. Chem. C* **2008**, 112, 1562–1569.

[5] Liu D. H.; Zheng, C. C.; Yang, Q. H.; Zhong, C. L. Understanding the Adsorption and Diffusion of Carbon Dioxide in Zeolitic Imidazolate Frameworks: A Molecular Simulation Study. *J. Phys. Chem. C* **2009**, 113, 5004–5009.

[6] Zhao, Z. X.; Li, Z.; Lin, Y. S. Adsorption and Diffusion of Carbon Dioxide on Metal-Organic Framework (MOF-5). *Ind. Eng. Chem. Res.* **2009**, 48, 10015–10020.

[7] Wang, Y.; Sward, B. K.; LeVan, M. D. New Frequency Response Method for Measuring Adsorption Rates via Pressure Modulation: Application to Oxygen and Nitrogen in a Carbon Molecular Sieve. *Ind. Eng. Chem. Res.* **2003**, 42, 4213–4222.

[8] Glover, T. G.; Wang, Y.; LeVan, M. D. Diffusion of Condensable Vapors in Single Adsorbent Particles Measured via Concentration-Swing Frequency Response. *Langmuir* **2008**, 24, 13406–13413.

[9] Polinski, L.M., Naphtali, L.M. A Novel Technique for Characterization of Adsorption Rates on Heterogeneous Surfaces. *J. Phys. Chem.* **1963**, 67, 369–375.

[10] Sward, B.K.; LeVan, M. D. Frequency Response Method for Measuring Mass Transfer Rates in Adsorbents via Pressure Perturbation. *Adsorption* **2003**, 9, 37–54.

[11] Park, I. S.; Petkovska, M.; Do, D. D. Frequency Response of an Adsorber with Modulation of the Inlet Molar Flow-rate I. A Semi-Batch Adsorber. *Chem. Eng. Sci.* **1998**, *53*, 819–832.

[12] Park, I. S.; Petkovska, M.; Do, D. D. Frequency Response of an Adsorber with Modulation of the Inlet Molar Flow-rate: II. A Continuous Flow Adsorber. *Chem. Eng. Sci.* **1998**, *53*, 833–843.

[13] Do, D. D.; Do, H. D.; Prasetyo, I. Constant Molar Flow Semi-batch Adsorber as a Tool to Study Adsorption Kinetics of Pure Gases and Vapors. *Chem. Eng. Sci.* **2000**, *55*, 1717–1727.

[14] Wang, Y.; LeVan, M. D. Nanopore Diffusion Rates for Adsorption Determined by Pressure-Swing and Concentration-Swing Frequency Response and Comparison with Darken's Equation. *Ind. Eng. Chem. Res.* **2008**, 47, 3121–3128.

[15] Green, D. W.; Perry, R. H. *Perry's Chemical Engineers' Handbook (8th Edition)*; McGraw-Hill: New York, NY, 2008.

[16] Wang, Y.; LeVan, M. D. Mixture Diffusion in Nanoporous Adsorbents: Development of Fickian Flux Relationship and Concentration-Swing Frequency Response Method. *Ind. Eng. Chem. Res.* **2007**, 46, 2141–2154.

[17] Twigg, M. V. *Catalyst Handbook*; Wolfe Publishing Ltd: London, 1989.

CHAPTER IV

H_2O ADSORPTION AND SIMULATED FLUE GAS CONDITIONING EFFECTS ON CO_2 ADSORPTION IN MOFS

4.1 Introduction

A difficulty in using traditional zeolites (5A, NaX, etc.) to capture CO_2 from flue gas is the adsorption of H_2O, which is contained in the flue gases and is strongly adsorbed on the zeolites.[1] In addition, the presence of a trace amount of water can significantly affect the CO_2 capacities of the zeolites.[2] Therefore, it is important to study the H_2O effect during the investigation of CO_2 adsorption in MOF materials. In a process design using a MOF or another adsorbent, it may be advantageous to utilize a guard bed to adsorb water and thereby minimize H_2O effects on the adsorbent targeted for CO_2 capture.

Most MOF materials are considered to have hydrophilic surfaces, which generally have strong interactions with H_2O molecules.[3,4] However, the H_2O adsorption process in some MOF materials, such as HKUST-1, is reversible and the adsorbed H_2O can be thoroughly removed under moderate temperatures.[5] Experimental and simulated room temperature H_2O isotherm data have been reported for HKUST-1.[6–8] Results have revealed some characteristics for H_2O adsorption in HKUST-1 but have not provided information on the effect of H_2O on adsorption of CO_2 or other gases. Yazaydin *et al.*[9] has recently reported interesting simulation and experimental results on enhancing the CO_2 capacities for HKUST-1 by pre-adsorbing 4 wt% H_2O. More research is needed to address higher loadings of water, such as those that would be encountered in capturing CO_2 from wet flue gas. Especially, extensive experimental studies are still needed to help better understand the H_2O effect on CO_2 capture from flue gas by using MOF materials as adsorbents.

Besides CO_2 and H_2O, typical flue gases also contains trace amounts of acid gases such as NO_x and SO_x.[10] Therefore, it is also necessary to investigate the impact of exposure to acid gas and moisture on CO_2 adsorption in MOF samples.

We selected two of the DOBDC series MOFs, Ni/DOBDC, and Mg/DOBDC, as well as HKUST-1 as our targets for the study of H_2O and simulated flue gas conditioning effects on CO_2 adsorption in MOFs. The DOBDC series of MOFs with UMCs are found to be the best MOF candidates for CO_2 adsorption in the low pressure range. Beyond the DOBDC series of MOFs, HKUST-1 (also known as CuBTC and MOF-199) has the highest CO_2 capacity at the POI among all other MOFs that were considered, and it is also among the most studied MOFs.

4.2 Synthesis

Most MOF materials are synthesized through solvothermal reactions. The MOF samples in our research were synthesized by our collaborators from UOP and University of Michigan. Their synthesis procedures are modified from the literature.[11–13]

To make HKUST-1, copper(II) nitrate hemipentahydrate (10.0 g, 43.0 mmol, Aldrich) and benzene-1,3,5-tricarboxylic acid (BTC, 5.0 g, 23.8 mmol, Aldrich) were stirred for 1 h in 250 mL of solvent consisting of equal parts N,N-dimethylformamide (DMF, Fisher), ethanol (Fisher) and deionized water in a 1-L wide mouth glass vessel. The vessel was tightly capped and heated at 85 °C for 24 h to yield small octahedral crystals as shown in Fig. 4.1 (a). After decanting the hot mother liquid and rinsing twice with DMF, the product was washed with dichloromethane (Fisher) and DMF. Then the sample was immersed in dichloromethane for 6 d, during which the dichloromethane solvent was decanted and freshly replenished twice each day. Next, the sample was dried in a hot (100 °C) nitrogen flow. Finally, the purple porous HKUST-1 sample was obtained after the residual solvent was removed at 170 °C under vacuum.

To synthesize Ni/DOBDC, nickel(II) acetate (18.7 g, 94.0 mmol, Aldrich) and 2,5-dihydroxyterephthalic acid (DOBDC, 37.3 g, 150 mmol, Aldrich) were placed in 1 L of mixed solvent consisting of equal parts tetrahydrofuran (THF) and deionized water. The mixture was then put into a 2 L static Parr reactor and heated at 110 °C for 3 d. The as-synthesized sample, shown in Fig. 4.1 (b), was filtered and washed with water. Then the sample was dried in air, and the solvent remaining inside the sample was exchanged with ethanol 6 times over 8 d. Finally, the sample was activated at 150 °C under vacuum with nitrogen flow.

Mg/DOBDC was synthesized as follows. $Mg(NO_3)_2 \bullet 6H_2O$ (0.475 g, 1.85 mmol, 3.31 equiv, Fisher) and DOBDC (0.111 g, 0.559 mmol, 1 equiv, Aldrich) were added to a 15:1:1 (v/v/v) mixture of DMF-ethanol-water (50 mL). The suspension was mixed and ultrasonicated until homogeneous. The reaction solution was then dispensed to five 20-mL scintillation vials. The reaction vials were capped tightly with Teflon-lined caps and placed in an oven at 125 °C. After 20 h, the samples were removed from the oven and allowed to cool to room temperature. The mother liquor was decanted from the yellow microcrystalline material and replaced with methanol (10 mL per vial). The yellow microcrystalline material was combined into one vial. The methanol was decanted and replenished four times over two days. The solvent was removed under vacuum at 250 °C over 5 hours, yielding the dark yellow microcrystalline, porous material. The activated material was stored under vacuum or under an inert atmosphere.

4.3 Adsorption Equilibrium and Conditioning Apparatus

Fig. 4.2 shows a schematic diagram of the volumetric system used in our experiments to measure the CO_2 and H_2O adsorption equilibrium. Pellet MOF samples were pressed from pure powder samples without any binder. Note that pelletizing

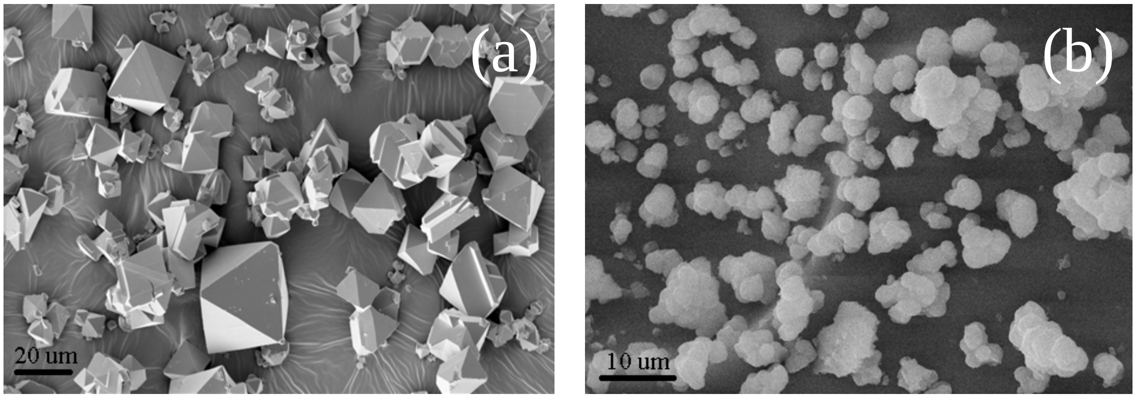

Figure 4.1: Scanning electron microscope (SEM) images for the MOF samples. (a) HKUST-1; (b) Ni/DOBDC.

without binder can cause about 5 % decrease in the CO_2 capacity for both MOF samples based on our experience. Before measurements, HKUST-1 samples were regenerated at 170 °C for 8 h under high vacuum (1×10^{-5} Pa) to obtain the fresh sample weight and regenerated again in-situ at 170 °C for 12 h under vacuum with helium flow. Similarly, Ni/DOBDC samples were regenerated at 150 °C for 8 h under high vacuum (1×10^{-5} Pa) to obtain the fresh sample weight and regenerated again in-situ at 150 °C for 12 h under vacuum with helium flow. After regeneration, gases and water vapor were introduced into the system by flow and liquid injection, respectively. These were circulated in the closed loop by the circulation pump at a rate of about 1.0 L/min. The whole apparatus was contained inside an environmental chamber (Thermotron SE-300) to keep temperature constant. Equilibrium was determined by using a gas chromatograph (GC, HP-6890) with a thermal conductivity detector (TCD). In the CO_2/H_2O binary equilibrium experiments, water was first injected into the system. After reaching equilibrium, the water loadings were constant (varied ±1.2 % of their values) through the CO_2 isotherm measurement processes as shown in Fig. 4.3 because of the strong interactions between the MOF structures and H_2O molecules. The results in Fig. 4.3 justify the procedure that we used to measure the CO_2/H_2O coadsorption by assuming that H_2O molecules are strongly adsorbed and essentially not affected by CO_2 adsorption.

Fig. 4.4 shows a schematic diagram of the apparatus that used in our experiments to study the simulated flue gas conditioning effect. The simulated flue gas used in our experiment is composed of 16% CO_2, 100 ppm SO_2, 10 ppm NO, balanced with N_2. Saturated water vapor at 17 °C was generated using a water sparger and added to the flow of simulated flue gas. Fixed flow rates of water vapor and simulated flue gas flow through the adsorption bed loaded with a MOF sample. CO_2 isotherms were measured for the same sample before and after the simulated flue gas conditioning to reveal the effects of humidity and acid gases on CO_2 adsorption performance.

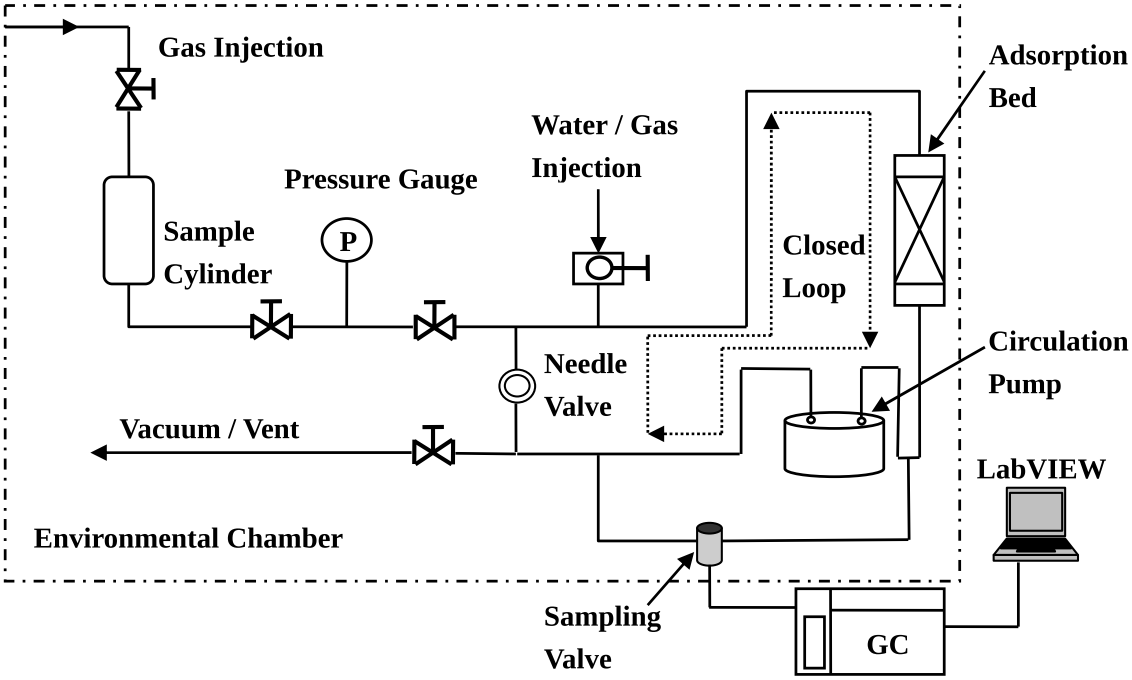

Figure 4.2: Volumetric system for CO_2/H_2O adsorption equilibrium measurement.

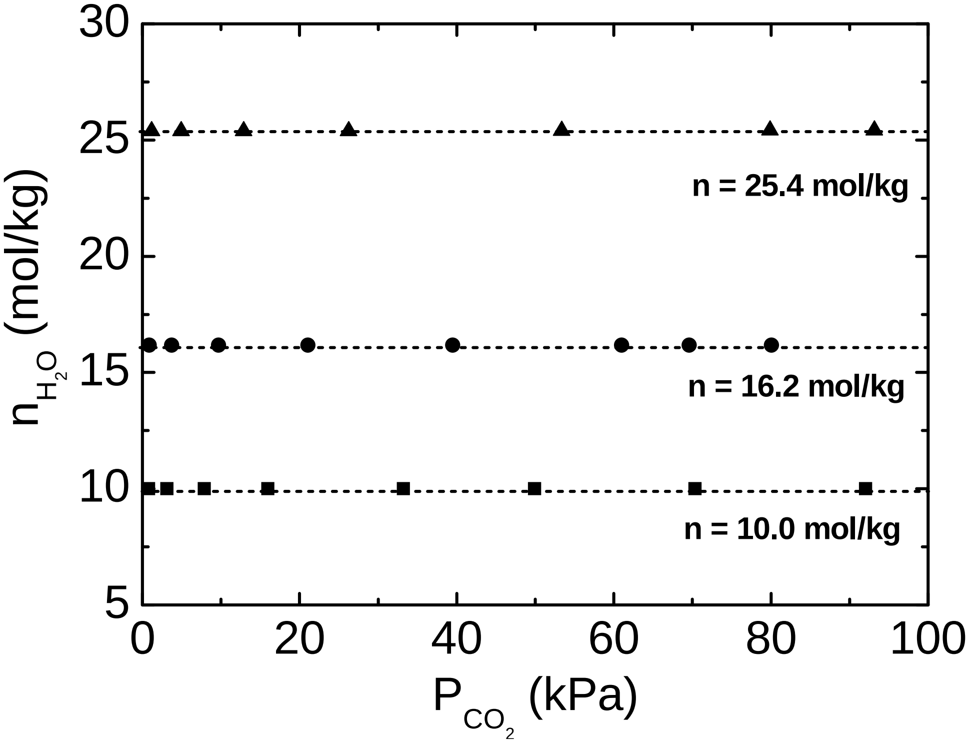

Figure 4.3: H_2O loadings during the CO_2 adsorption equilibrium measurement for HKUST-1 pellet. The three dashed lines are horizontal.

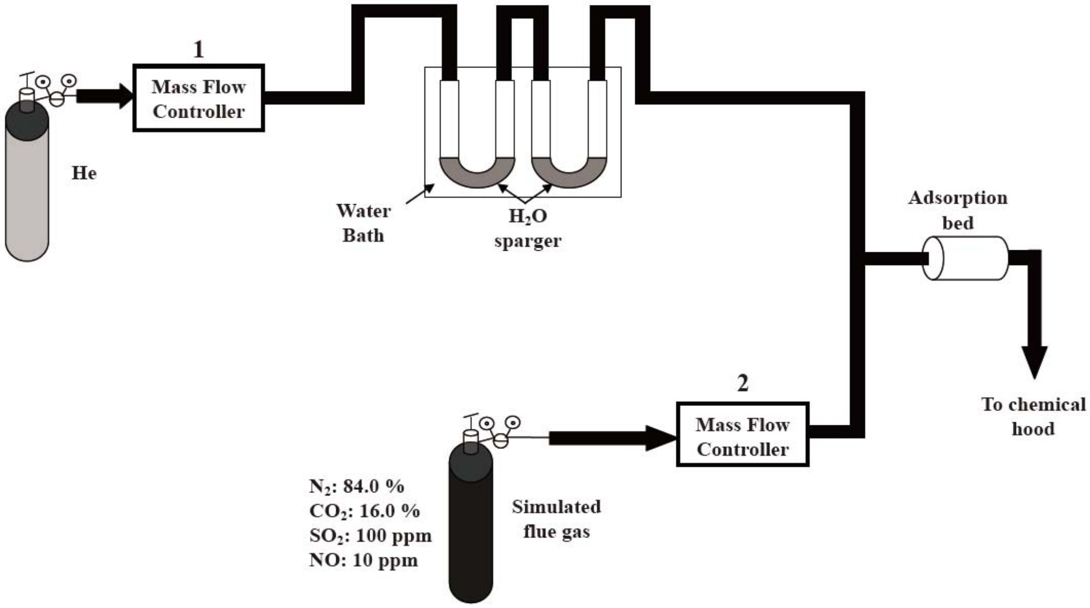

Figure 4.4: Simulated flue gas conditioning apparatus.

4.4 Pure CO_2 and H_2O Isotherms

Pure component isotherms form the basis for understanding mixture adsorption. Fig. 4.5 shows the pure CO_2 isotherms at 25 °C for both HKUST-1, Ni/DOBDC, and Mg/DOBDC pellets. We also include the results for 5A and NaX zeolite pellets (W. R. Grace) for comparison. As mentioned above, the partial pressures of CO_2 in flue gases are generally about 0.1 atm.[10,14] Therefore, we chose 0.1 atm and 25 °C for adsorption testing. From Fig. 4.5, it is clear that the CO_2 capacities for HKUST-1, Ni/DOBDC, and Mg/DOBDC pellets at 0.1 atm and 25 °C are 0.55, 3.28, and 5.65 mol/kg, respectively. The CO_2 capacity at 80 kPa for HKUST-1 is 2.68 mol/kg, which is close to the 2.81 mol/kg reported in the literature at the same pressure.[15,16] The CO_2 capacity at 100 kPa for Mg/DOBDC is 7.62 mol/kg, which is also close to the 7.81 mol/kg reported in the literature.[13] However, the CO_2 capacity we measured for Ni/DOBDC at about 1 bar is 6.68 mol/kg. This is higher than the previously reported value of 5.77 mol/kg.[13] Given 48 metal atoms per unit cell for HKUST-1 and 18 for Ni/DOBDC and Mg/DOBDC, these uptake values correspond to 0.11 CO_2 molecules/metal atom (5.3 CO_2 molecules/unit cell), 0.63 CO_2 molecules/metal atom (11.3 CO_2 molecules/unit cell), and 0.69 CO_2 molecules/metal atom (12.4 CO_2 molecules/unit cell) for HKUST-1, Ni/DOBDC, and Mg/DOBDC, respectively. This indicates that the adsorption sites in Ni/DOBDC and Mg/DOBDC are more attractive to CO_2 than those in HKUST-1.

It is interesting to note that Ni/DOBDC and Mg/DOBDC has even higher CO_2 capacities than 5A and NaX zeolites at 0.1 atm. The high gas capacities at low pressures has been ascribed to the UMCs in the crystal structures of some MOFs.[18] The Cu atoms in HKUST-1, Ni atoms in Ni/DOBDC, and Mg atoms in Mg/DOBDC are unsaturated after complete dehydration. These UMCs can coordinate with CO_2 molecules and form strong adsorption interactions, which lead to the high CO_2 capacities for the MOF samples.[19,20] However, the coordinate strength for the UMCs

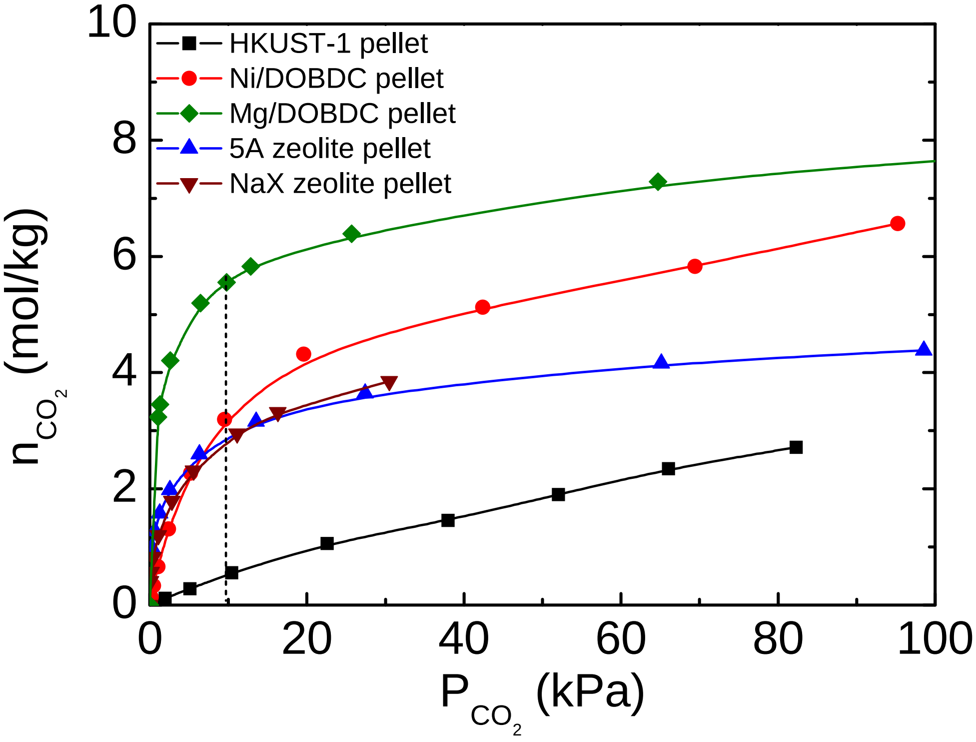

Figure 4.5: CO_2 isotherms at 25 °C for MOF and zeolite pellets. Curves are multi-temperature Toth equation fits. Zeolite results are taken from reference [17].

toward CO_2 molecules varies from one MOF type to another. A good example is the different CO_2 capacities per metal atom for HKUST-1 and Ni/DOBDC. The difference can be attributed to the stronger ionic character of the metal-oxide bond in the Ni/DOBDC as suggested in the literature.[13,21]

Pure H_2O isotherms at 25 °C for both the HKUST-1 and Ni/DOBDC pellets are shown in Fig. 4.6. The H_2O isotherm measurement was repeated several times, and we report the average results with standard deviations for the reproduced measurements shown as error bars. For HKUST-1, some prior results are also included for comparison. Because of the differences in samples, our results and the two results from the literature do not match with each other very well. It has been reported that the same MOF synthesized using different procedures can have quite different adsorption characteristics.[22] However, the high H_2O capacities and steep slopes at low loadings shown in all three isotherms indicate strong H_2O affinity for HKUST-1. Steps before reaching the saturation plateaus are also apparent in all of the isotherms. The saturated H_2O capacity for HKUST-1 pellet is about 40 mol/kg. The 25 °C H_2O isotherm for Ni/DOBDC is shown in Fig. 4.6b. We believe this to be the first experimental water isotherm reported for Ni/DOBDC. The H_2O isotherm for Ni/DOBDC pellets is steeper than that for the HKUST-1 pellet, especially in the very low pressure region, which indicates stronger interactions between H_2O molecules and the Ni/DOBDC crystal structure. According to the literature,[15] there is only one set of cylindrical pores, with a size of 11 Å, in the Ni/DOBDC framework while two sets of pores with sizes of 5 Å and 15 Å exist in the HKUST-1 framework. In addition, the adsorption sites in the Ni/DOBDC framework are more attractive to H_2O molecules. The H_2O molecules can occupy adsorption sites in Ni/DOBDC with uniformly fast rates, which leads to a shorter time to reach 80 % of the saturation H_2O capacity compared to HKUST-1 in which the two sets of pores with different sizes and less attractive adsorption sites to H_2O molecules exist.

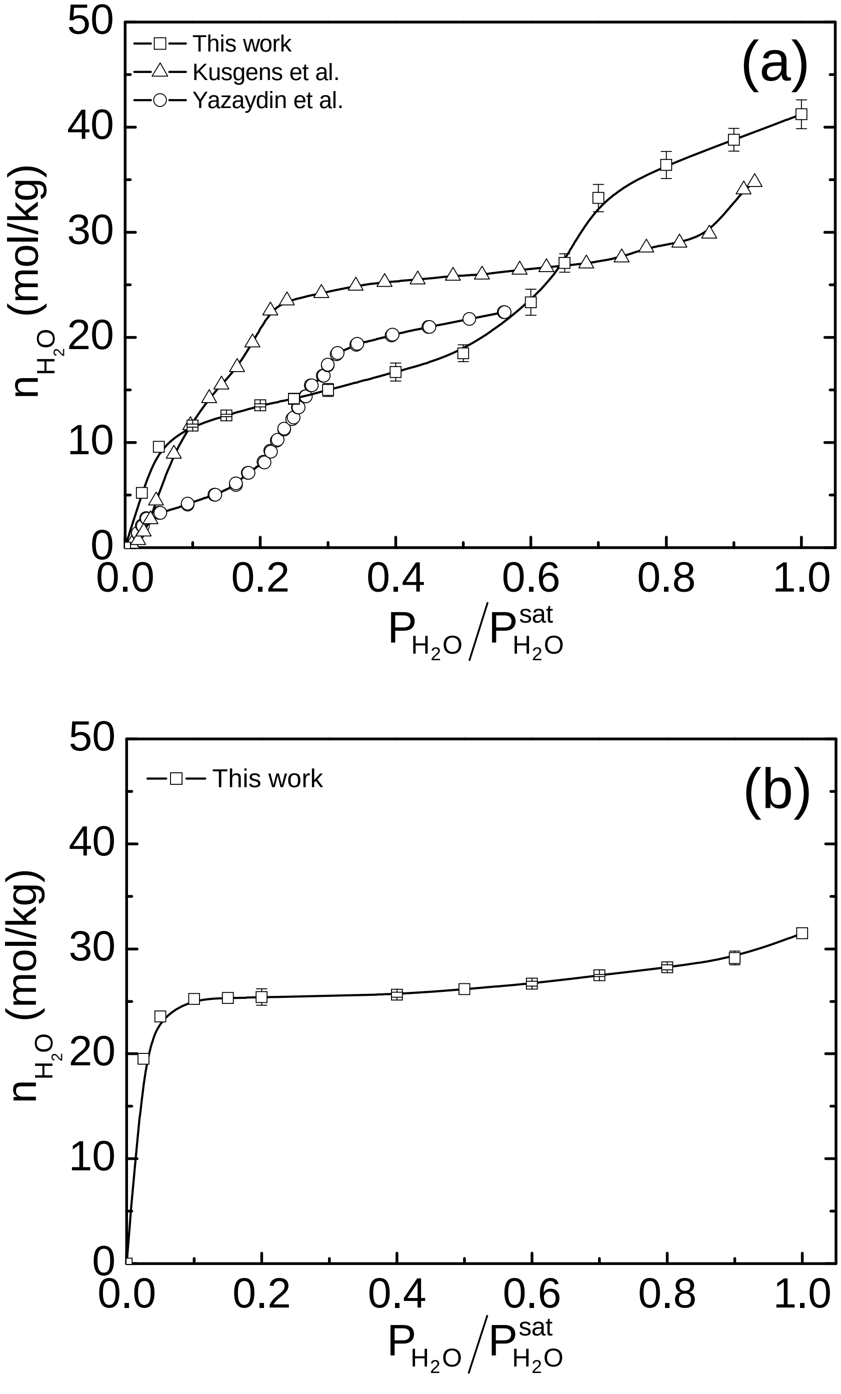

Figure 4.6: H_2O isotherms at 25 °C for MOF pellets. (a) HKUST-1 pellet; Kusgens et al.,[8] Yazaydin et al.[9] (b) Ni/DOBDC pellet. Lines are guides for the eyes.

The saturated H_2O capacity for Ni/DOBDC pellets is about 32 mol/kg. The saturated water capacity for Ni/DOBDC is lower than that of HKUST-1 while the CO_2 capacity for Ni/DOBDC shown in Fig. 4.5 is higher than for HKUST-1. For CO_2 adsorption, our isotherms for both MOFs only show the relative pressure range from 0 to 0.016. In other words, the results in Fig. 4.5 display the CO_2 adsorption behavior under relatively low concentration at which stronger adsorption sites (i.e., UMCs) lead to higher CO_2 capacities. The interaction between UMCs and CO_2 molecules in Ni/DOBDC is stronger than that in HKUST-1 as we know from previous results. In contrast, Fig. 4.6 shows the H_2O adsorption behavior for the two MOFs up to high relatively pressure at which larger surface area and pore volume usually lead to higher overall adsorption capacity. The HKUST-1 sample has a higher surface area and larger pore volume than the Ni/DOBDC sample. Consequently, it can adsorb more H_2O than Ni/DOBDC when the water vapor concentration is high. Fig. 4.7 shows CO_2 isotherms for HKUST-1 and Ni/DOBDC at higher pressure. It is clear that the CO_2 loading for HKUST-1 exceeds that of Ni/ DOBDC at pressures above 7 bar, which supports our explanation.

4.5 H_2O effect on CO_2 adsorption

As mentioned before, it is important to understand H_2O effects on CO_2 adsorption in adsorbent samples before making any conclusions about their applications in process designs to separate CO_2 from wet flue gas. Fig. 4.8, Fig. 4.9, and Fig. 4.10 show CO_2 isotherms at 25 °C for HKUST-1, Ni/DOBDC, and Ni/DOBDC pellets with different H_2O loadings. It is interesting to note from Fig. 4.8 that a small amount of adsorbed water did not affect the CO_2 capacity and may actually help to increase slightly CO_2 adsorption in HKUST-1. This has recently been ascribed to the addition of coulombic interactions between CO_2 molecules and H_2O molecules after the introduction of H_2O molecules into the system.[9] The trend of our CO_2 isotherms

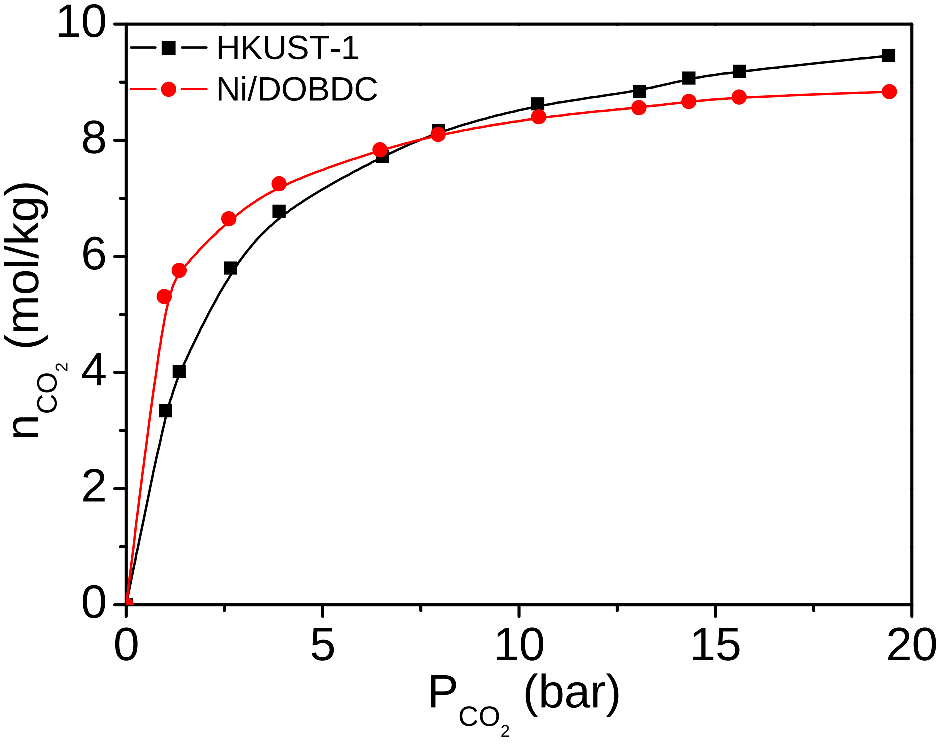

Figure 4.7: CO_2 isotherms at 25 °C and high pressure for HKUST-1 and Ni/DOBDC samples.

for HKUST-1 with low water loadings agrees quantitatively with this prediction. The CO_2 capacity for HKUST-1 decreases when the H_2O loading increases from 3.4 mol/kg to 16.2 mol/kg. HKUST-1 has lost almost all of its CO_2 capacity when the H_2O loading is about 25.4 mol/kg, which is approaching the H_2O saturation capacity (RH $\approx$ 67 %, where RH is the percent relative humidity, i.e. $P_{H_2O}/P_{H_2O}^{sat} \times 100\%$).

In Fig. 4.9, CO_2 capacities for Ni/DOBDC decrease when H_2O molecules are present. No enhancement for CO_2 adsorption by H_2O was found for this MOF sample. The Ni/DOBDC sample retained a substantial CO_2 capacity at the POI, about 2.0 mol/kg, even with a 3.4 mol/kg H_2O loading at room temperature. Similar to HKUST-1, the Ni/DOBDC sample could adsorb only small amounts of CO_2 for a high H_2O loading, which here is 28.7 mol/kg (RH $\approx$ 89 %).

In Fig. 4.10, CO_2 capacities for Mg/DOBDC decrease when the H_2O loading increases. The Mg/DOBDC pellet can adsorb 2.13 mol/kg CO_2 at 0.1 atm, even with a 3.4 mol/kg H_2O loading at room temperature. Similarly, the Mg/DOBDC sample could adsorb only small amounts of CO_2 with high H_2O loadings.

We also compared the H_2O effects on CO_2 adsorption for the three MOF pellets with those for 5A and NaX zeolite pellets. The results are shown in Fig. 4.11. It is obvious that H_2O does not inhibit CO_2 adsorption for HKUST-1 and Ni/DOBDC as much as it does for 5A and NaX zeolites, as indicated by the less steep slopes for HKUST-1 and Ni/DOBDC in the comparison plots.[23] In other words, MOF samples can adsorb relatively more CO_2 than zeolites before they are saturated with H_2O. Moreover, H_2O molecules are easier to remove from MOF samples than from zeolites by regeneration as evidenced by lower isotherm slopes for MOFs at low loadings. The temperature we used in our research to regenerate the MOF samples in-situ is no higher than 200 °C, while 350 °C or higher is often needed for removing water from zeolites. Further, framework alumina in zeolites can be extracted and react with CO_2 in water-saturated streams to form difficult to decompose carbonate species. Besides

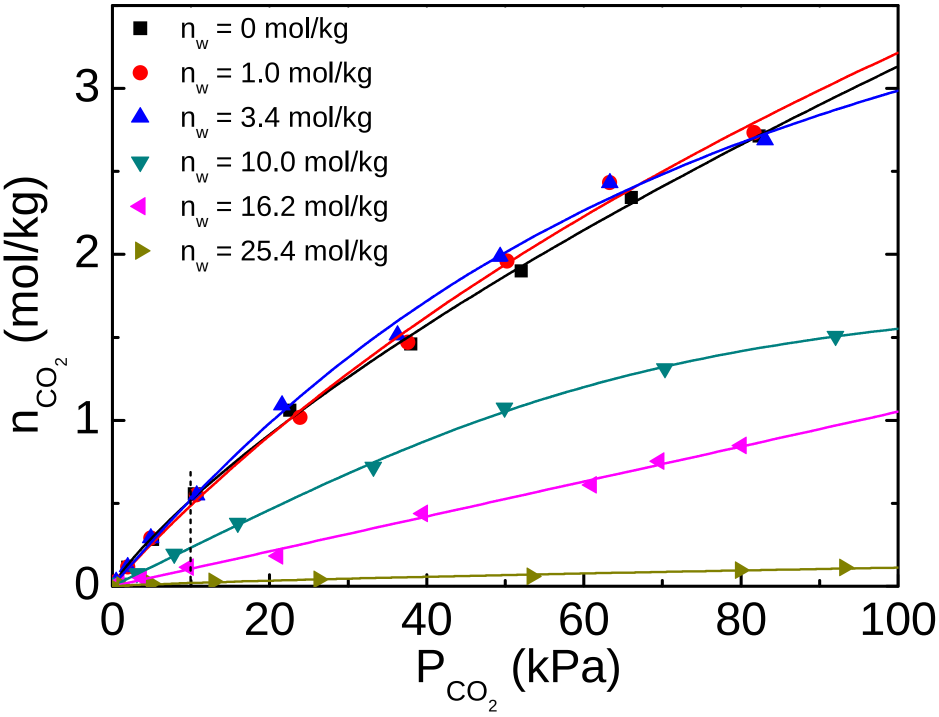

Figure 4.8: CO_2 isotherms at 25 °C for HKUST-1 pellet with different H_2O loadings. Curves are multi-temperature Toth equation fits.

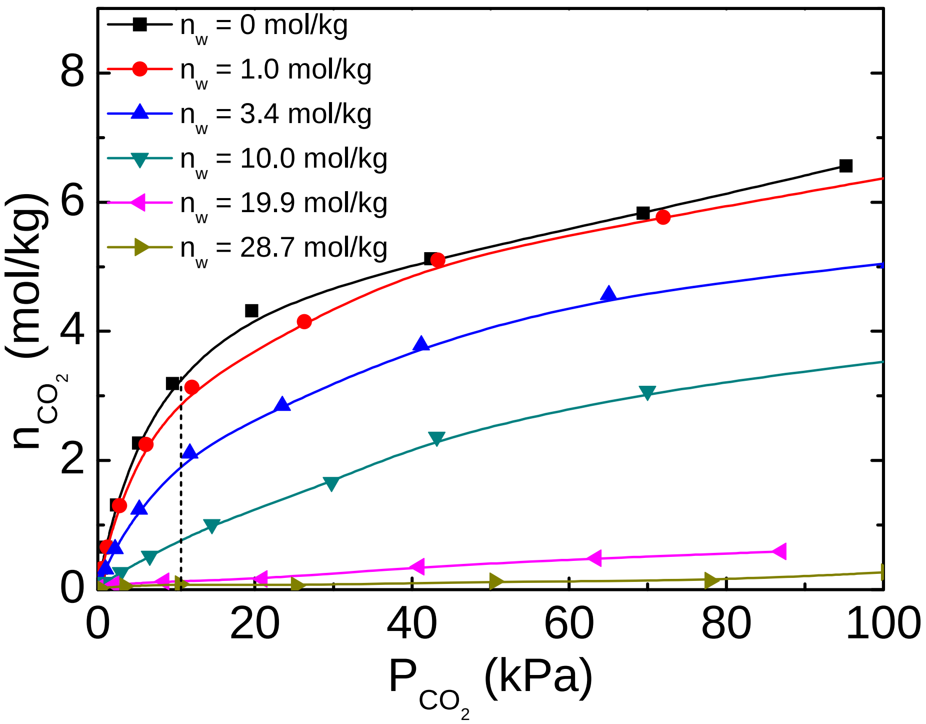

Figure 4.9: CO_2 isotherms at 25 °C for Ni/DOBDC pellet with different H_2O loadings. Curves are multi-temperature Toth equation fits.

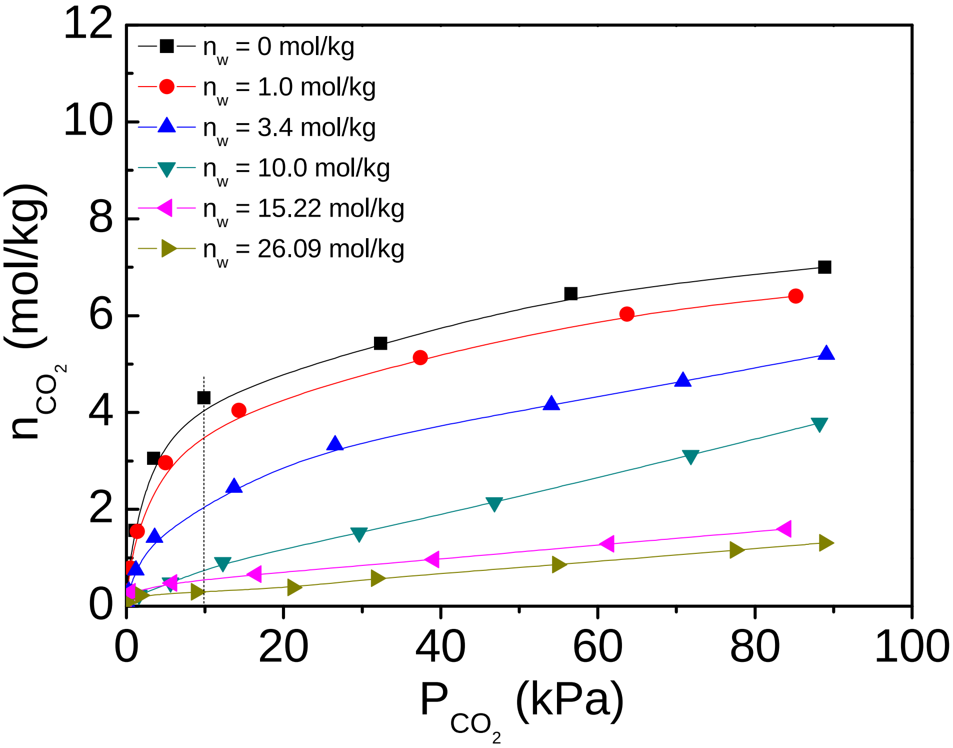

Figure 4.10: CO_2 isotherms at 25 °C for Mg/DOBDC pellet with different H_2O loadings. Curves are multi-temperature Toth equation fits.

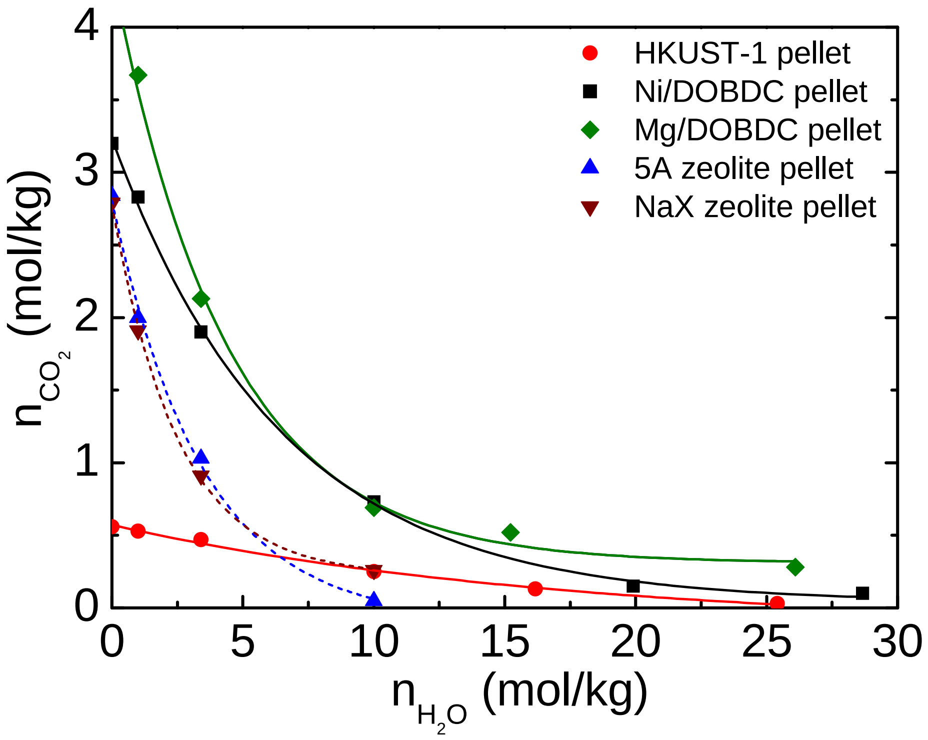

Figure 4.11: H_2O effects on CO_2 adsorption for MOF and zeolite pellets at 25 °C. Data points are CO_2 capacities at 0.1 atm for different samples at various H_2O loadings and lines are guides for the eyes. Zeolite results are taken from reference [26].

the comparable CO_2 capacity between the two DOBDC MOFs and the benchmark zeolites at 0.1 atm and 25 °C, the smaller water effect together with an easier regeneration process suggests that Ni/DOBDC and Mg/DOBDC may have a promising future in CO_2 capture from flue gas.

Although MOFs are usually synthesized through solvothermal reactions, the lack of hydrothermal stability is a disadvantage for some MOFs in comparison with traditional zeolites.[24] An extensive study has been reported recently on the hydrothermal stability of MOFs.[25] Experimental and simulation results obtained suggest that the strength of the bond between the metal oxide group and the organic linker determine the hydrothermal stability of MOFs.

In our study, pure CO_2 adsorption isotherms were measured at periodic intervals for the MOF samples over the course of H_2O and CO_2/H_2O mixture equilibrium measurements to investigate the effect of hydrothermal stability. The results are shown in Fig. 4.12. From Fig. 4.12a, it is clear that the CO_2 capacity of HKUST-1 decreases slightly after several runs, which means that HKUST-1 is somewhat prone to degradation after water vapor adsorption and heat treatments. However, as shown in Fig. 4.12b, Ni/DOBDC can better maintain its CO_2 capacity after multiple exposures to water vapor and multiple thermal regeneration processes. These results are consistent with the sequence of the transition state energies for hydration of Ni/DOBDC and HKUST-1 bonds in which transition state energies are positively related with the stabilities of MOF structures toward water.[25]

4.6 Simulated Flue Gas Conditioning

MOF samples were tested for CO_2 capacity at 0.1 atm and 25 °C before and after the simulated flue gas conditioning to reveal the effects of humidity and acid gases on performance. The result for HKUST-1 powder is shown in Fig. 4.13. Generally, the CO_2 capacities at 0.1 atm and 25 °C for HKUST-1 powder did not

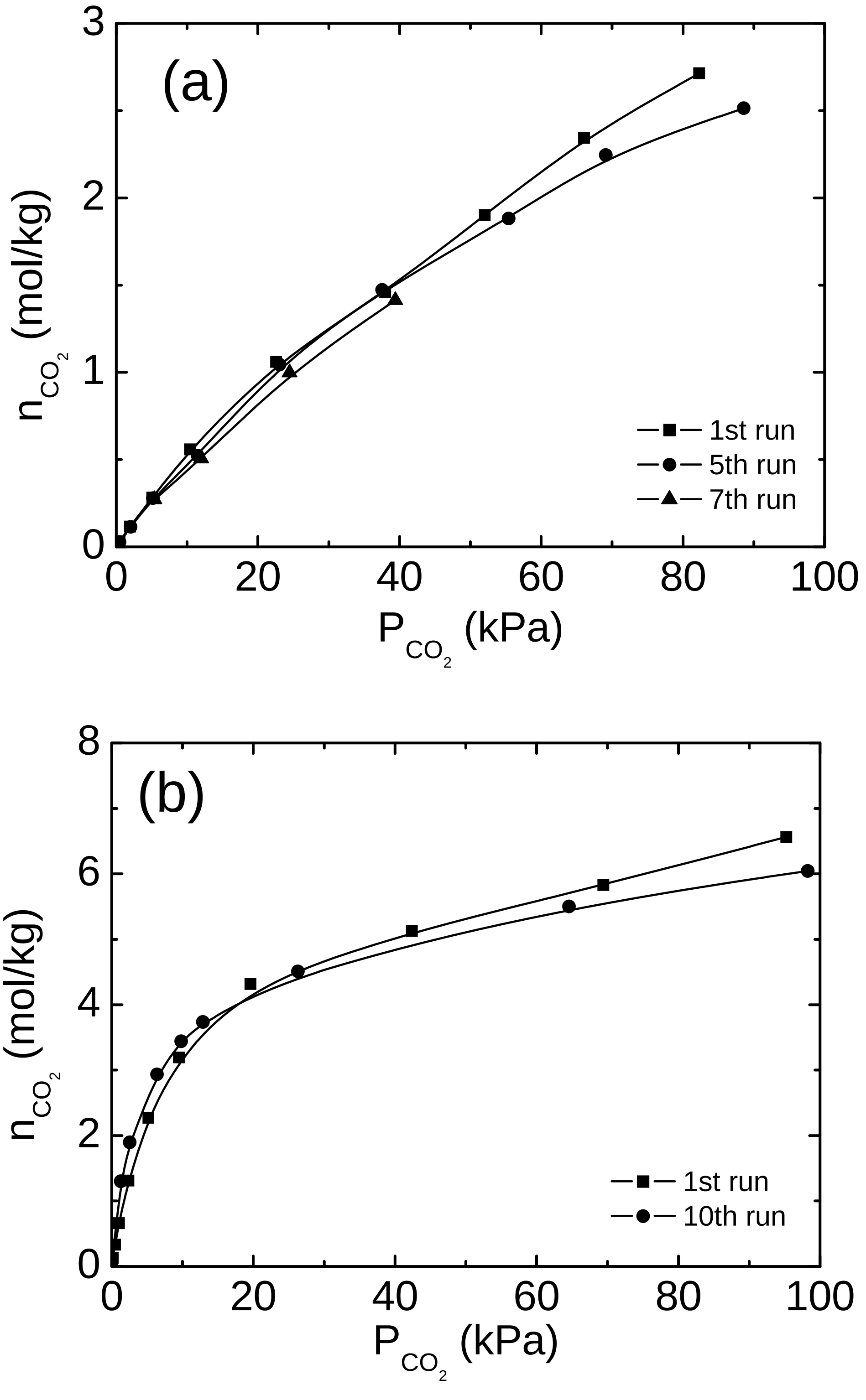

Figure 4.12: CO_2 isotherms at 25 °C for MOF samples at different stages. (a) HKUST-1 pellet; (b) Ni/DOBDC pellet. Lines are guides for the eyes.

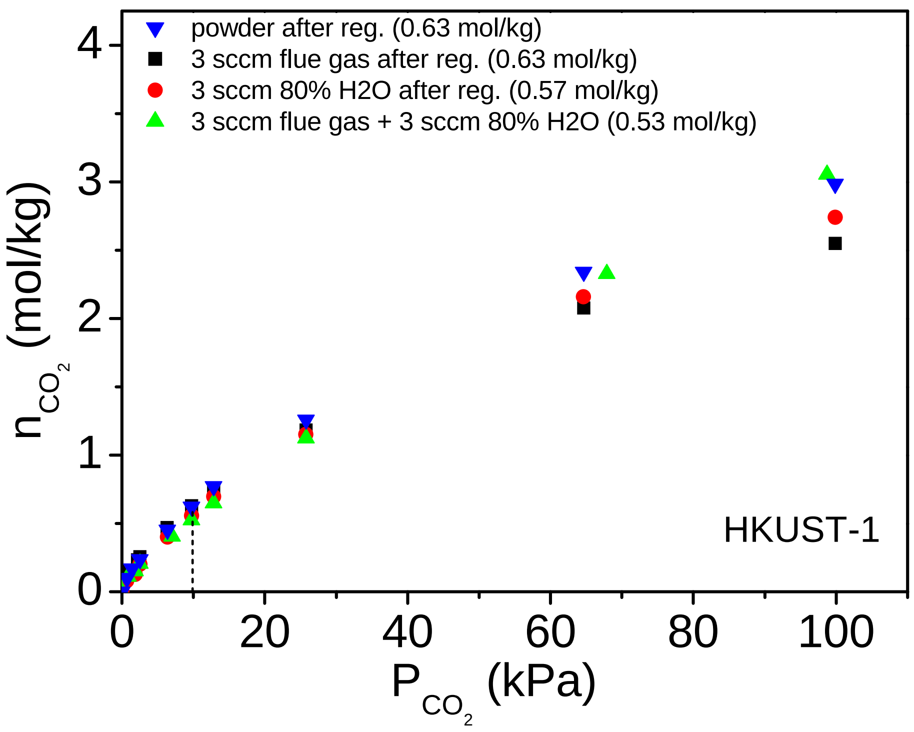

Figure 4.13: CO_2 isotherms at 25 °C for HKUST-1 pellet before and after different simulated flue gas conditionings.

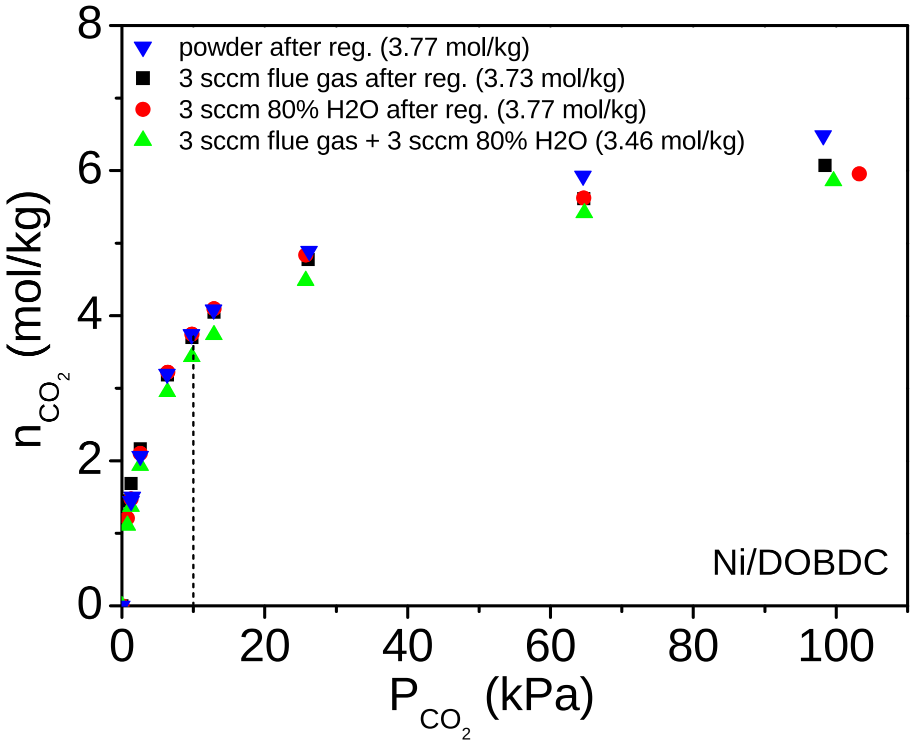

Figure 4.14: CO_2 isotherms at 25 °C for Ni/DOBDC pellet before and after different simulated flue gas conditionings.

change significantly after being conditioned with different simulated flue gases at room temperature. Note the numerical values shown in the figure for the CO_2 loading at 0.1 atm. It seems that flue gas at room temperature does not affect CO_2 adsorption in HKUST-1. However, moisture can impact the simulated flue gas conditioning effect for HKUST-1, as indicated by the reduced capacity of 0.53 mol/kg at 0.1 atm. Similar results were found for Ni/DOBDC as shown in Fig. 4.14.

4.7 Conclusions

Adsorption equilibria of CO_2, H_2O, and CO_2/H_2O were studied for HKUST-1, Ni/DOBDC, and Mg/DOBDC. Large CO_2 capacities are found at 25 °C and 0.1 atm CO_2 partial pressure. They are 0.55, 3.28, and 5.65 mol/kg for HKUST-1, Ni/DOBDC, and Mg/DOBDC pellets, respectively. Ni/DOBDC and Mg/DOBDC have higher CO_2 capacities than benchmark zeolites NaX and 5A at 25 °C and 0.1 atm.

Adsorbed water vapor impacts CO_2 adsorption in the MOFs. A small amount of H_2O does not decrease and may actually increase the CO_2 capacity of HKUST-1. H_2O does not affect CO_2 adsorption on HKUST-1 and Ni/DOBDC samples as much as on 5A and NaX zeolites, and H_2O would be more easily removed from the MOFs by regeneration. Ni/DOBDC and Mg/DOBDC retain substantial CO_2 capacities with moderate H_2O loadings. They may have a promising future for capturing CO_2 from flue gases provided that costs are not prohibitive.

References

[1] Breck, D. W. *Zeolite Molecular Sieves: Structure, Chemistry, and Use*; Wiley: New York, 1973.

[2] Brandani, F.; Ruthven, D. M. The Effect of Water on the Adsorption of CO_2 and C_3H_8 on Type X Zeolites. *Ind. Eng. Chem. Res.* **2004**, 43, 8339–8344.

[3] Kondo, A.; Daimaru, T.; Noguchi, H.; Ohba, T.; Kaneko, K.; Kanoh, H. Adsorption of Water on Three-Dimensional Pillared-Layer Metal Organic Frameworks. *J. Colloid Interface Sci.* **2007**, 314, 422–426.

[4] Gu, J. Z.; Lu, W. G.; Jiang, L.; Zhou, H. C.; Lu, T. B. 3D Porous Metal-Organic Framework Exhibiting Selective Adsorption of Water over Organic Solvents. *Inorg. Chem.* **2007**, 46, 5835–5837.

[5] Chen, Y.; Kondo, A.; Noguchi, H.; Kajiro, H.; Urita, K.; Ohba, T.; Kaneko, K.; Kanoh, H. Reversible Structural Change of Cu-MOF on Exposure to Water and Its CO_2 Adsorptivity. *Langmuir* **2009**, 25, 4510–4513.

[6] Wang, Q. M.; Sheng, D.; Bulow, M.; Lau, M. L.; Deng, S.; Fitch, F. R.; Lemcoff, N. O.; Semanscin, J. Metal-Organic Molecular Sieve for Gas Separation and Purification. *Microporous Mesoporous Mater.* **2002**, 55, 217–230.

[7] Castillo, J. M.; Vlugt, T. J. H.; Calero, S. *J. Phys. Chem. C* Understanding Water Adsorption in Cu-BTC Metal-Organic Frameworks. **2008**, 112, 15934–15939.

[8] Kusgens, P.; Rose, M.; Senkovska, I.; Frode, H.; Henschel, A.; Siegle, S.; Kaskel, S. Characterization of Metal-Organic Frameworks by Water Adsorption. *Microporous Mesoporous Mater.* **2009**, 120, 325–330.

[9] Yazaydin, A. O.; Benin, A. I.; Faheem, S. A.; Jakubczak, P.; Low, J. J.; Willis, R. R.; Snurr, R. Q. Enhanced CO_2 Adsorption in Metal-Organic Frameworks via Occupation of Open-Metal Sites by Coordinated Water Molecules. *Chem. Mater.* **2009**, 21, 1425–1430.

[10] Lee, K. B.; Sircar, S. Removal and Recovery of Compressed CO_2 from Flue Gas by a Novel Thermal Swing Chemisorption Process. *AIChE J.* **2008**, 54, 2293-2302.

[11] Rowsell, J. L. C.; Yaghi, O. M. Effects of Functionalization, Catenation, and Variation of the Metal Oxide and Organic Linking Units on the Low-Pressure Hydrogen Adsorption Properties of Metal-Organic Frameworks. *J. Am. Chem. Soc.* **2006**, 128, 1304–1315.

[12] Dietzel, P. D. C.; Panella B.; Hirscher, M. Blom, R.; Fjellvag, H. Hydrogen Adsorption in a Nickel Based Coordination Polymer with Open Metal Sites in the Cylindrical Cavities of the Desolvated Framework. *Chem. Commun.* **2006**, 9, 959–961.

[13] Caskey, S. R.; Wong-Foy, A. G.; Matzger, A. J. Dramatic Tuning of Carbon Dioxide Uptake via Metal Substitution in a Coordination Polymer with Cylindrical Pores. *J. Am. Chem. Soc.* **2008**, 130, 10870-10871.

[14] Minutillo, M.; Perna, A. A Novel Approach for Treatment of CO_2 from Fossil Fired Power Plants, Part A: The Integrated Systems ITRPP. *Int. J. Hydrogen Energy* **2009**, *34*, 4014–4020.

[15] Millward, A. R.; Yaghi, O. M. Metal-Organic Frameworks with Exceptionally High Capacity for Storage of Carbon Dioxide at Room Temperature. *J. Am. Chem. Soc.* **2006**, *127*, 17998–17999.

[16] Cavenati, S.; Grande, C. A.; Rodrigues, A. E. Metal Organic Framework Adsorbent for Biogas Upgrading. *Ind. Eng. Chem. Res.* **2008**, *47*, 6333-6335.

[17] Wang, Y.; LeVan, M. D. Adsorption Equilibrium of Carbon Dioxide and Water Vapor on Zeolites 5A and 13X and Silica Gel: Pure Components. *J. Chem. Eng. Data* **2009**, *54*, 2839–2844.

[18] Wu, H.; Zhou, W.; Yildrim, T. High-Capacity Methane Storage in Metal-Organic Frameworks M_2(dhtp): The Important Role of Open Metal Sites. *J. Am. Chem. Soc.* **2009**, *131*, 4995–5000.

[19] Forster, P. M.; Eckert, J.; Chang J. S.; Park, S. E.; Ferey, G.; Cheetham, A. K. Hydrogen Adsorption in Nanoporous Nickel(II) Phosphates. *J. Am. Chem. Soc.* **2009**, *125*, 1309–1312.

[20] Prestipino, C.; Regli, L.; Vitillo, J. G.; Bonino, F.; Damin, A.; Lamberti, C.; Zecchina, A.; Solari, P. L.; Kongshaug, K. O.; Bordiga, S. Local Structure of Framework Cu(II) in HKUST-1 Metallorganic Framework: Spectroscopic Characterization upon Activation and Interaction with Adsorbates. *Chem. Mater.* **2006**, *18*, 1337–1346.

[21] Yazaydin, A. O.; Snurr, R. Q.; Park, T. H.; Koh, K.; Liu, J.; LeVan, M. D.; Benin, A. I.; Jakubczak, P.; Lanuza, M.; Galloway, D. B; Low, J. J.; Willis, R. R. Screening of Metal-Organic Frameworks for Carbon Dioxide Capture from Flue Gas Using a Combined Experimental and Modeling Approach. *J. Am. Chem. Soc.* **2009**, *131*, 18198–18199.

[22] Chowdhury, P.; Bikkina, C.; Meister, D.; Dreisbach, F.; Gumma, S. Comparison of Adsorption Isotherms on Cu-BTC Metal Organic Frameworks Synthesized from Different Routes. *Microporous Mesoporous Mater.* **2009**, *117*, 406–413.

[23] Liu, J.; Wang, Y.; Benin, A. I.; Jakubczak, P.; Willis, R. R.; LeVan, M. D. CO_2/H_2O Adsorption Equilibrium and Rates on Metal-Organic Frameworks: HKUST-1 and Ni/DOBDC. *Langmuir* **2010**, *26*, 14301–14307.

[24] Sabo, M.; Henschel, A.; Frode, H.; Klemm, E.; Kaskel, S. Solution Infiltration of Palladium into MOF-5: Synthesis, Physisorption and Catalytic Properties. *J. Mater. Chem.* **2007**, *17*, 3827–3832.

[25] Low, J. J.; Benin, A. I.; Jakubczak, P.; Abrahamian, J. F.; Faheem, S. A.; Willis, R. R. Virtual High Throughput Screening Confirmed Experimentally: Porous Coordination Polymer Hydration. *J. Am. Chem. Soc.* **2009**, *131*, 15834–15842.

[26] Wang, Y.; LeVan, M. D. Adsorption Equilibrium of Binary Mixtures of Carbon Dioxide and Water Vapor on Zeolites 5A and 13X. *J. Chem. Eng. Data* **2010**, *55*, 3189–3195.

CHAPTER V

ISOSTERIC HEATS OF ADSORPTION IN THE HENRY'S LAW RE GION FOR CARBON SINGLE WALL CYLINDRICAL NANOPORES AND SPHEREICAL NANOCAVITIES

5.1 Introduction

Knowledge of isotherms and heats of adsorption are crucial for the optimal design of adsorption processes. These provide important information about capacities at given pressures, heat effects, and ease of regeneration. The isosteric heat of adsorption is also useful for studies of adsorption selectivities.

The Henry's law region for adsorption is the low loading region where the isotherm is linear. In the absence of steric hindrance each gas molecule can explore every adsorption site on the whole surface of the adsorbent, and the molecules will associate preferentially with the adsorption sites with the highest energies. Adsorbate-adsorbate interactions are neglected when considering potential energies for adsorption because of infinitesimal adsorbed-phase concentrations in the Henry's law region. Therefore, it is sufficient to calculate $q_{\mathrm{st}}^{\mathrm{o}}$ only from adsorbent-adsorbate interactions. In particular, $q_{\mathrm{st}}^{\mathrm{o}}$ can be determined as a function of pore width when a Lennard-Jones (LJ) type fluid is adsorbed on non-polar homogeneous surfaces such as ideal carbon surfaces.

As many efforts are ongoing on the synthesis of novel carbonaceous materials, including carbon nanotubes, carbon fibers, and carbon-silica composites, knowledge of the isosteric heat of adsorption for a molecule as a function of pore width is of great importance in the design and application of these novel materials. Steele[1] proposed an equation based on statistical thermodynamics to calculate $q_{\mathrm{st}}^{\mathrm{o}}$ for gas adsorption on a flat graphite surface. Steele's equation has been applied by many scientists to study the adsorption of various gases on graphite surfaces and to calculate $q^{\mathrm{o}}_{\mathrm{st}}$.[2,3] In addition, Do *et al.*[4] used the Monte Carlo method to calculate the Henry's law constant and isosteric heat of adsorption at zero loading for argon adsorption in carbon nanotubes. Floess and VanLishout[5] calculated $q^{\mathrm{o}}_{\mathrm{st}}$ for argon as a function of pore width for slit-shaped carbon pores. They found the maximum $q^{\mathrm{o}}_{\mathrm{st}}$ at 6.8 Å by integrating the LJ 12-6 potential into the walls of the adsorbent to a depth of three carbon layers. Schindler and LeVan[6] calculated $q^{\mathrm{o}}_{\mathrm{st}}$ as a function of the pore width for nitrogen, argon, carbon dioxide, methane, helium, and hydrogen adsorption in slit shape carbon nanopores by using Steele's 10-4-3 equation. They determined the pore widths where $q^{\mathrm{o}}_{\mathrm{st}}$ is a maximum as well as the pore widths where $q^{\mathrm{o}}_{\mathrm{st}}$ is equal to zero. Their calculation results of maximum $q^{\mathrm{o}}_{\mathrm{st}}$ are somewhat larger than the results obtained from experiments in which pore size distributions always lower the maximum $q^{\mathrm{o}}_{\mathrm{st}}$, because only one pore size corresponds to the maximum $q^{\mathrm{o}}_{\mathrm{st}}$.[7] They also presented a general plot giving the pore width where the maximum $q^{\mathrm{o}}_{\mathrm{st}}$ occurs for various gas molecules based on LJ parameters.

In this paper, we expand the calculation of $q^{\mathrm{o}}_{\mathrm{st}}$ as a function of pore width to carbon single wall cylindrical nanopores and spherical nanocavities. The focus of this study is on the effect of LJ parameters and geometrical factors on the isosteric heat of adsorption. This is in contrast to an early study by Everett and Powl[8] on the adsorption potential calculation in slit and cylindrical micropores in which several models for the external wall potential are analyzed, some in combination with experimental data, and used to support a possible polymer crystal model for the microporosity of the activated carbon. The pore width where $q^{\mathrm{o}}_{\mathrm{st}}$ is a maximum will be determined in our paper, and the influence of geometry on the theoretical $q^{\mathrm{o}}_{\mathrm{st}}$ will also be studied. The theoretical maximum $q^{\mathrm{o}}_{\mathrm{st}}$ for cylindrical carbon nanopores will be compared with experimental and simulation adsorption data for single-wall carbon nanotubes (SWNTs).

5.2 Theory

The theoretical isosteric heat of adsorption will be calculated for various gases on model cylindrical and spherical carbon surfaces, which can represent the internal surface for unbundled SWNTs and fullerene (with allowance for an opening into the spherical cavity). Gas molecules interact much more strongly with the internal surface of a SWNT than with the outside surface in the Henry's law region.[9] Therefore, we only consider the solid-fluid interactions that occur on the internal surfaces in our study.

The isosteric heat of adsorption is calculated by using the Clausius-Clapeyron equation at constant adsorbed-phase concentration

$$q_{\mathrm{st}} = RT^2 \left. \frac{\partial \ln P}{\partial T} \right|_n \tag{5.1}$$

where R is the ideal gas constant, T is temperature, and P is pressure. In the Henry's law region with the isotherm written $n = K_{\mathrm{H}}(T)\, P$, equation 5.1 becomes

$$q_{\mathrm{st}}^{o} = -RT^2 \frac{d \ln K_{\mathrm{H}}}{dT} \tag{5.2}$$

Clearly, the right hand side of this equation is independent of n. Thus, the isosteric heat of adsorption is independent of loading in the Henry's law region.

When the mutual interactions of the adsorbed molecules can be omitted, Steele[1] wrote the Henry's law constant as

$$K_{\mathrm{H}} = \frac{1}{A} \left(\frac{Z_1^{(\mathrm{s})}}{kT} \right) \tag{5.3}$$

where k is Boltzman's constant, and A is the surface area of the adsorbent. The configuration integral for one molecule is

$$Z_1^{(\mathrm{s})} = \int_{\mathrm{V}^{(\mathrm{s})}} \exp[-V_{\mathrm{ext}}(\mathbf{r}_1)/kT]\; d\mathbf{r}_1 \tag{5.4}$$

where $\mathbf{r}_1$ is the position vector and $\mathrm{V}^{(\mathrm{s})}$ is the volume of the adsorbed phase. Substituting equation 5.3 and 5.4 into equation 5.2 we obtain

$$q_{\mathrm{st}}^{\mathrm{o}} = RT - N_{\mathrm{a}} \frac{\int_{\mathrm{V}^{(\mathrm{s})}} V_{\mathrm{ext}}(\mathbf{r}_i) \exp[-V_{\mathrm{ext}}(\mathbf{r}_i)/kT] \; d\mathbf{r}_i}{\int_{\mathrm{V}^{(\mathrm{s})}} \exp[-V_{\mathrm{ext}}(\mathbf{r}_i)/kT] \; d\mathbf{r}_i} \tag{5.5}$$

where N_{a} is Avagadro's number and $V_{\mathrm{ext}}(\mathbf{r}_i)$ is the external wall potential, which we use to describe the interactions between fluid molecules and adsorbents in the Henry's law region.

It should be noted that equation 6.5 gives the average isosteric heat for molecules contained within the adsorption volume, and in our case, the isosteric heat for a single molecule averaged statistically over all possible locations within that volume. Comments on the application of this equation to large simulation volumes in which many molecules may be essentially unadsorbed have been provided recently by Do et al.[10] In our application, we are concerned primarily with geometries in which heats of adsorption are large, with tight confinement of molecules in pores and cavities.

The external wall potential has different expressions for different geometries. Tjatjopoulos[11] developed an interaction potential for cylindrical pores by using the LJ potential energy expression

$$\Gamma_{\mathrm{sf}} = 4\epsilon_{\mathrm{sf}} \left[\left(\frac{\sigma_{\mathrm{sf}}}{r} \right)^{12} - \left(\frac{\sigma_{\mathrm{sf}}}{r} \right)^{6} \right] \tag{5.6}$$

where ϵ_{sf} and σ_{sf} are the solid-fluid well depth potential and the solid-fluid collision diameter, respectively, and r is the interatomic separation. Then, the external interaction potential for a molecule adsorbed on a surface of area A and atom number density n_{s} is given by

$$V_{\mathrm{ext}} = \int_A \Gamma_{\mathrm{sf}} \, n_{\mathrm{s}} \; dA \tag{5.7}$$

The carbon atoms are assumed to be located uniformly over the cylindrical surface with a given surface number density. A pore diagram is shown in Fig. 5.1(a). H_{c} is the distance between the center of the carbon atoms on opposing walls of the pore, which will be referred to below as pore diameter. $H = H_\mathrm{c} - \sigma_\mathrm{ss}$ is the distance between the surfaces of carbon atoms on opposing walls (i.e., the inside diameter), which will be referred to below as pore width. The size of a carbon atom is $\sigma_\mathrm{ss} = 3.38$ Å. Substituting equation 5.6 into equation 5.7 and integrating the resulting equation over z and ϕ using $r^2 = z^2 + \rho^2 + R^2 - 2\rho R \cos\phi$, the external interaction potential for a cylindrical carbon surface is

$$\begin{aligned} V_\text{ext, cyl} = & n_\mathrm{s}\pi^2\epsilon_\mathrm{sf}\sigma_\mathrm{sf}^2 \left\{ \frac{63}{32}\left[\frac{R-\rho}{\sigma_\mathrm{sf}}\left(1+\frac{\rho}{R}\right)\right]^{-10} \times F\left[-\frac{9}{2}, -\frac{9}{2}; 1; \left(\frac{\rho}{R}\right)^2\right] \right. \\ & \left. -3\left[\frac{R-\rho}{\sigma_\mathrm{sf}}\left(1+\frac{\rho}{R}\right)\right]^{-4} \times F\left[-\frac{3}{2}, -\frac{3}{2}; 1; \left(\frac{\rho}{R}\right)^2\right] \right\} \end{aligned} \tag{5.8}$$

where R is the radius of the cylinder measured from the center of the cylinder to the center of the carbon atoms in the wall, ρ is the perpendicular distance between the center of a fluid molecule and the center axis of the cylinder, and $F[\alpha, \beta; \gamma; z]$ denotes the hypergeometric series with parameters α, β, and γ.[12]

Besides the fluid-fluid parameters and solid-fluid parameters, which can be obtained from the literature, we need the surface number density to calculate the external wall potential. In this paper, we estimate the surface number density of carbon atoms on a cylindrical surface based on the graphite crystal structure. A SWNT can be viewed as a rolled graphite sheet. Therefore, the surface number density of carbon atom in a SWNT can be estimated by unfolding the nanotube back to a graphite sheet and calculating the surface number density of the flat sheet as shown in Fig. 5.2. The bold hexagon, which sits over a six carbon member ring, is chosen as the unit structure. The distance between the neighboring points in the hexagon is the length of a carbon-carbon bond, which is known to be 1.42 Å.[13] The unit structure contains two carbon atoms, and the surface area can be calculated based on the border length of the hexagon. Thus, the surface number density can be estimated to be 3.82×10^{19} m^{-2}.

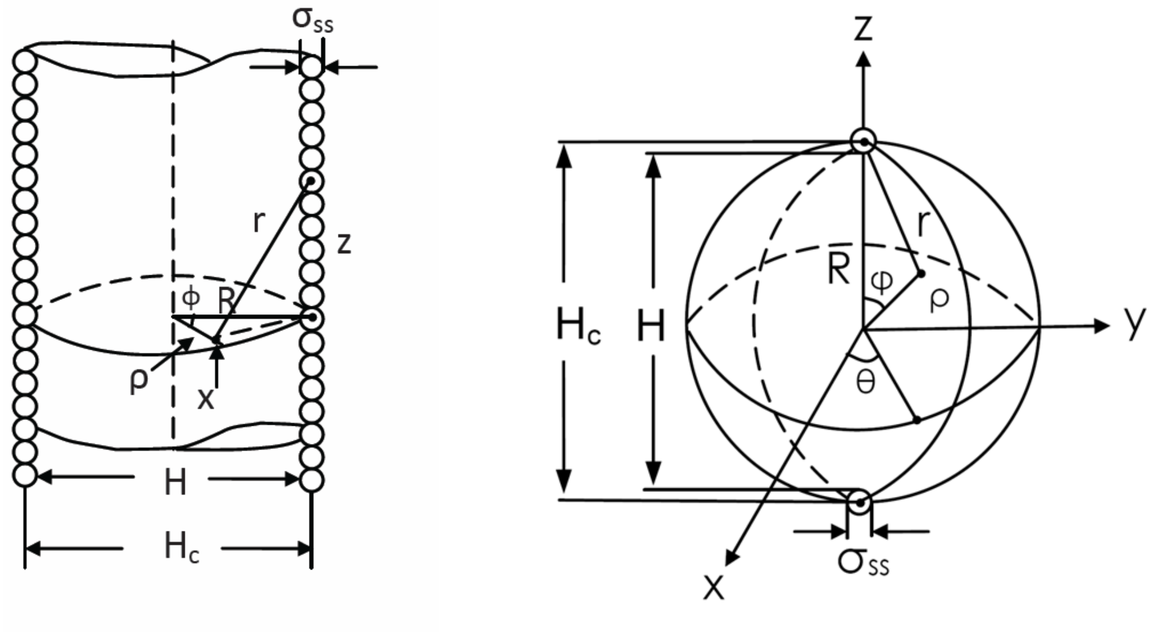

(a) (b)

Figure 5.1: Diagrams of carbon nanopore and nanocavity. (a) Cylindrical pore; (b) Spherical cavity.

For a spherical surface, the pore diagram is shown in Fig. 5.1(b). The pore diameter H_c is the distance between the center of the carbon atoms on opposing walls of the pore. The pore width is again $H = H_\mathrm{c} - \sigma_\mathrm{ss}$. Baksh and Yang[14] developed an interaction potential for spherical pores by using the LJ potential. They started their derivation from the expression

$$V_\mathrm{ext} = \int_0^{2\pi} \int_0^{\pi} n_\mathrm{s}\, \Gamma_\mathrm{sf}\, R^2 \sin\phi \; d\phi \; d\theta \tag{5.9}$$

Substituting $r^2 = R^2 + \rho^2 - 2\rho R \cos\phi$ into the above equation and integrating it over ϕ and θ gives

$$\begin{aligned} V_\text{ext, sph} = 8\pi R^2 n_\mathrm{s} \epsilon_\mathrm{sf} \Bigg[& -\left(\frac{\sigma_\mathrm{sf}}{R}\right)^6 \frac{1}{4\,(\rho/R)} \left(\frac{1}{(1-\rho/R)^4} - \frac{1}{(1+\rho/R)^4} \right) \\ & + \left(\frac{\sigma_\mathrm{sf}}{R}\right)^{12} \frac{1}{10\,(\rho/R)} \left(\frac{1}{(1-\rho/R)^{10}} - \frac{1}{(1+\rho/R)^{10}} \right) \Bigg] \end{aligned} \tag{5.10}$$

where R is the radius of the spherical nanocavity, measured from the center of the nanocavity to the center of the carbon atoms in the wall, and ρ is the distance between the center of a fluid molecule and the center of the cavity. Only the internal surface is considered to be active for adsorption in our study, and an opening is assumed to exist into the nanocavity. The surface number density of carbon atoms for a fullerene (C60) molecule can be estimated to be 4.10×10^{19} m^{-2} by using a method similar to that used for the SWNT.

5.3 Results and Discussion

We determine q_st^o for six different gas molecules: argon, methane, carbon dioxide, hydrogen, helium, and nitrogen. The LJ potential has an effective interaction distance because the repulsive and attractive forces are short-distance forces. The LJ solid-fluid parameters used to describe the gas molecules were obtained from the literature[6] and are given in Table 5.1.

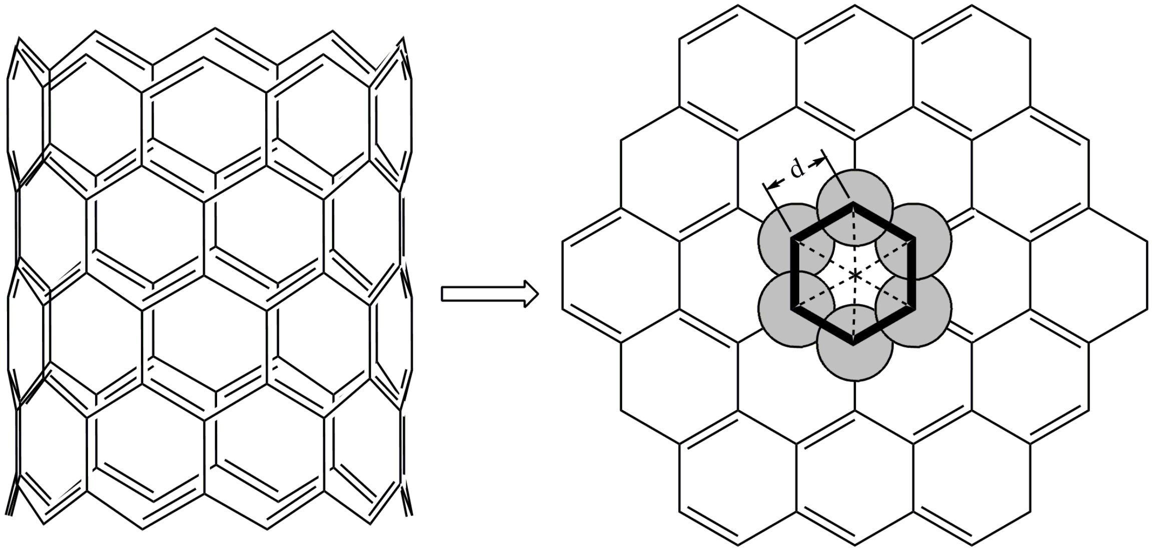

Figure 5.2: Surface number density of SWNT determined from graphite sheet.

Table 5.1: Model parameters for different molecules.

Molecule	σ_{ff} (Å)	ϵ_{ff}/k (k)	σ_{sf} (Å)	ϵ_{sf}/k (k)	Ref.
Ar	3.305	118.05	3.35	55.0	Ref[15]
CH_4	3.82	148.2	3.60	64.4	Ref[16]
CO_2	3.454	235.9	3.43	81.5	Ref[15]
H_2	2.83	59.7	3.10	40.87	Ref[17]
He	2.56	10.21	2.98	16.90	Ref[1]
N_2	3.575	94.45	3.494	53.22	Ref[15]

In the original sources, the solid-fluid parameters for argon, methane, carbon dioxide, and nitrogen had been determined by fitting the LJ equation of state to experimental vapor-liquid equilibrium data. The solid-fluid parameters for helium and hydrogen had been calculated using the Lorentz-Berthelot mixing rules

$$\sigma_{\text{sf}} = \left(\sigma_{\text{ff}} + \sigma_{\text{ss}}\right)/2 \quad \text{and} \quad \epsilon_{\text{sf}} = \sqrt{\epsilon_{\text{ff}}\epsilon_{\text{ss}}} \tag{5.11}$$

where $\epsilon_{\text{ss}}/k = 27.97$ K. We determine the pore width where the isosteric heat of adsorption is a maximum and where it is zero for each of the six gas molecules for both carbon cylindrical nanopores and spherical nanocavities, as was done by Schindler and LeVan for slit-shaped carbon nanopores.[6]

Cylindrical carbon nanopore

The results for the calculated isosteric heat of adsorption for a cylindrical carbon nanopore are shown in Fig. 5.3(a) as a function of pore width H and in Fig. 5.3(b) as a function of dimensionless pore diameter, which is the ratio of pore diameter H_{c} to σ_{sf}. Each curve has a single peak, which corresponds to the maximum isosteric heat of adsorption. The steep branch on the left hand side of the maximum point shows rapid change of q_{st}^{o} with pore width. As the pore becomes larger, q_{st}^{o} declines gradually.

The results are summarized in Table 5.2. The maximum $q_{\mathrm{st}}^{\mathrm{o}}$ for argon adsorption in a cylindrical carbon nanopore was found for a pore width of 3.92 Å. The maximum value, 26.45 kJ/mol, is slightly larger than the result that Do and co-authors[4] obtained for argon adsorption inside carbon nanotubes, which was about 25.50 kJ/mol for a 4.07 Å pore, by using Monte Carlo integration. The small difference in maximum $q_{\mathrm{st}}^{\mathrm{o}}$ may be caused by the different calculation methods and parameters.

We compare our results for other gas molecules with data from experimental or simulation studies in Table 5.2. Many of our results for $q_{\mathrm{st}}^{\mathrm{o}}$ are significantly larger than experimental data from the literature. However, most of the experimental results are average isosteric heats of adsorption rather than the maximum isosteric heat of adsorption because of the pore size distributions of real adsorbents. Although some simulation studies reported the maximum $q_{\mathrm{st}}^{\mathrm{o}}$, the pore widths corresponding to the maximum $q_{\mathrm{st}}^{\mathrm{o}}$ are different from the pore widths that we determined. Therefore, it is natural that the two maximum isosteric heats of adsorption are different since $q_{\mathrm{st}}^{\mathrm{o}}$ is a strong function of pore width, especially in certain regions as shown in Fig. 5.3(a). For example, the maximum $q_{\mathrm{st}}^{\mathrm{o}}$ we obtained for nitrogen in a cylindrical carbon nanopore at 298.15 K is 27.76 kJ/mol for a pore of width 4.22 Å. The maximum $q_{\mathrm{st}}^{\mathrm{o}}$ obtained by Jiang and Sandler[18] in their simulation study for nitrogen in isolated carbon nanotubes at 77 K is about 16.80 kJ/mol for a pore of width 6.80 Å. However, if we change the temperature in our study to calculate $q_{\mathrm{st}}^{\mathrm{o}}$ for nitrogen adsorption in a cylindrical carbon nanopore as a function of pore width at 77 K, the value of $q_{\mathrm{st}}^{\mathrm{o}}$ we obtain for a 6.80 Å pore is 16.09 kJ/mol, which becomes comparable to the result of Jiang and Sandler.

It is interesting to note from Table 5.2 that the dimensionless pore diameter where $q_{\mathrm{st}}^{\mathrm{o}}$ is a maximum for all the six gas molecules is close to 2.18, and the dimensionless pore diameter where $q_{\mathrm{st}}^{\mathrm{o}}$ is zero for all the six gas molecules is close to 1.86. As a matter of fact, Schindler and LeVan[6] found the dimensionless pore diameter where

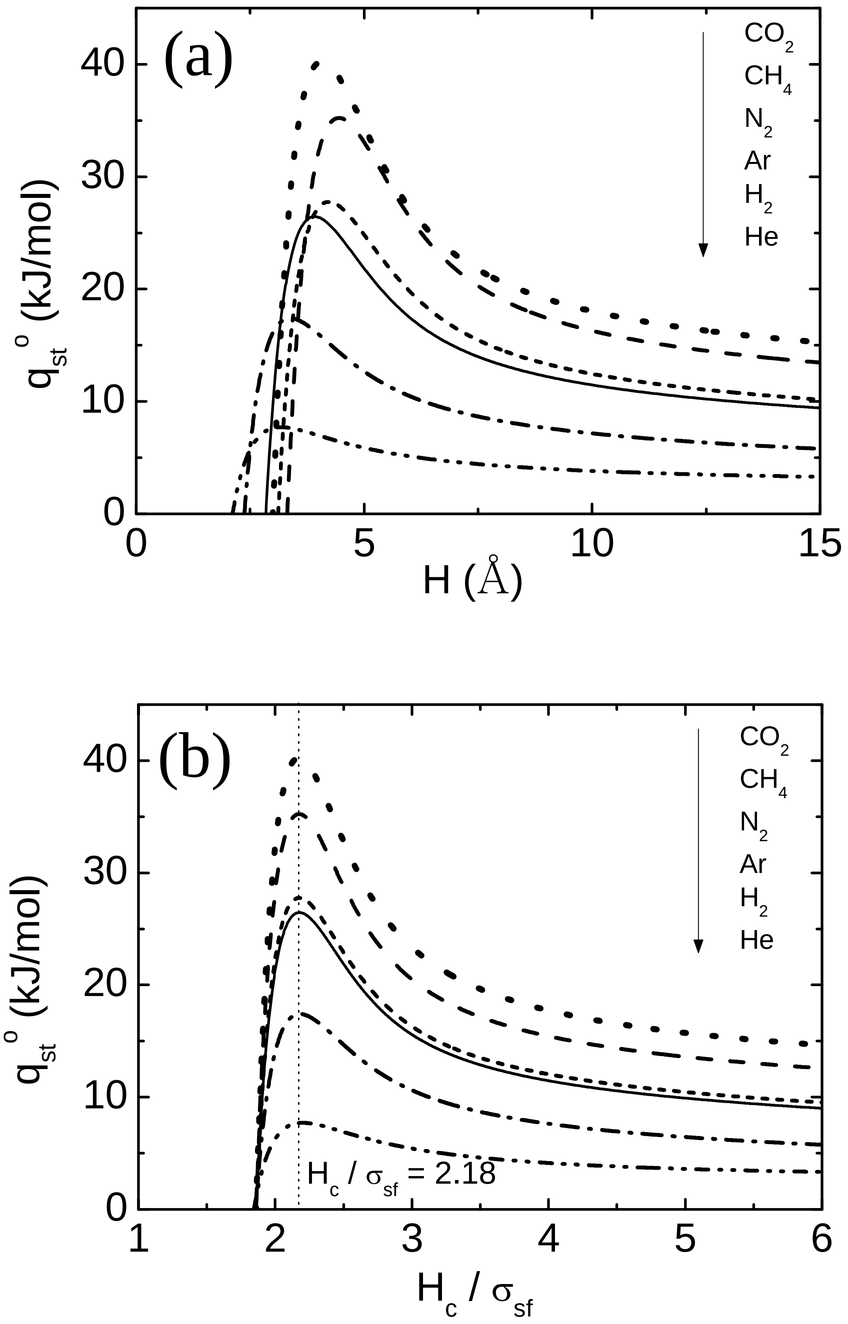

Figure 5.3: Isosteric heat of adsorption as a function of pore width and dimensionless pore diameter in cylindrical carbon nanopore. (a) pore width results; (b) dimensionless pore diameter results.

Table 5.2: Isosteric heat of adsorption in the Henry's law region for cylindrical carbon nanopores.

Molecule	Pore width of maximum q^{o}_{st}, H_{max}(Å)	$H_{c\ max}/\sigma_{sf}$	Pore width of zero q^{o}_{st}, H_{zero} (Å)	$H_{c\ zero}/\sigma_{sf}$	Maximum q^{o}_{st} (kJ/mol)	q^{o}_{st} from data (kJ/mol)	Ref.
Ar	3.92	2.18	2.84	1.86	26.45	25.50(S)*	Ref[4]
CH_4	4.45	2.18	3.32	1.86	35.24	24.12(E), 18.3(E)	Ref[19,20]
CO_2	4.08	2.18	3.00	1.86	40.26	22.5(E)	Ref[20]
H_2	3.38	2.18	2.37	1.86	17.41	7.5(E)	Ref[20]
He	3.18	2.20	2.12	1.84	7.72	3.58(E)	Ref[21]
N_2	4.22	2.18	3.12	1.86	27.76	16.80(S), 9.17(E)	Ref[18,22]

* (S) simulation data; (E) experimental data maximum $q_{\mathrm{st}}^{\mathrm{o}}$ occurs in slit-shaped carbon nanopores to be close to 2.0. According to their study, the pore width for maximum $q_{\mathrm{st}}^{\mathrm{o}}$ is a weak function of the well depth parameters for most of the cases in which ϵ_{sf}/k is larger than 20 K. In other words, the influence of well depth parameters on the pore width for maximum $q_{\mathrm{st}}^{\mathrm{o}}$ could be neglected for most situations. Therefore, it is convenient to predict the pore diameters for the maximum and zero value of $q_{\mathrm{st}}^{\mathrm{o}}$ by using only the solid-fluid parameters of specific gas molecules. The estimation accuracy depends on the accuracy of the accessible LJ solid-fluid parameter data.

Spherical carbon nanocavity

The results for the calculated isosteric heat of adsorption in spherical carbon nanopores is shown in Fig. 5.4(a) as a function of pore width H and in Fig. 5.4(b) as a function of dimensionless pore diameter. The shapes of the curves are similar to those in the cylindrical case. However, generally higher maximum $q_{\mathrm{st}}^{\mathrm{o}}$ are found, which shows that a spherical carbon nanocavity is more attractive to gas molecules than is a cylindrical carbon nanopore.

We also found a roughly constant dimensionless pore diameter for the maximum and zero value of $q_{\mathrm{st}}^{\mathrm{o}}$ for all six gas molecules, as shown in Table 5.3. The average values for the two dimensionless pore diameters are 2.33 and 2.00, respectively. Including the dimensionless pore diameters for the maximum and zero value of $q_{\mathrm{st}}^{\mathrm{o}}$ that Schindler and LeVan found in their study for slit-shaped carbon nanopores, all of the carbon nanopores with three different geometries, slit-shaped, cylindrical and spherical, have essentially constant dimensionless pore diameters for those isosteric heats as indicated in Table 5.4.

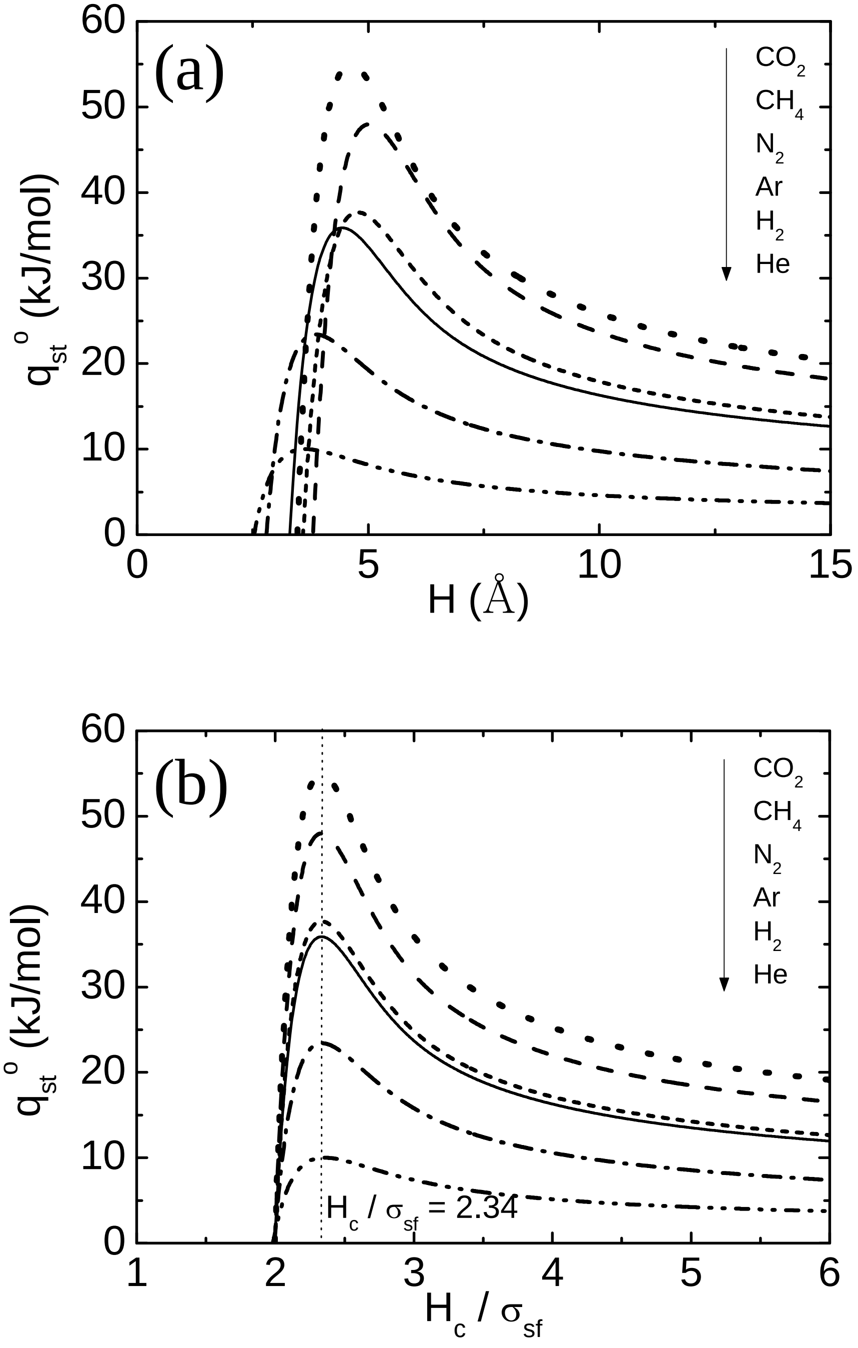

Figure 5.4: Isosteric heat of adsorption as a function of pore width and dimensionless pore diameter in spherical carbon nanocavity. (a) pore width results; (b) dimensionless pore diameter results.

Table 5.3: Isosteric heat of adsorption in the Henry's law region for spherical carbon nanocavities.

Molecule	Pore width of maximum q^{o}_{st}, H_{max}(Å)	$H_{c\ max}/\sigma_{sf}$	Pore width of zero q^{o}_{st}, H_{zero} (Å)	$H_{c\ zero}/\sigma_{sf}$	Maximum q^{o}_{st} (kJ/mol)
Ar	4.44	2.33	3.30	2.00	35.87
CH_4	5.02	2.33	3.81	2.00	47.97
CO_2	4.62	2.33	3.47	2.00	54.89
H_2	3.86	2.34	2.80	1.99	23.41
He	3.64	2.35	2.53	1.98	10.01
N_2	4.77	2.33	3.59	2.00	37.68

Table 5.4: Empirical constant relationships between pore diameter for maximum and zero $q^{\mathrm{o}}_{\mathrm{st}}$ for different geometries.

Geometry	Average dimensionless pore diameter for $q^{\mathrm{o}}_{\mathrm{st}} = \max$ $H_{\mathrm{c\ max}}/\sigma_{\mathrm{sf}}$	Average dimensionless pore diameter for $q^{\mathrm{o}}_{\mathrm{st}} = 0$ $H_{\mathrm{c\ zero}}/\sigma_{\mathrm{sf}}$
Slit-shaped	2.00	1.71
Cylindrical	2.18	1.86
Spherical	2.33	2.00

LJ parameter effects

As indicated from our equation set, $q^{\mathrm{o}}_{\mathrm{st}}$ in our study is determined from only the LJ parameters σ_{sf} and ϵ_{sf}/k when the temperature and surface number density are fixed. In order to understand the constant relationships between the pore diameters for the maximum heats of adsorption and σ_{sf}, we produce a set of general plots for all three geometries based on the calculation results of $q^{\mathrm{o}}_{\mathrm{st}}$ for a broad range of LJ parameters. This is shown in Fig. 5.5. The range for the LJ parameters was chosen basing on LJ parameter data for normal gases in the literature.[17] The y-axis in the figure is the ratio of the pore diameter for the maximum $q^{\mathrm{o}}_{\mathrm{st}}$ to the specific σ_{sf}, which will be referred to below as dimensionless pore diameter for the maximum $q^{\mathrm{o}}_{\mathrm{st}}$.

In Fig. 5.5, we can clearly see a band of curves for each of the three geometries. Each curve in a band displays results that corresponding to one σ_{sf} and the whole range of ϵ_{sf}/k values. The dimensionless pore diameter for the maximum $q^{\mathrm{o}}_{\mathrm{st}}$ for each pair of LJ parameters in the three geometries gradually decreases and approaches a constant at modest values of ϵ_{sf}/k. This indicates that the dimensionless pore diameter for the maximum $q^{\mathrm{o}}_{\mathrm{st}}$ is nearly independent of ϵ_{sf}/k when ϵ_{sf}/k is larger than 20 K, which is consistent with the results found by Schindler and LeVan.[6]

The finding above is also confirmed by a sensitivity analysis. Taking argon in a cylindrical pore as an example, the sensitivities of the maximum $q^{\mathrm{o}}_{\mathrm{st}}$ and the

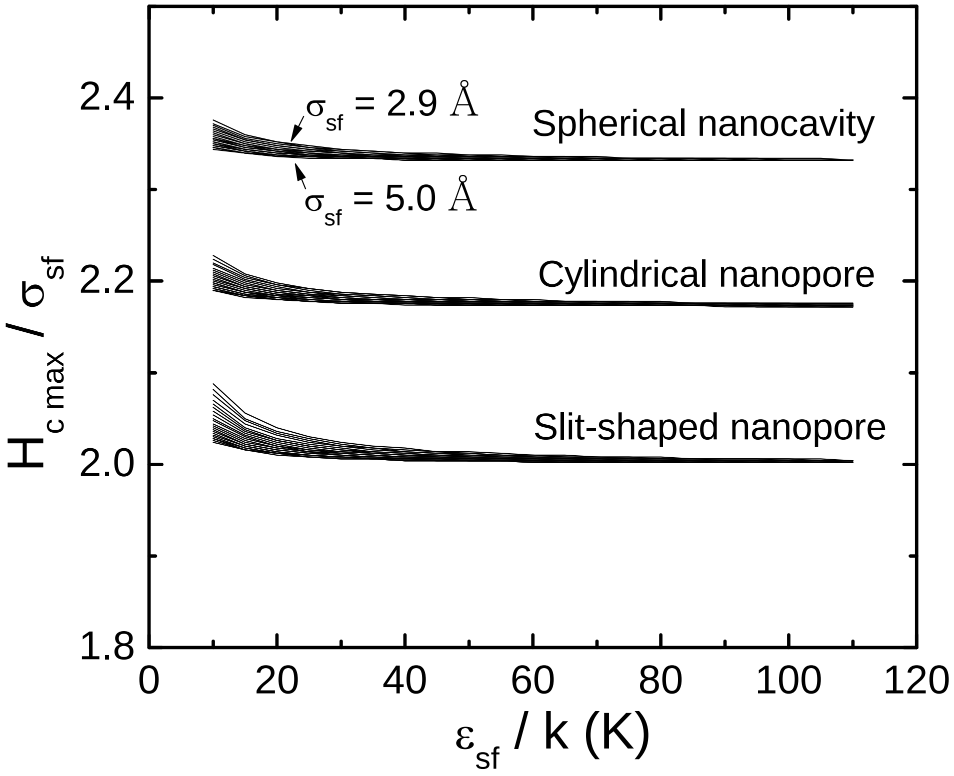

Figure 5.5: The effect of LJ parameters on the pore diameter for the maximum q^{o}_{st} for the three geometries. σ_{sf} increases from 2.9 Å to 5.0 Å (top to bottom) for each geometry.

dimensionless pore diameter for the maximum q_{st}^{o} to changes in σ_{sf} are 1.88 and 4.3×10^{-4} (i.e., $\partial q_{\text{st}}^{\text{o}}/\partial\sigma_{\text{sf}} = 1.88$, etc.). Similarly, the sensitivities of these same respective quantities to changes in ϵ_{sf}/k are 0.94 and -3.6×10^{-3}. Thus, while the maximum q_{st}^{o} is sensitive to σ_{sf} and ϵ_{sf}/k, the dimensionless pore diameter is nearly independent of both σ_{sf} and ϵ_{sf}/k. These findings agree well with what is shown in Fig. 5.5.

The constant dimensionless pore diameters for the maximum q_{st}^{o}, determined from Fig. 5.5, are 2.00, 2.18, and 2.33 for the slit-shaped nanopore, the cylindrical nanopore, and the spherical nanocavity, respectively. The interesting result that these differ significantly can be explained in terms of geometrical effects. For the slit-shaped pore, as the distance between the parallel walls changes, a confined molecule still is influenced by the same number of carbon atoms in the walls. However, as the diameter of a cylindrical pore is increased, its surface area increases, and more atoms are added to the wall for interaction with the confined molecule. This effect is further enhanced for the spherical nanocavity, which has two radii of curvature. Thus, the geometry-dependent differences shown in Fig. 5.5 account for two effects, the location of minima in the LJ potential and the size and location of the surface surrounding the confined molecule.

The general plots support the constant relationships we found earlier between the pore diameters for maximum q_{st}^{o} and σ_{sf} and can explain the slight variations that occurs for helium because of its small value of ϵ_{sf}/k. After demonstrating the constant relationships using general plots based on the calculated results, we explain the phenomenon by exploring the relationship between the external wall potential and pore diameters in the next section.

External wall potential

The external wall potentials in our research can be treated as a superposition of the LJ potentials between one gas molecule and one carbon atom. Consider a cylindrical carbon nanopore as an example to analyze the relationship between the external wall potential and pore diameters. Our focus in on high isosteric heats of adsorption, which occur when the size of a gas molecule is close to the pore width; e.g., $H_{\mathrm{c}}/\sigma_{\mathrm{sf}}$ is around 2.0–2.3 based on our earlier results. Under these conditions, the center of a gas molecule is very close to the center of the pore. Therefore, it is reasonable to assume the gas molecule to be sitting in the center of the pore to approximate the real situation. Following Everett and Powl,[8] for the LJ potentials, there are three possible cases for the superposition, as shown by the simplified profiles in Fig. 5.6.

When the dimensionless pore diameter is large, the result of addition will generate a total external wall potential with the second derivative $d^2V_{\mathrm{ext}}/d\rho^2$ being negative at the center of the pore, shown as case 1 in Fig. 5.6. As the two walls approach each other, the second derivative $d^2V_{\mathrm{ext}}/d\rho^2$ at the center of the pore will pass through zero, which is shown as case 2 in Fig. 5.6 and is referred to as a inflection point. Finally, when the distance of wall separation continues to decrease, the minimum external wall potential occurs at the center of the pore with a positive $d^2V_{\mathrm{ext}}/d\rho^2$, which is shown as case 3 in Fig. 5.6.

The corresponding dimensionless pore diameters, $H_{\mathrm{c}}/\sigma_{\mathrm{sf}}$, at the inflection points for the three geometrical pores have been calculated and are 2.28, 2.46, and 2.56 for the slit-shaped, cylindrical, and spherical geometries, respectively. These first two values are in good agreement with results of Everett and Powl,[8] who considered LJ potentials in slit-shaped pores and cylindrical pores. When the dimensionless pore diameter is larger than these values, the minimum external wall potential for the gas molecule occurs near the walls as shown in case 1. When the dimensionless pore

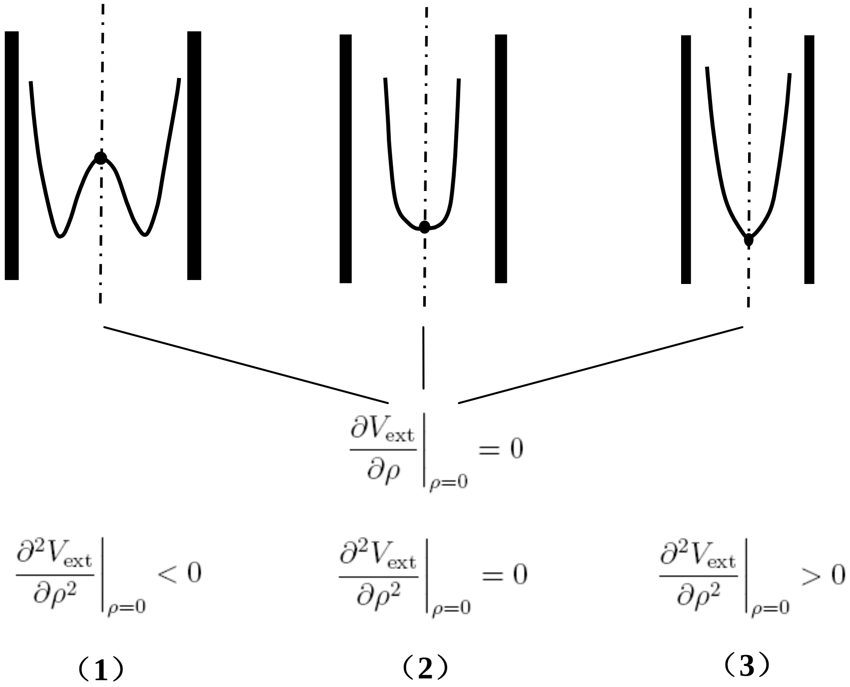

Figure 5.6: Three possible results for the superposition of LJ potentials.

diameter is smaller than the value at the inflection points for the specific geometry, the minimum external wall potential occurs at the center of the pore.

The dimensionless pore diameters corresponding to the maximum $q_{\mathrm{st}}^{\mathrm{o}}$ that we obtained in Table 5.4 are smaller than the dimensionless pore diameters at the inflection points for all of the three geometries. Therefore, the minimum external wall potential occurs at the center of the pores for these conditions, as shown as case 3 in Fig. 5.6. For this case, the isosteric heat of adsorption can be approximated by

$$q_{\mathrm{st}}^{\mathrm{o}} = \frac{1}{2}RT - N_{\mathrm{a}}V_{\mathrm{ext}} \tag{5.12}$$

by using the harmonic oscillator approximation.[1] The maximum $q_{\mathrm{st}}^{\mathrm{o}}$ can now be obtained when the external wall potential is a minimum for this condition. As known from above, the minimum V_{ext} for the conditions in case 3 occurs at the center for any pore with a diameter less than the inflection point value. There is a set of minimum V_{ext} occurring at the center of pores with various diameters. The overall minimum V_{ext} that we need is the smallest V_{ext} for a pore with a certain diameter among the set of minimums.

The cylindrical nanopore is still used as an example here to calculate the external wall potential at the center of pores as a function of the dimensionless pore diameter in order to determine the overall minimum V_{ext}. The results are shown in Fig. 5.7. We found that the overall minimum V_{ext} at the center of the pore occurs when the dimensionless pore diameter is equal to 2.18 for all of the gas molecules considered. This value is consistent with the dimensionless pore diameter that we obtained for the maximum $q_{\mathrm{st}}^{\mathrm{o}}$ for cylindrical nanopores. This can verify that the maximum $q_{\mathrm{st}}^{\mathrm{o}}$ and the overall minimum V_{ext} occur at the same dimensionless pore diameter for the conditions in case 3 and can explain that the constant dimensionless pore diameter found earlier for the maximum $q_{\mathrm{st}}^{\mathrm{o}}$ for cylindrical pores is caused by the relationship between V_{ext} and the pore diameter. This approach can also be applied to explain the dimensionless pore diameters corresponding to the maximum $q_{\mathrm{st}}^{\mathrm{o}}$ for the silt-shaped nanopores and spherical nanocavities.

Geometrical effects

The isosteric heat of adsorption is a strong function of pore width and it also depends on surface geometry. In order to study the geometrical effects, we calculate the $q_{\rm st}^{\rm o}$ as a function of pore width for single wall slit-shaped carbon nanopore, which is different from the multiwall slit-shaped carbon nanopore that was studied by Schindler and LeVan,[6] to compare with the results for cylindrical nanopores and spherical nanocavities. For example, the isosteric heats of adsorption for argon in single wall carbon nanopores with three different geometries, slit-shaped, cylindrical and spherical, have been shown in Fig. 5.8. The maximum $q_{\rm st}^{\rm o}$ for slit-shaped nanopores, cylindrical nanopores and spherical nanocavities are 16.21 kJ/mol, 26.45 kJ/mol and 35.87 kJ/mol, respectively. In addition, the pore widths where the maximum $q_{\rm st}^{\rm o}$ occurs and where $q_{\rm st}^{\rm o} = 0$ occurs are different for different geometries. As shown in Fig. 5.8, the shape of these three curves are similar to each other. For all geometries, $q_{\rm st}^{\rm o}$ first will increase rapidly from negative values to a maximum and then will decrease gradually when the pores reach larger widths. Generally, the spherical carbon nanocavity has the largest $q_{\rm st}^{\rm o}$, and the cylindrical carbon nanopore has the second largest $q_{\rm st}^{\rm o}$.

This phenomenon can be ascribed to the different surface mean curvatures of the three carbon nanopores, as should be expected. The slit-shaped nanopore is modeled with two parallel planes so the surface mean curvature is zero. The surface mean curvature for the internal surface of a cylinder of radius a is $1/(2a)$, and the surface mean curvature for the internal surface of a sphere of radius a is $1/a$.[23] Obviously, the spherical surface has the largest mean curvature among the three geometries given the same pore width.

A larger surface mean curvature denotes a larger number of carbon atoms that

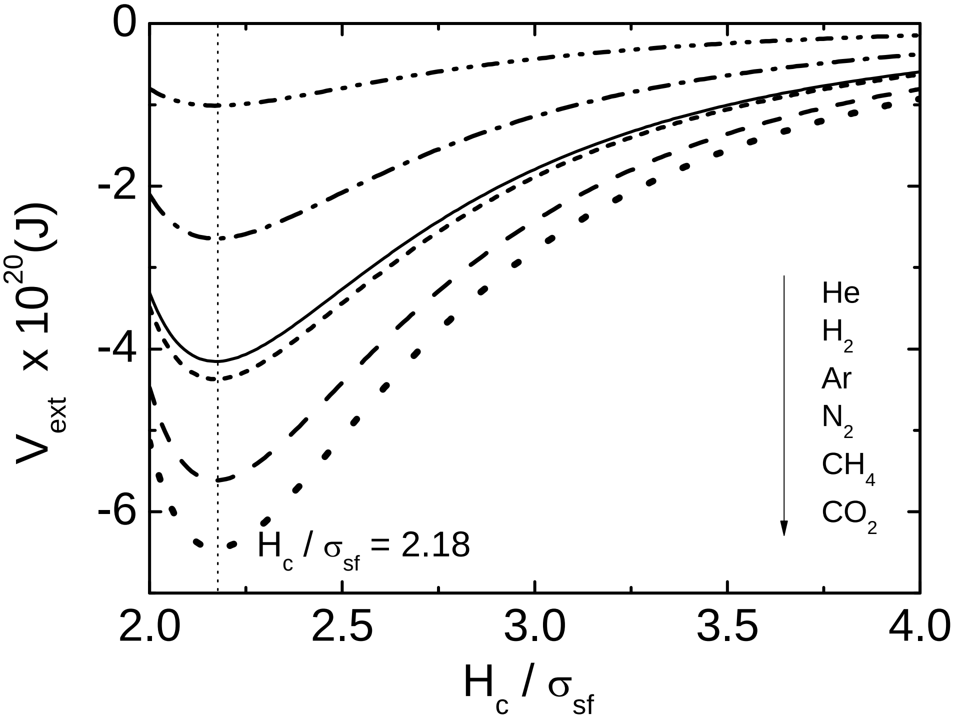

Figure 5.7: External wall potentials at the center of pores as functions of dimensionless pore diameters for all six gas molecules in a cylindrical nanopore.

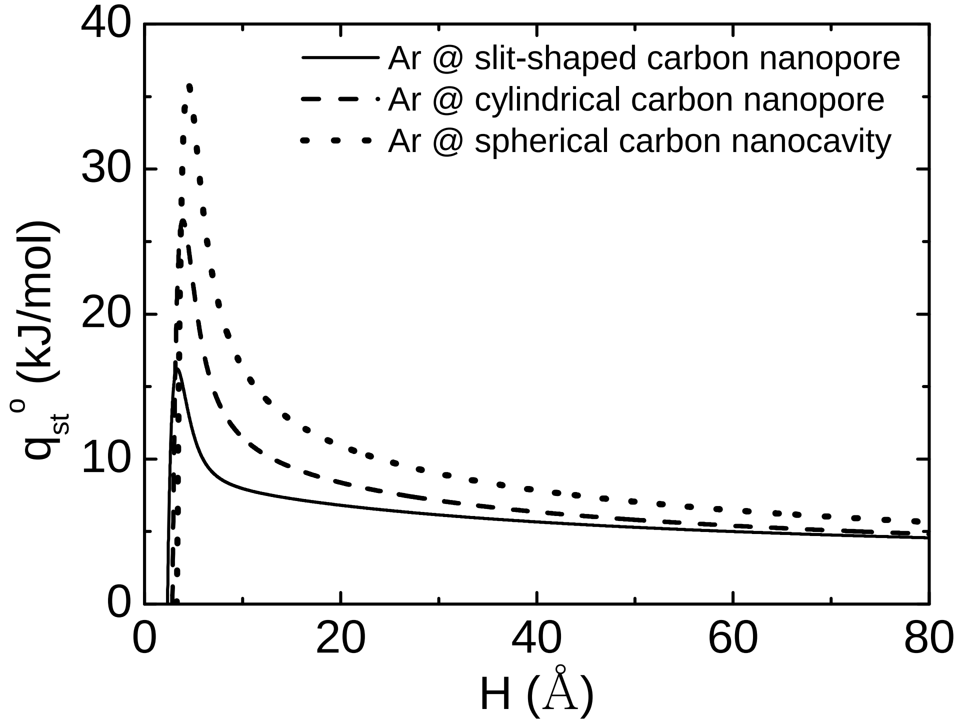

Figure 5.8: Isosteric heats of adsorption of argon in three different geometries.

influence the adsorbate molecule strongly in 3-D space.[24] Therefore, a larger heat of adsorption is expected for the surface that has a larger surface mean curvature. In addition, the surface mean curvatures for cylindrical and spherical surfaces are reciprocal functions of radius. So, they decline rapidly with the increase of pore radius in the narrow pore region and decline slowly in the large pore region. This can explain the shape of the curves in Fig. 5.8. After the pore width passes the point at which $q_{\mathrm{st}}^{\mathrm{o}}$ is zero, the value of $q_{\mathrm{st}}^{\mathrm{o}}$ changes quickly from zero to a maximum and then relative slowly from the maximum to lower values. When the pore width is even larger, the surface mean curvatures of both cylindrical and spherical surface approach zero, giving the surface mean curvature of a plane. Thus, as shown in Fig. 5.8, the isosteric heats of adsorption curves for the three geometries merge together when the pore width is larger than about 8 nm because the pore width is so large that the gas molecule is not influenced sufficiently by the small differences in surface curvatures, and the molecule is essentially interacting with a single layer plane.

5.4 Conclusions

The isosteric heat of adsorption in the Henry's law region has been calculated for six gas molecules: argon, methane, carbon dioxide, hydrogen, helium, and nitrogen in both carbon single wall cylindrical nanopores and spherical nanocavities. The maximum isosteric heats of adsorption have been determined for all of the six gas molecules in both cylindrical and spherical geometries. The maximum isosteric heats of adsorption in cylindrical carbon nanopores have been compared with adsorption data in the literature for a SWNT . Our results agree well with the simulation work under similar conditions. Experiment limitations and broad pore size distributions lead the relatively larger differences between some of our results and the experimental data.

General plots, shown in Fig. 5.5, have been generated to conveniently predict pore diameter for the maximum isosteric heat of adsorption for non-polar or weakly polar molecules adsorbed in carbon nanopores. These show constant relationships for straightforward estimation of pore diameters at which maximum isosteric heats of adsorption occur. We also have proposed an equation to provide an estimation of the isosteric heat of adsorption based on the external wall potential at the center of pores when the dimensionless pore diameter is less than the inflection point value for a specific geometry.

The influence of geometry on the isosteric heat of adsorption has also been investigated. The spherical carbon surface is the most attractive surface for gas molecules in the small pore region because of its large surface mean curvature. The effects of surface curvature disappear gradually as the pore size increases. The information provided in this paper should be beneficial for the design of novel carbon adsorbents for various applications.

References

[1] Steele, W. A. The interaction of gases with solid surfaces. Oxford: Pergamon Press; 1974.

[2] Vernov, A.; Steele, W. A. Computer simulation of benzene adsorbed on graphite. 1. *Langmuir* **1991**, *7*, 3110–3117.

[3] Pikunic, J.; Clinard, C.; Cohaut, N.; Gubbins, K. E.; Guet, J.; Pellenq, J. M. Structure modeling of porous carbons: constrained reverse Monte Carlo method. *Langmuir* **2003**, *19*, 8565–8582.

[4] Do, D. D.; Do, H.D.; Wongkblap, A.; Nicholson, D. Henry constant and isosteric heat at zero-loading for gas adsorption in carbon nanotubes. *Phys. Chem. Chem. Phys.* **2008**, *10*, 7293–7303.

[5] Floess, J. K.; Vanlishout, Y. Calculation of adsorption energies in carbon micropores. *Carbon* **1992**, *30*, 967–973.

[6] Schindler, B. J.; LeVan, M. D. The Theoretical Maximum Isosteric Heat of Adsorption in The Henry's Law Region for Slit-Shaped Carbon Nanopores. *Carbon* **2008**, *46*, 644–648.

[7] Derrah, R.I.; Ruthven, D. M. Sorption of the inert gases (Ar, Kr, and Xe) in type A zeolites. *Can. J. Chem.* **1975**, *53*, 996–1006.

[8] Everett, D. H.; Powl, J. C. Adsorption in slit-like and cylindrical micropores in the henry's law region. *J. Chem. Soc. Faraday. Trans. I* **1976**, *72*, 619–636.

[9] Fujiwara, A.; Ishii, K.; Suematsu, H.; Kataura, H.; Maniwa, Y.; Suzuki, S. Gas adsorption in the inside and outside of single-walled carbon nanotubes. *Chem. Phys. Lett.* **2001**, *336*, 205–211.

[10] Do, D. D.; Nicholson, D.; Do, H. D. On the Henry constant and isosteric heat at zero loading in gas phase adsorption. *J. Colloid Interface Sci.* **2008**,*324*, 15–24.

[11] Tjatjopoulos, G. J.; Feke, D. L.; Adin Mann, Jr. J. Molecule-micropore interaction potentials. *J. Phys. Chem.* **1988**, *92*, 4006–4007.

[12] Ryshik, I. M.; Gradstein, I. S. *Table of Integrals, Series, and Products*; Academic Press: New York, 1980.

[13] Wilder, J. W. G.; Venema, L. C.; Rinzler, A. G.; Smally, R. E.; Dekker, C. Electronic structure of atomically resolved carbon nanotubes. *Nature* **1998**, *391*, 59–62.

[14] Baksh, M. S. A.; Yang, R. T. Model for spherical nanocavity radii and potential functions of sorbated in zeolites. *AlChE J.* **1991**, *37*, 923–30.

[15] Ravikovitch, P. I.; Nishnyakov, A.; Russo, R.; Neimark, A. V. Unified approach to pore size characterization of microporous carbonaceous materials for N_2, Ar, and CO_2, adsorption isotherms. *Langmuir* **2000**, *16*, 2311–2320.

[16] Ravikovitch, P. I.; Nishnyakov, A.; Neimark, A. V. Density functional theories and molecular simulations of adsorption and phase transitions in nanopores. *Phys. Rev. E* **2001**, **64**, 011602-1–011602-20.

[17] Poling, B. E.; Prausnitz, J. M.; O'Connell, J. P. The properties of gases and liquids. New York: McGraw-Hill; 2001.

[18] Jiang, J. W.; Sandler, S. I. Nitrogen adsorption on carbon nanotube bundles: Role of the external surface. *Phys. Rev. B* **2003**, *68*, 245412-1–245412-9.

[19] Talapatra, S.; Migone, A. D. Adsorption of methane on bundles of closed-ended single-wall carbon nanotubes. *Phys. Rev. B* **2002**, *65*, 045416-1–045416-6.

[20] Bienfait, M.; Zeppenfeld, P.; Dupont-Pavlovsky, N.; Muris, M.; Johnson, M. R.; Wilson, T. Thermodynamics and structure of hydrogen, methane, argon oxygen, and carbon dioxide adsorbed on single-wall carbon nanotube bundles. *Phys. Rev. B* **2004**, *70*, 035410-1–035410-10.

[21] Wilson, T.; Vilches, O. E. Helium adsorbed on carbon nanotube bundles: one-dimensional and/or two-dimensional solid? *Low Temp. Phys.* **2003**, *29*, 732–735

[22] Yoo, D. H.; Rue, G. H.; Hwang, Y. H.; Kim, H. K. Study of nitrogen adsorbed on single-walled carbon nanotube bundles. *J. Phys. Chem. B* **2002**, *106*, 3371–3374.

[23] O'Neil, B. Elementary differential geometry. Boston: Elsevier Academic Press; 2006.

[24] Jiang, J. W.; Wagner, N. J.; Sandler, S. I. A Monte Carlo Simulation Study of The Effect of Carbon Topology on Nitrogen Adsorption on Graphite, A Nanotube Bundle, C_{60} Fullerite, C_{168} Schwarzite, and A Nanoporous Carbon. *Phys. Chem. Chem. Phys.* **2004**, *6*, 4440–4444.

CHAPTER VI

HENRY'S LAW CONSTANTS AND ISOSTERIC HEATS OF ADSORP TION AT ZERO LOADING FOR MULTI-WALL CARBON SURFACES WITH DIFFERENT GEOMETRIES

6.1 Introduction

Henry's law in gas adsorption describes the affinity between an adsorbate molecule and the adsorbent. Therefore, it is of importance to determine this relationship and the associated isosteric heat of adsorption at zero loading. Classical statistical thermodynamics shows that Henry's law behavior invariably exists at zero loading. The Henry's law constant and the isosteric heat of adsorption at zero loading can always be calculated given models for solids and intermolecular interactions between fluid molecules and solids.[1]

Considerable research has been done on Henry's law constants and isosteric heats of adsorption for gas adsorption on well-defined solid surfaces, particularly graphite, activated carbon, and carbon nanotubes, using the statistical thermodynamic method originally developed by Steele.[2–5] In addition, Jiang *et al.*[6] calculated Henry's law constants for many single wall carbon surfaces with different topologies using Monte Carlo simulation. Do *et al.*[7] used the Grand Canonical Monte Carlo (GCMC) method to calculate the Henry's law constant and isosteric heat of adsorption at zero loading for argon adsorption on carbon nanotubes. They focused on the difference in the Henry's law constant and isosteric heat of adsorption between the inside and outside surfaces of carbon nanotubes. In another paper, Do *et al.*[8] considered the temperature dependence of both the Henry's law constant and the isosteric heat of adsorption.

This is the final in a series of three papers in which we investigate heats of adsorption in the Henry's law limit for several common light gases adsorbed on carbon surfaces of various geometries. In our first paper,[5] we calculated the isosteric heat of adsorption as a function of the pore width for six light gas molecules adsorbed in single wall slit-shaped carbon nanopores. The pore widths where maximum heats of adsorption occur were determined and found to be sensitive to the Lennard-Jones (LJ) potential collision diameter but only weakly dependent on the LJ well depth potential. A general plot was prepared for predicting the pore widths where maximum heats of adsorption occur for non-polar and weakly polar gas molecules adsorbed in slit-shaped carbon nanopores.

In our second paper,[9] we went beyond the slit-shaped geometry of the first paper to consider cylindrical and spherical geometries for a single wall carbon surface. The surface mean curvature was shown to be essential in determining the heat of adsorption for carbon nanopores with different geometries for small pore widths. Empirical linear relationships were found between the pore diameters corresponding to the maximum heats of adsorption and the solid-fluid LJ collision diameters for all three geometries. A general plot was presented for the prediction of pore widths where the maximum heats of adsorption occur for non-polar or weakly polar LJ gas molecules adsorbed in single wall carbon nanopores with various geometries.

Besides single wall carbon surfaces, it is also important to consider the Henry's law constant and the associated isosteric heat of adsorption at zero loading for multi-wall carbon surfaces since many carbon adsorbents are better described by a multi-wall model. In this paper, the Henry's law constant and isosteric heat of adsorption at zero loading will be investigated for several gases adsorbed on multi-wall carbon surfaces with slit-shaped, cylindrical, and spherical geometries. The dependence of Henry's law constants and isosteric heats of adsorption on pore width, surface mean curvature, and number of layers of wall in these well-defined geometries will be examined. Calculated results for isosteric heats and Henry's law constants will be compared with literature values. For slit-shaped carbon nanopores, we will also compare our results with those obtained using Steele's 10-4-3 potential. In an appendix, we develop simple relationships for single wall surfaces to permit Henry's law constants to be converted between bases of absolute volume and accessible volume of the adsorbent.

Collectively, our three papers provide a systematic study of some fundamental thermodynamic properties for light gas molecules adsorbed on surfaces with various geometries and walls with different numbers of carbon layers for the Henry's law region. The general plots in our papers are useful for predicting the pore widths where maximum heats of adsorption occur for LJ molecules adsorbed in carbon adsorbents. Heats of adsorption and Henry's law constants are quantitatively related with pore width, surface mean curvature, and number of wall layers to provide beneficial information for the design and synthesis of novel carbon adsorbents for various applications.

6.2 Theory

Some macroscopic characteristics for gas adsorption in the Henry's law region are that the gas concentration is infinitesimal and the isotherm within this region is linear. Microscopically, for gas adsorption in the Henry's law region, each gas molecule can independently explore every adsorption site on the whole surface of the adsorbent, and the surface can be homogeneous or heterogeneous. In the dilute limit of Henry's law, adsorbate-adsorbate interactions do not exist and only the solid-fluid interaction potential energies are considered.

The slit-shaped, cylindrical, and spherical single wall carbon surface model potentials and parameters are taken from the literature.[5,9–11] These models can be viewed as ideal models for graphite, carbon nanotubes, and fullerene with open access. All gas molecules are described by a single site model. The carbon atoms are assumed to be uniformly distributed over the wall with specific surface number densities. The LJ potential is commonly used to describe the site-to-site interactions between non-polar or weakly polar gas molecules and carbon surfaces.[10,12] Averaged external wall potentials are obtained by integrating the site-to-site LJ potential over the inner space of the pores to account for all possible molecule locations for slit-shaped, cylindrical, and spherical geometries.[9–11] For all of the geometries, H_{c} is the distance between the centers of the carbon atoms on opposing walls of the pore, which will be referred to below as pore diameter. $H = H_{\mathrm{c}} - \sigma_{\mathrm{ss}}$ is the distance between the surfaces of carbon atoms on opposing walls (i.e., the inside diameter), which will be referred to below as pore width. σ_{ss} is the LJ collision diameter for a carbon atom. For the parallel-sided slit-shaped pore, the external wall potential is given by[9,10,13]

$$\begin{aligned} V_{\mathrm{ext,\ slit}} = {} & 8\pi n_{\mathrm{s}} \epsilon_{\mathrm{sf}} \sigma_{\mathrm{sf}}^2 \left\{ \frac{1}{10} \left(\frac{\sigma_{\mathrm{sf}}}{R} \right)^{10} \left[\left(1 - \frac{\rho}{R} \right)^{-10} + \left(1 + \frac{\rho}{R} \right)^{-10} \right] \right. \\ & \left. - \frac{1}{4} \left(\frac{\sigma_{\mathrm{sf}}}{R} \right)^{4} \left[\left(1 - \frac{\rho}{R} \right)^{-4} + \left(1 + \frac{\rho}{R} \right)^{-4} \right] \right\} \end{aligned} \tag{6.1}$$

where n_{s} is the carbon number density (atoms per unit area), ϵ_{sf} and σ_{sf} are the solid-fluid well depth potential and the solid-fluid collision diameter, R is half of the pore diameter of the slit-shaped nanopore, and ρ is the perpendicular distance between the center of a fluid molecule and the center axis of the slit-shaped pore. Similarly, for cylindrical geometry, we have[7,10]

$$\begin{aligned} V_{\mathrm{ext,\ cyl}} = {} & n_{\mathrm{s}} \pi^2 \epsilon_{\mathrm{sf}} \sigma_{\mathrm{sf}}^2 \left\{ \frac{63}{32} \left[\frac{R-\rho}{\sigma_{\mathrm{sf}}} \left(1 + \frac{\rho}{R} \right) \right]^{-10} \times F \left[-\frac{9}{2}, -\frac{9}{2}; 1; \left(\frac{\rho}{R} \right)^2 \right] \right. \\ & \left. - 3 \left[\frac{R-\rho}{\sigma_{\mathrm{sf}}} \left(1 + \frac{\rho}{R} \right) \right]^{-4} \times F \left[-\frac{3}{2}, -\frac{3}{2}; 1; \left(\frac{\rho}{R} \right)^2 \right] \right\} \end{aligned} \tag{6.2}$$

where R is half of the pore diameter of the cylindrical nanopore, ρ is the perpendicular distance between the center of a fluid molecule and the center axis of the cylinder, and $F[\alpha, \beta; \gamma; z]$ denotes the hypergeometric series with parameters α, β, and γ.[14] Finally, for a spherical surface, the external wall potential is[11]

$$V_{\text{ext, sph}} = 8\pi R^2 n_{\text{s}} \epsilon_{\text{sf}} \left[-\left(\frac{\sigma_{\text{sf}}}{R}\right)^6 \frac{1}{4\left(\rho/R\right)} \left(\frac{1}{\left(1-\rho/R\right)^4} - \frac{1}{\left(1+\rho/R\right)^4}\right) + \left(\frac{\sigma_{\text{sf}}}{R}\right)^{12} \frac{1}{10\left(\rho/R\right)} \left(\frac{1}{\left(1-\rho/R\right)^{10}} - \frac{1}{\left(1+\rho/R\right)^{10}}\right)\right] \tag{6.3}$$

where R is half of the pore diameter of the spherical nanocavity, and ρ is the distance between the center of a fluid molecule and the center of the cavity. Adsorption occurs only on the internal surface in our study, and a small opening is assumed to exist into the nanocavity. This small opening allows gas molecules to pass through the cavity wall while having little effect to the solid-fluid potential. For large pores, irrespective of their geometry, and a molecule close to a wall, all three potentials approach the same limit, which is

$$V_{\text{ext}} = -\frac{2\pi n_{\text{s}} \epsilon_{\text{sf}} \sigma_{\text{sf}}^6}{(1-\rho/R)^4 R^4} \left[1 - \frac{2}{5}\left(\frac{\sigma_{\text{sf}}/R}{1-\rho/R}\right)^6\right] \tag{6.4}$$

Equations 6.1 to 6.3 are external wall potentials for single wall carbon nanopores with different geometries. To obtain the external wall potentials for multi-wall carbon surfaces, following Steele[15,16] and others,[7,17–19] we sum the single wall potentials layer by layer. For example, when we consider the external wall potential for the second layer of a two-layer carbon surface, a separation distance of 3.35 Å[5] between the layers is added to the distance between the center of the gas molecule and the center of a carbon atom in the first layer wall to give the new interaction distance between the gas molecule and a carbon atom in the second layer wall. Then, we can obtain the total external wall potential for a two-layer carbon surface by summing the external wall potentials for the first and second layers. Finally, limiting values for the infinite layer wall are obtained when the inclusion of additional layers has no significant change on results. Thus, the solid-fluid potential will depend on both curvature effects as given by the geometry (i.e., equations 6.1–6.3) and by the number of layers included in the summation for the wall.

As in our previous paper,[9] Steele's method is adopted to calculate the isosteric heat of adsorption for all geometries using

$$q_{\mathrm{st}}^{\mathrm{o}} = RT - N_{\mathrm{a}} \frac{\int_{\mathrm{V}^{(\mathrm{s})}} V_{\mathrm{ext}}(\mathbf{r}_i) \exp[-V_{\mathrm{ext}}(\mathbf{r}_i)/kT] \; d\mathbf{r}_i}{\int_{\mathrm{V}^{(\mathrm{s})}} \exp[-V_{\mathrm{ext}}(\mathbf{r}_i)/kT] \; d\mathbf{r}_i} \tag{6.5}$$

where R is the gas constant, T is absolute temperature, N_{a} is Avagadro's number, $V^{(\mathrm{s})}$ is the volume of the adsorbed phase, $\mathbf{r}_i$ is the position vector, and k is the Boltzman constant. Also, we calculate the Henry's law constant in units of mol/(m^2 Pa) using[15,20]

$$K_{\mathrm{H}} = \frac{1}{ART} \int_{\mathrm{V}^{(\mathrm{s})}} \{\exp[-V_{\mathrm{ext}}(\mathbf{r}_i)/kT] - 1\} \; d\mathbf{r}_i \tag{6.6}$$

where A is the internal surface area of the pore. The pore volume basis of equation 6.6 is considered further in the appendix.

6.3 Results and Discussion

Pore width and curvature dependence of Henry's law constant

We have calculated the Henry's law constants for all the six gas molecules in different geometries using equation 6.6. The integrations in this paper were performed using an extended trapezoidal rule. The results for argon adsorbed in single wall carbon cylindrical nanopores at different temperatures are shown in Fig. 6.1 for temperatures from 70 K to 800 K. It is clear that the Henry's law constants have single maxima for all the pore widths at any fixed temperature. The shapes of the curves are similar to what we reported for heats of adsorption in a previous paper,[9] which means that the changes of isosteric heats of adsorption and Henry's law constants have similar trends relative to the change of pore width since both are signs of adsorption affinity.

From Fig. 6.1, it is also obvious that the Henry's law constants decrease with an increase in temperature. In order to better understand the temperature dependence

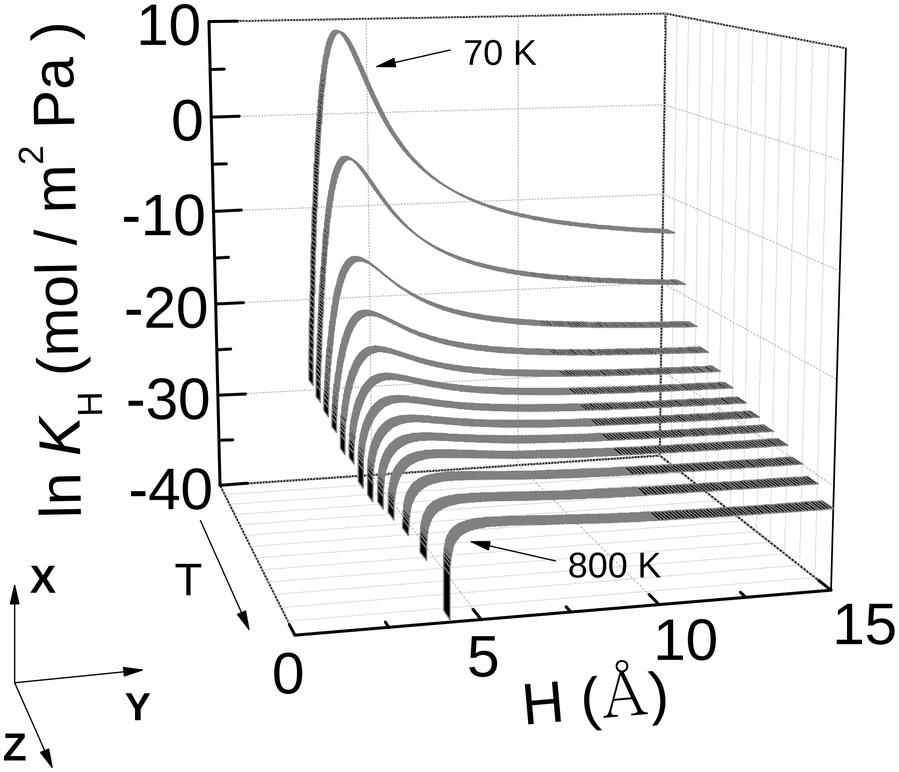

Figure 6.1: Henry's law constant as a function of pore width for Ar adsorbed in single wall cylindrical carbon nanopores at different temperatures. T = 70, 100, 150, 200, 250, 300, 350, 400, 450, 500, 600, 700, 800 K, increasing in the positive z direction.

of Henry's law constants, we developed the Van't Hoff plots (ln K_H vs. T^{-1}) shown in Fig. 6.2 for argon adsorbed in single wall cylindrical carbon nanopores with different pore widths and in Fig. 6.3 for nitrogen adsorbed in a 5.0 Å multi-wall cylindrical carbon nanopores. The Van't Hoff plots are non-linear in T^{-1} based on equation 6.6, and some non-linear Van't Hoff plots have been shown in the recent publications.[7,8] As shown in Fig. 6.2 and Fig. 6.3, the non-linearity of the Van't Hoff plots becomes more apparent at high temperatures and with weak adsorption potentials.

The Henry's law constants for argon adsorbed at 298.15 K on single wall carbon surfaces with different geometries are shown in Fig. 6.4. The maximum Henry's law constant for the carbon surfaces with three geometries decreases from the spherical nanocavity through the cylindrical nanopore to the slit-shaped nanopore in the order of decreasing surface mean curvature.[9] The significant differences in the Henry's law constants between the three geometries, especially in the small pore width region, suggest that surface curvature is as important as pore width for gas adsorption on carbon surfaces. SWCNTs, a well characterized material with cylindrical carbon nanopores, has been widely considered to have higher affinities toward gas molecules, such as hydrogen and methane, than activated carbon or microporous carbon.[21,22] This clearly shows the superiority of higher surface curvature, which leads to stronger confinement with one adsorbate molecule interacting with many adsorbent atoms, in determining the affinity of gas adsorption. Furthermore, we may anticipate that some new carbon materials with even more curved nanopore surfaces will have higher affinities toward gas molecules than SWCNTs.

The Henry's law constants for other gases adsorbed on carbon surfaces with different geometries have also been calculated. A comparison between results in this work and results in the literature for the Henry's law constants for different carbon surfaces is shown in Table 6.1. For this comparison, graphite was treated as a material of infinite extent with slit-shaped nanopores and a large pore width; we used 100 Å,

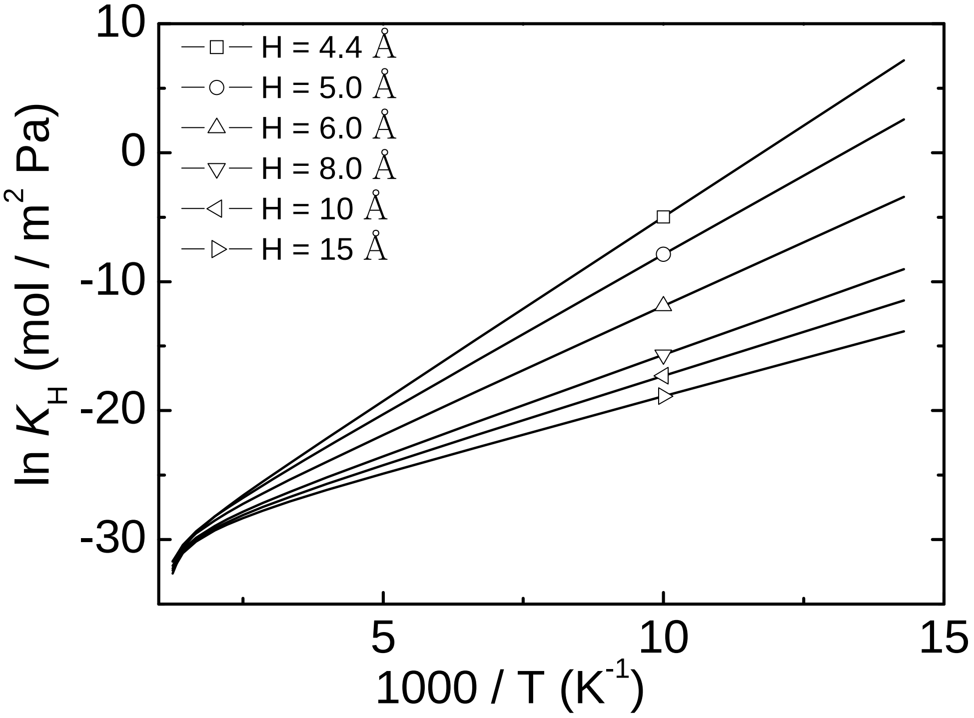

Figure 6.2: Van't Hoff plots for Ar adsorbed in single wall cylindrical carbon nanopores with different pore widths.

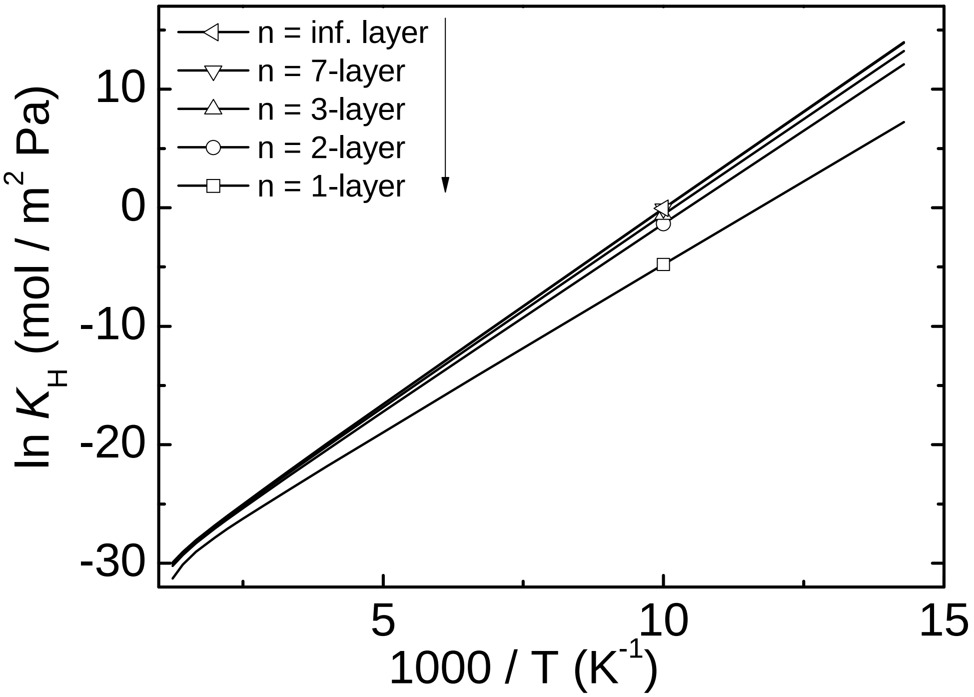

Figure 6.3: Van't Hoff plots for N_2 adsorbed in 5.0 Å multi-wall cylindrical carbon nanopores with different layers of walls.

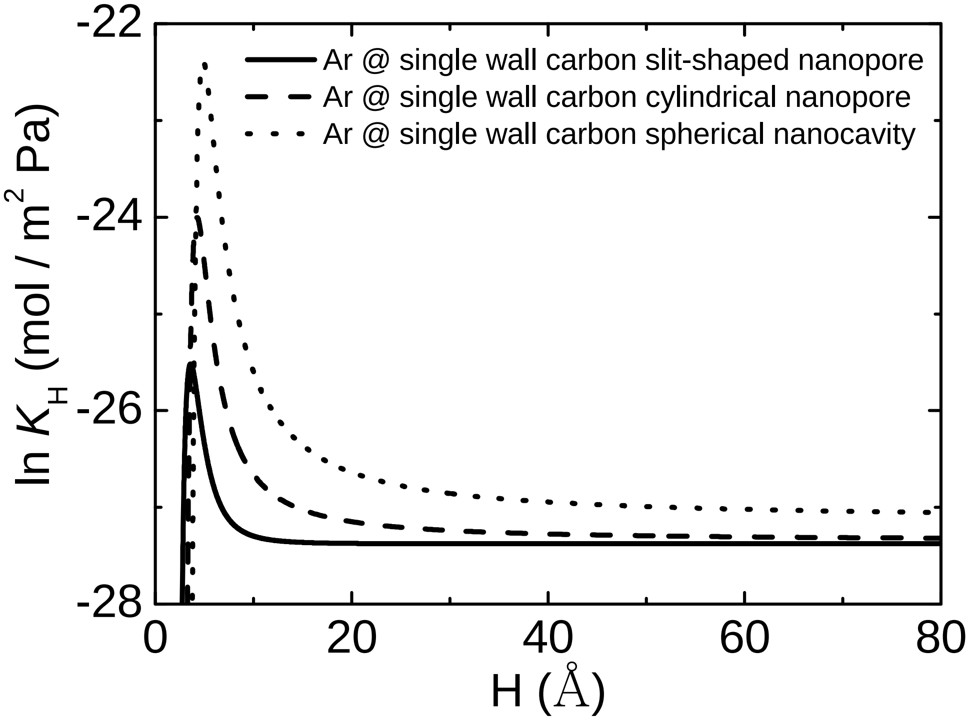

Figure 6.4: Henry's law constants for Ar adsorbed on single wall carbon surfaces with different geometries at 298.15 K.

Table 6.1: Henry's law constants for single wall and multi-wall carbon surfaces.

Molecule	Adsorbent	Corresponding model	Pore width H (Å)	T (K)	Unit of K_H	ln K_H (this work)	ln K_H (literature)	Ref.
N_2	Graphite	Inf. layer slit	100	300	mol/(m^2 Pa)	-26.68	-26.43(E)⋆	Ref[20]
	Graphite	Inf. layer slit	100	200	mol/(m^3 Pa)	-3.96	-4.10(S)	Ref[6]
	SWCNTs bundle	1-layer cylinder	13.56	200	mol/(m^3 Pa)	-1.75	-2.07(S)	Ref[6]
Ar	Graphite	Inf. layer slit	100	300	mol/(m^2 Pa)	-26.93	-27.14(E)	Ref[20]
	SWCNTs	1-layer cylinder	7.47	250	nm	3.41	4.60(S)	Ref[7]
CH_4	Graphite	Inf. layer slit	100	300	mol/(m^2 Pa)	-25.36	-25.70(E)	Ref[20]
	Graphite	Inf. layer slit	100	200	nm	3.12	2.89(S)	Ref[8]

⋆ (S) simulation data; (E) experimental data with further increases having no effect. We show Henry's law constants calculated to have the same units as those in the literature. Some of our results match well with the literature values, such as nitrogen adsorbed on graphite surfaces. In our study, we only consider adsorption that occurs inside an isolated SWCNT. We find a difference between our calculated Henry's law constant and the literature value for nitrogen adsorbed in SWCNTs bundles. For the Henry's law constants in nm,[7,8] the authors used accessible void volume, which avoided negative Henry's law constants at high temperatures. In this paper, we have used an absolute void volume, as is common,[6,15,20] to calculate the Henry's law constant. The comparison shows that using our method gives good agreement with both experimental and simulation results for most cases of normal gas adsorption on carbon surfaces with different geometries and pore widths at low to moderate temperatures. In addition, a method is presented in the appendix to help avoid the negative Henry's law constant occurring at high temperatures without losing consistency with the current results at low to moderate temperatures by replacing the absolute void volume with an accessible void volume.

Isosteric heats of adsorption for multi-wall carbon surfaces

The results for the isosteric heat of adsorption as a function of pore width for argon adsorbed on multi-wall carbon surfaces at room temperature are summarized in Fig. 6.5 to Fig. 6.7 for slit-shaped, cylindrical, and spherical geometries. For the slit-shaped carbon nanopores, we compare the results between single wall carbon nanopore and multi-wall carbon nanopores. The results obtained by using Steele's 10-4-3 potential are also included for comparison.[5,15] The shapes of the curves in Fig. 6.5 are similar; however, as shown in the inserted figure, the difference in the isosteric heats of adsorption for different layers varies. The contributions to the total maximum isosteric heats of adsorption from the different layers of the wall are summarized in Fig. 6.8. The contributions to the total maximum heats of adsorption from the first layers always dominates for all three geometries. The contributions to the total maximum heat of adsorption from the same layer with different geometries varies slightly. For example, the contribution to the total maximum heat of adsorption from the second layer of the slit-shaped carbon surface is 8.4%, while the contribution from the second layer of the cylindrical carbon surface is 10.2%, and the contribution from the second layer of the spherical carbon surface is 11.1%. From Fig. 6.8a, it is clear that 97.3% of the total maximum heat of adsorption is due to the first and second layers for multi-wall carbon slit-shaped surface, while 99.9% of the total maximum heat of adsorption occurs by the seventh layer. After the seventh layer, the contributions from additional layers to the total maximum heat of adsorption are very small. These findings are consistent with the trends found by Fischer *et al.*[17] and Do *et al.*[7]

We also notice that for the multi-wall carbon slit-shaped surface, the total maximum heat of adsorption obtained by using Steele's 10-4-3 potential is about 99.7% of the result for infinite layers. Steele derived the 10-4-3 potential for gas adsorption on graphite because integrating the LJ potential over just a few layers of carbon atom sheets did not give good results. The 10-4-3 potential was developed by combining the first terms of the infinite sum of LJ potentials over wall layers with a fitting term that gives a good approximation for the total summation of the LJ potentials. In our work, we did not truncate terms and the summation was continued until no significant difference could be found between consecutive layers. In other words, our results for slit-shaped carbon surface with infinite layers of walls are closer to the exact results than those obtained by using Steele's 10-4-3 potential. Our calculation results verify his choice and show the accuracy of the 10-4-3 potential.

The results for argon adsorbed in multi-wall cylindrical carbon nanopores and spherical nanocavities are similar to the slit-shaped nanopores except the isosteric heats of adsorption are higher, which is caused by the larger surface mean curvatures of cylinders and spheres.[9] From Fig. 6.8b for the cylindrical geometry, 96.5% of the total maximum heat of adsorption is due to the first and second layers while 99.9% of the total maximum heat of adsorption has occurred by the seventh layer, which is the same as found for the carbon slit-shaped surface. From Fig. 6.8c for the spherical geometry, 95.7% of the total maximum heat of adsorption is due to the first and second layers, and 99.8% of the total maximum heat of adsorption has occurred by the seventh layer.

Importantly, the pore widths corresponding to the maximum heats of adsorption are essentially the same for carbon walls with different numbers of layers but the same geometries. For example, only a 0.01 Å difference is found between the the locations of the maxima for the single wall cylindrical carbon nanopores and the infinite layer multi-wall cylindrical carbon nanopores. Therefore, the generally plots we presented in previous papers[5,9] for the prediction of pore width where maximum heats of adsorption occur for single wall carbon surfaces are also applicable for multi-wall carbon surfaces. In addition, for multilayer large pores with all the three geometries, the external wall potentials approach to the same asymptote as shown in equation 6.4.

Adsorption of other gases such as nitrogen, carbon dioxide, methane, hydrogen, and helium in multi-wall carbon surfaces for all the three geometries show trends in heat of adsorption similar to argon. Some of our results are compared with those of microporous carbon and multi-wall carbon nanotubes (MWCNTs) from the literature in Table 6.2. For the multi-wall carbon slit-shaped nanopore model, our results agree very well with literature values for hydrogen and reasonable well for nitrogen. For the multi-wall carbon cylindrical nanopore model, our results do not match most of the experimental results in the literature for carbon nanotubes. One possible reason may be that the experimental isosteric heats of adsorption obtained in the literature are not in the Henry's law region, for which the heat of adsorption is usually larger than for other regions. Secondly, some experimental samples used in the literature would contain impurities which can affect the heat of adsorption.[26] Thirdly, we consider the heat of adsorption on the inside wall of an isolated MWCNTs. We note that in some studies carbon nanotube bundles have been considered. Narrow gaps between carbon nanotubes can lead to higher heats of adsorption while the outside walls of carbon nanotubes lead to lower heats of adsorption than those for adsorption on the inside walls.[7] Our results agree reasonably well with some simulations in the literature for argon adsorption on double-wall carbon nanotubes (DWCNTs). It is worth mentioning that we used a simpler model here than the GCMC model used in some studies in the literature, and we achieve similar results.

As is already known, the MWCNTs have stronger external wall potentials than SWCNTs because of the superposition of potentials. Naturally, the isosteric heats of adsorption we obtained for MWCNTs are higher than SWCNTs at the same pore width. However, most of the isosteric heats of adsorption reported in the literature for MWCNTs are smaller than those of SWCNTs. That is because the MWCNTs usually have large inner pore widths from 10 to 500 Å,[27] while SWCNTs often have much smaller pore widths. SWCNTs with a 3 Å inner pore width have been successfully synthesized.[28] The isosteric heat of adsorption is a very strong function of the pore width, so this can explain why MWCNTs of significantly larger pore width have lower isosteric heats of adsorption while having stronger external wall potentials. However, since MWCNTs have stronger external wall potentials than SWCNTs at the same pore width, MWCNTs with comparable pore widths and the same inside wall surface area as SWCNTs would provide stronger adsorption sites than SWCNTs. Some DWCNTs with a 4 Å inner pore width have recently been synthesized by using SWCNTs as growth templates,[29] which suggests the possibility of creating MWCNTs with comparable pore widths to SWCNTs.

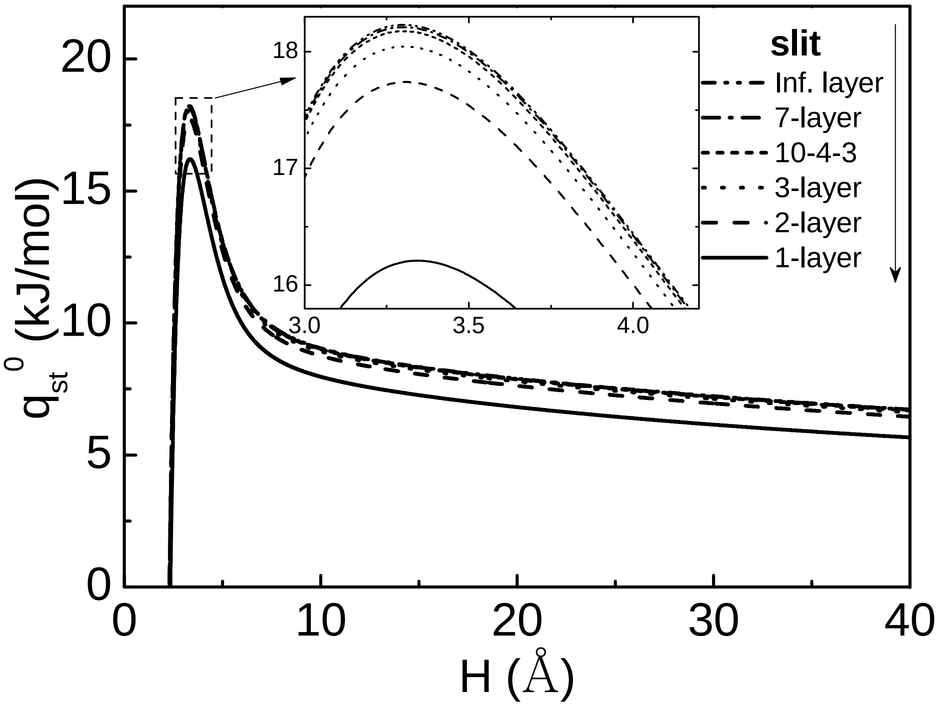

Figure 6.5: Isosteric heats of adsorption as a function of pore width for Ar adsorbed in multi-wall slit-shaped carbon nanopores at room temperature. Results obtained by using Steele's 10-4-3 potential are included for comparison. The inserted figure is a magnified image. The curves are labeled from top to bottom.

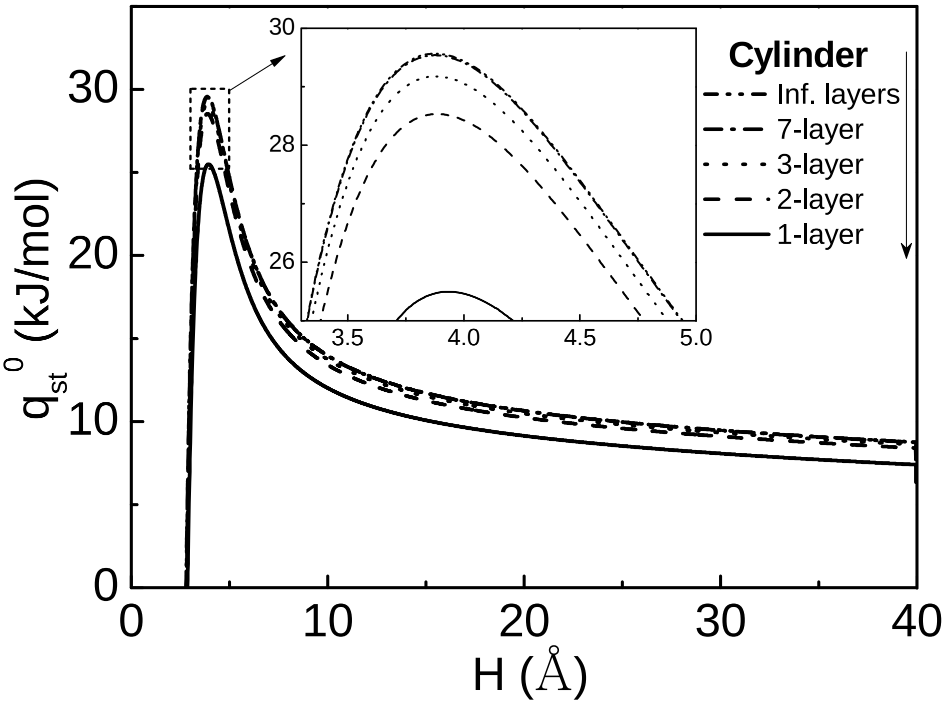

Figure 6.6: Isosteric heats of adsorption as a function of pore width for Ar adsorbed in multi-wall cylindrical carbon nanopores at room temperature. The inserted figure is a magnified image. The curves are labeled from top to bottom.

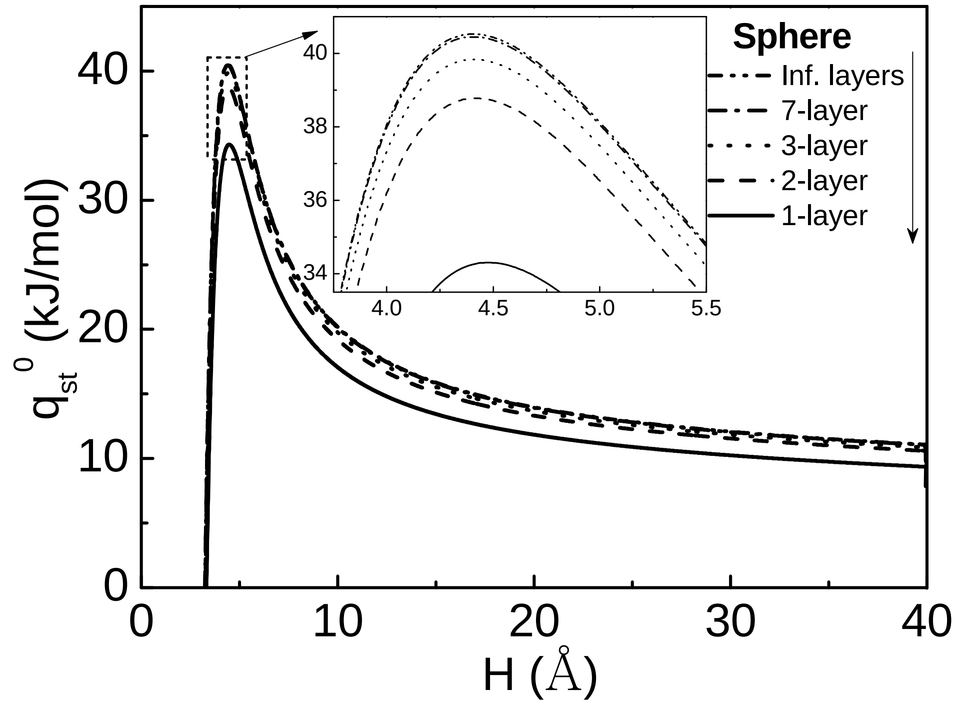

Figure 6.7: Isosteric heats of adsorption as a function of pore width for Ar adsorbed in multi-wall spherical carbon nanopores at room temperature. The inserted figure is a magnified image. The curves are labeled from top to bottom.

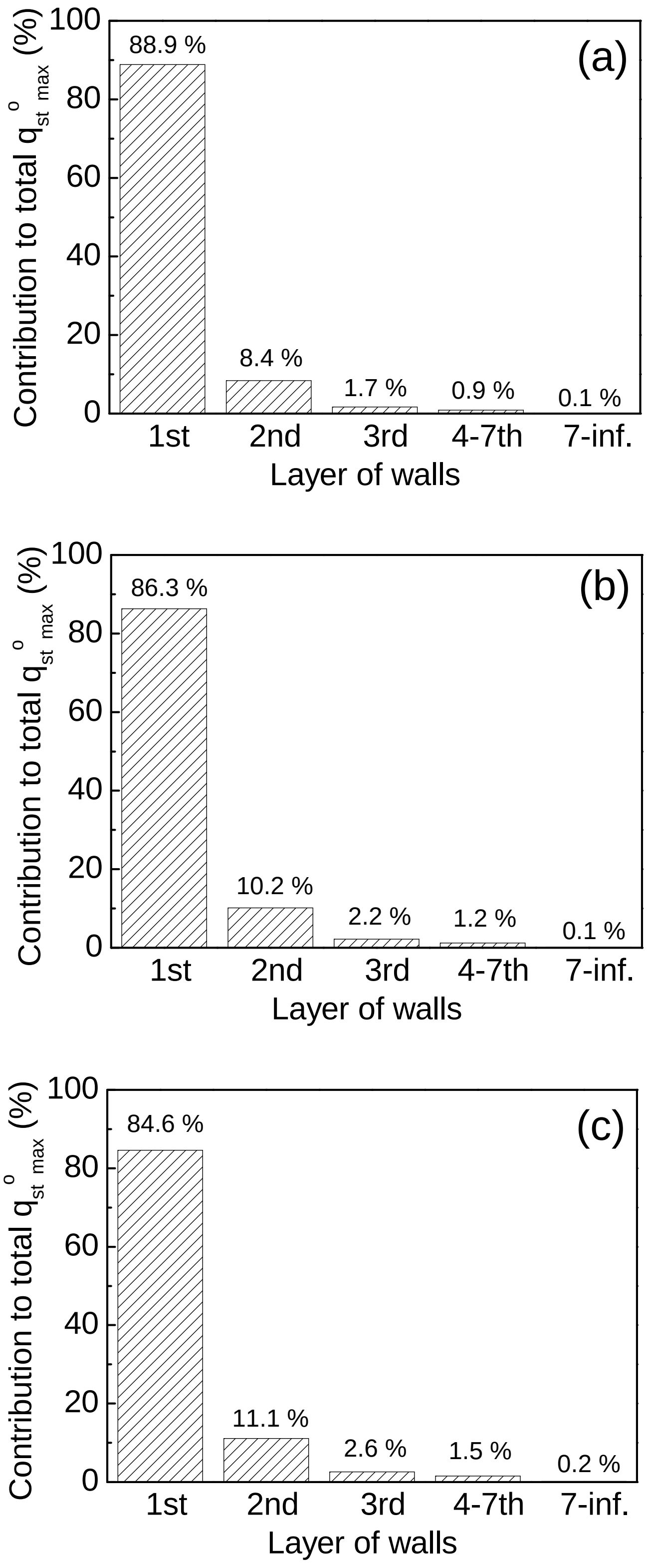

Figure 6.8: The contributions to the total maximum isosteric heats of adsorption from different layer of walls for Ar adsorbed on multi-wall carbon surfaces. (a) slit-shaped geometry; (b) cylindrical geometry; (c) spherical geometry.

Table 6.2: Isosteric heats of adsorption at zero loading for multi-wall carbon surfaces.

Molecule	Adsorbent	Corresponding model	Pore width H (Å)	T (K)	q^o_{st}(this work) (kJ/mol)	q^o_{st}(literature) (kJ/mol)	Ref.
H_2	Microporous carbon	Inf. layer slit	4.3	87	7.61	7.50(E)⋆	Ref[23]
	Activated carbon	Inf. layer slit	21.7	303	4.73	4.80(E)	Ref[25]
	MWCNTs	Inf. layer cylinder	10	233	8.43	1.73(E)	Ref[24]
	MWCNTs*	Inf. layer cylinder	11.8	303	8.08	2.89(E)	Ref[26]
N_2	Activated carbon	Inf. layer slit	21.7	303	8.41	11.6(E)	Ref[25]
Ar	MWCNTs*	Inf. layer cylinder	11.8	303	12.92	3.01(E)	Ref[26]
	DWCNTs	2-layer cylinder	10.0	300	13.42	12.0(S)	Ref[7]
	DWCNTs	2-layer cylinder	10.0	500	14.36	14.0(S)	Ref[7]
He	MWCNTs*	Inf. layer cylinder	11.8	303	4.17	2.94(E)	Ref[26]

⋆ (S) simulation data; (E) experimental data

* with carbon impurities

6.4 Conclusions

The isosteric heat of adsorption and Henry's law constant have been calculated on multi-wall carbon surfaces with different geometries using a simple summation method for several gas molecules. The pore width, surface mean curvature, and temperature dependences of Henry's law constant have been investigated in this paper. Single maxima have been found for the Henry's law constant for carbon surfaces with different geometries. Pore width and surface mean curvature play essential roles in determining the Henry's law constants.

The isosteric heats of adsorption for multi-wall carbon nanopores are higher than those of single wall carbon nanopores given the same pore width. Importantly, the pore widths corresponding to the maximum heats of adsorption do not change significantly for carbon walls with different numbers of layers for the same geometry. Larger surface mean curvature still leads to a larger heat of adsorption for multi-wall carbon surfaces. The first layer of wall contributes most to the maximum heat of adsorption in a multilayer wall. For argon adsorbed on multi-wall carbon surfaces, over 95% of the total maximum heat of adsorption comes from the first two layers of the wall, and over 99% derives from the first seven layers of the wall. Our results for isosteric heats of adsorption and Henry's law constants agree reasonably well with experimental and simulation results in the literature.

6.5 Appendix

As discussed in the main text, the calculated Henry's law constant is negative for small pores at high temperatures. This is due to the use of absolute void volumes in the analysis,[8] which historically has been the common approach. This appendix shows how to convert results from an absolute void volume basis to an accessible void volume basis, thereby avoiding the negative Henry's law constants.

The Henry's law constant is the ratio of the excess adsorption amount over the pressure when both are approaching zero. Henry's law constants based on absolute void volumes and accessible void volumes both account for the excess adsorption but do so with allowance for the different volumes. The Henry's law constant given by equation 6.6, noting the two terms of the equation in braces, is of the form

$$K_{\mathrm{H}}^{(abs)} = \frac{1}{A}(\frac{n}{P} - \frac{\bar{n}^{(abs)}}{P}) = \frac{1}{A}(\frac{n}{P} - \frac{V^{(abs)}}{RT}) \tag{6.7}$$

where $\bar{n}^{(abs)}$ and $V^{(abs)}$ are the fluid-phase molar density and the adsorbent specific absolute volume. Alternatively, a Henry's law constant based on the accessible volume of the adsorbent is

$$K_{\mathrm{H}}^{(acc)} = \frac{1}{A}(\frac{n}{P} - \frac{\bar{n}^{(acc)}}{P}) = \frac{1}{A}(\frac{n}{P} - \frac{V^{(acc)}}{RT}) \tag{6.8}$$

Thus, for the difference in Henry's law constants, we have simply,

$$\Delta K_{\mathrm{H}} = K_{\mathrm{H}}^{(acc)} - K_{\mathrm{H}}^{(abs)} = \frac{V^{(abs)} - V^{(acc)}}{ART} = \frac{V^{(inacc)}}{ART} \tag{6.9}$$

where $V^{(inacc)}$ is the specific inaccessible volume of the adsorbent.

Following Do et al.,[8] we choose the dividing surface for the accessible void volume to be the surface where the solid-fluid potential (i.e., the external wall potential V_{ext} in this paper) is zero. The region of inaccessible volume is then bounded by this dividing surface and the outermost surface of the absolute void volume. Equation 6.9 can then be written

$$\Delta K_{\mathrm{H}} = K_{\mathrm{H}}^{(acc)} - K_{\mathrm{H}}^{(abs)} = \frac{1}{ART} \int_{\mathrm{V}^{(\mathrm{s})}} \left\{ 1 - \left(\frac{R_1}{R_2} \right)^n \right\} \, d\mathbf{r}_i \tag{6.10}$$

where R_1 is the distance between the center of the pore axis and the center of the atom on the dividing surface, R_2 is the distance between the center of the pore axis and the center of the atom on the outermost surface of the absolute void volume, and $n = 1$, 2, and 3 for slit-shaped, cylindrical, and spherical geometries, respectively. Using equation 6.9 or 6.10 gives for the three geometries

$$\Delta K_{\mathrm{H,\ slit}} = \frac{1}{RT} \left(R_2 - R_1 \right) \tag{6.11}$$

$$\Delta K_{\mathrm{H,\ cyl}} = \frac{1}{RT} \frac{R_2^2 - R_1^2}{2R_2} \tag{6.12}$$

$$\Delta K_{\mathrm{H,\ sph}} = \frac{1}{RT} \frac{R_2^3 - R_1^3}{3R_2^2} \tag{6.13}$$

Thus, it is clear from these equations that $(RT/R_2)\Delta K_{\mathrm{H}}$ is given as a simple function of R_1/R_2 for the three geometries.

Values of R_1/R_2 were determined as a function of σ_{sf}/R_2 for a single layer wall for all three geometries and are shown in Fig. 6.9. These were obtained by solving equations 7.2-7.4 with $V_{\mathrm{ext}} = 0$, $\rho = R_1$, and $R = R_2$. The slope of the large pore asymptote shown in Fig. 6.9 for all three geometries corresponds to $R_2 - R_1 = 0.8584\,\sigma_{\mathrm{sf}}$. Thus, the thickness of the layer of inaccessable volume is somewhat less than σ_{sf} as the result of the Lennard-Jones potential and the attraction of the molecule by multiple carbon atoms in the first layer of the wall.

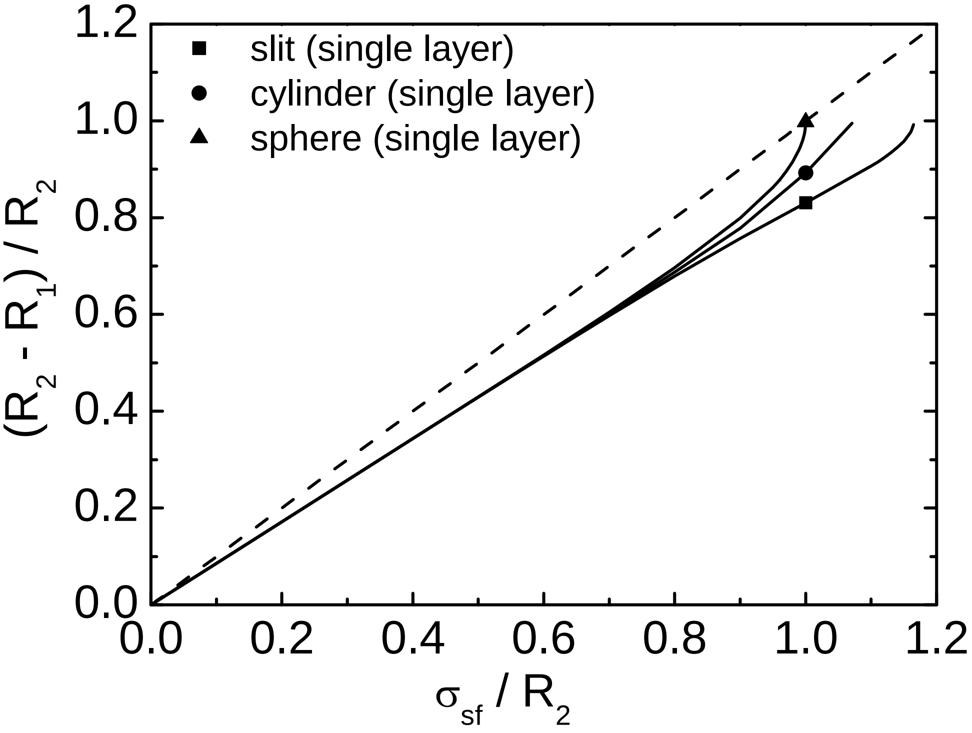

Figure 6.9: Positions of surfaces where zero solid-fluid potentials occur for gas molecules adsorbed in single layer carbon pores with different geometries.

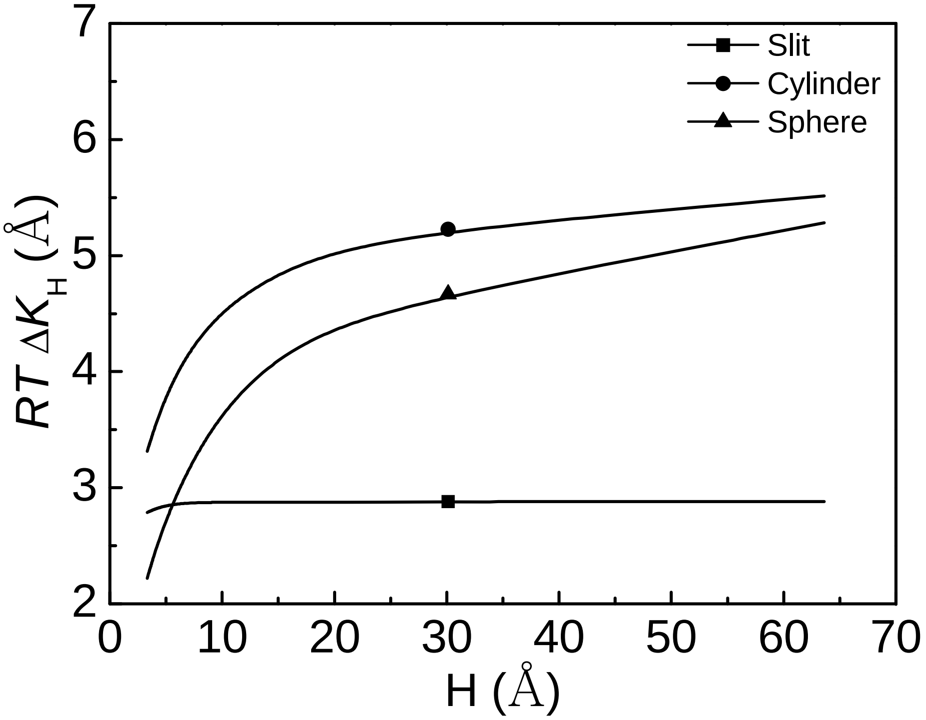

Figure 6.10: Difference between the Henry's law constants obtained by using accessible void volume and absolute void volume for Ar adsorbed in single wall carbon cylindrical nanopores with different geometries and pore widths.

As an example, consider the adsorption of argon in single wall carbon nanopores. Values of $RT\,\Delta K_{\mathrm{H}}$ were calculated as a function of pore width for all there geometries. Results are shown in Fig. 6.10. Henry's law constants obtained by using the accessible void volume are close to the results obtained by using the absolute void volume, with $K_{\mathrm{H}}^{(acc)}$ being slightly larger than $K_{\mathrm{H}}^{(abs)}$, because inaccessible volume is always present. As shown in Fig. 6.10, for the cylindrical and spherical geometries, as the pore width increases, the difference in Henry's law constants increases; the primary reason for this is the increase in the total inaccessable volume for these geometries created by the expansion of wall area with increasing pore width. The differences between the two Henry's law constants we obtained here are consistent with results in the literature.[7,8] At high temperatures (e.g., 1000 K), where potentially negative values can be obtained for Henry's law constants based on the absolute void volume, the Henry's law constants calculated by using the accessible void volume are small positive values.

References

[1] Steele, W. A. The interaction of gases with solid surfaces. Oxford: Pergamon Press; 1974.

[2] Vernov, A.; Steele, W. A. Computer simulation of benzene adsorbed on graphite. 1. *Langmuir* **1991**, *7*, 3110–3117.

[3] Floess, J. K.; Vanlishout, Y. Calculation of adsorption energies in carbon micropores. *Carbon* **1992**, *30*, 967–973.

[4] Pikunic, J.; Clinard, C.; Cohaut, N.; Gubbins, K. E.; Guet, J.; Pellenq, J. M. Structure modeling of porous carbons: constrained reverse Monte Carlo method. *Langmuir* **2003**, *19*, 8565–8582.

[5] Schindler, B. J.; LeVan, M. D. The Theoretical Maximum Isosteric Heat of Adsorption in The Henry's Law Region for Slit-Shaped Carbon Nanopores. *Carbon* **2008**, *46*, 644–648.

[6] Jiang, J. W.; Wagner, N. J.; Sandler, S. I. A Monte Carlo Simulation Study of The Effect of Carbon Topology on Nitrogen Adsorption on Graphite, A Nanotube Bundle, C_{60} Fullerite, C_{168} Schwarzite, and A Nanoporous Carbon. *Phys. Chem. Chem. Phys.* **2004**, *6*, 4440–4444.

[7] Do, D. D.; Do, H.D.; Wongkblap, A.; Nicholson, D. Henry constant and isosteric heat at zero-loading for gas adsorption in carbon nanotubes. *Phys. Chem. Chem. Phys.* **2008**, *10*, 7293–7303.

[8] Do, D. D.; Nicholson, D.; Do, H. D. On the Henry constant and isosteric heat at zero loading in gas phase adsorption. *J. Colloid Interface Sci.* **2008**,*324*, 15–24.

[9] Liu, J.; LeVan, M. D. Isosteric heats of adsorption in the Henry's Law region for carbon single wall cylindrical nanopores and spherical nanocavities. *Carbon* **2009**, *47*, 3415–3423.

[10] Tjatjopoulos, G. J.; Feke, D. L.; Adin Mann, Jr. J. Molecule-micropore interaction potentials. *J. Phys. Chem.* **1988**, *92*, 4006–4007.

[11] Baksh, M. S. A.; Yang, R. T. Model for spherical nanocavity radii and potential functions of sorbated in zeolites. *AlChE J.* **1991**, *37*, 923–30.

[12] Everett, D. H.; Powl, J. C. Adsorption in slit-like and cylindrical micropores in the henry's law region. *J. Chem. Soc. Faraday. Trans. I* **1976**, *72*, 619–636.

[13] Bandosz, T. J.; Biggs, M. J.; Gubbins, K. E.; Hattori, Y.; Iiyama, T.; Kaneko, K.; Pikunic, J.; Thomson, K. T. Molecular Models of Porous Carbons. *Chem. Phys. Carbon* **2003**, *28*, 41–228.

[14] Ryshik, I. M.; Gradstein, I. S. *Table of Integrals, Series, and Products*; Academic Press: New York, 1980.

[15] Steele W. The physical interaction of gases with crystalline solids. Surf Sci 1973;36:317–52.

[16] Steele, W. A. The Physical Interaction of Gases with Crystalline Solids. *Surf. Sci.* **1973**,*36*, 317–352.

[17] Fischer, J.; Fluids at interfaces. Molecular based study of fluids. Advances in Chemistry Series 204 Chapter 6. Washington, DC: American Chemical Society; 1983.

[18] Do, D. D.; Do, D. H. Adsorption of Carbon Tetrachloride On Graphitized Thermal Carbon Black and In Slit Grahitic Pores: Five-Site versus One-Site Potential Models. *J. Phys. Chem. B* **2006**, *110*, 9520–9528.

[19] Do, D. D.; Do, D. H. Appropriate Volumes for Adsorption Isotherm Studies: The Absolute Void Volume, Accessible Pore Volume and Enclosing Particle Volume. *J. Colloid Interface Sci.* **2007**, *316*, 317–330.

[20] Maurer, S.; Mersmann, A.; Peukert, W. Henry coefficients of adsorption predicted from solid Hamaker constants. *Chem. Eng. Sci.* **2001**, *56*, 3443–3453.

[21] Dillon, A. C.; Jones, K. M.; Bekkedahl, T. A.; Kiang, C. H.; Bethune, D. S.; Heben, M. J. Storage of hydrogen in single-walled carbon nanotubes. *Nature* **1997**, *386*, 377–379.

[22] Tanaka, H.; EI-Merraoui, M.; Steele, W. A.; Kaneko, K. Methane adsorption on single-walled carbon nanotube: a density functional theory model. *Chem. Phys. Lett.* **2002**, *352*, 334–341.

[23] Cheng, F.; Liang, J.; Zhao, J.; Tao, Z.; Chen, J. Biomass waste-derived microporous carbons with controlled texture and enhanced hydrogen uptake. *Chem. Mater.* **2008**, *20*, 1889–1895.

[24] Zhou, L.; Sun, Y.; Yang, Z.; Zhou, Y. Hydrogen and methane sorption in dry and water-loaded multiwall carbon nanotubes. *J. Colloid Interface Sci.* **2005**, *289*, 347–351.

[25] Erdogan, F. O.; Kopac, T. Dynamic analysis of sorption of hydrogen in activated carbon. *Int. J. Hydrogen Energy* **2007**, *32*, 3448–3456.

[26] Kopac, T.; Karaaslan, T. H_2, He and Ar sorption on arc-produced cathode deposit consisting of multiwalled carbon nanotubes–graphitic and diamond-like carbon. *Int. J. Hydrogen Energy* **2007**, *32*, 3990–3997.

[27] Hilding, J. M.; Grulke, E. A. Heat of adsorption of butane on multiwalled carbon nanotubes. *J. Phys. Chem. B* **2004**, *108*, 13688–13695.

[28] Zhao, X.; Liu, Y.; Inoue, S.; Suzuki, T.; Jones, R. O.; Ando, Y. Smallest carbon nanotube is 3 Å in diameter. *Phys. Rev. Lett.* **2004**,*92*, 125502.

[29] Guan, L.; Suenaga, K.; Iijima, S. Smallest carbon nanotube assigned with atomic resolution accuracy. *Nano. Lett.* **2008**, *8*, 459–462.

CHAPTER VII

ACCESSIBLE VOLUME FOR ADSORPTION IN CARBON NANOPORES OF DIFFERENT GEOMETRIES AND WALL THICKNESSES

7.1 Introduction

The Henry's law constant of an adsorption isotherm and the isosteric heat of adsorption are important measures of gas adsorption affinity. Besides direct measurements and evaluation using isotherm data, theoretical calculations of Henry's law constants and isosteric heats of adsorption based on statistical thermodynamics are numerous.[1–10] The selection of an appropriate pore volume and pore radius for the calculation of these properties is important. For example, the equation that Steele and others adopted to calculate the Henry's law constant is based on an absolute void volume, which causes the Henry's law constant at high temperatures to be negative, as first discovered by Do and coworkers. The negative Henry's law constant can be avoided by replacing the absolute void volume with an accessible pore volume.[9,10]

Do et al.[9,10] proposed that the outer boundary of the accessible pore volume be where the external wall potential is zero for Lennard-Jones (LJ) gas molecules in the limit of zero loading. The accessible void volume was then determined using Monte Carlo integration. Do and coauthors[11–13] also defined an accessible pore size as the diameter of the largest sphere than can be put inside the accessible volume using a Tri-POD method. They pointed out that accessible pore radius and accessible pore volume vary for gas molecules with different LJ parameters.

In this paper, we adopt the definition of accessible pore volume of Do et al.[9,10] and apply it to planar, cylindrical, and spherical geometries. We investigate the effects of pore radius or half width, pore geometry, and the number of carbon layers forming the pore wall on the accessible pore radius or half width. The results of our geometrical method can be easily applied to estimate accessible pore volumes for LJ molecules adsorbed in a wide variety of carbon nanopores.

7.2 Theory

Slit-shaped, cylindrical, and spherical single wall carbon nanopore and graphene model potentials and parameters are taken from the literature.[6,7,14,15] Gas molecules and carbon atoms are described by a single site model. The carbon atoms are assumed to be uniformly distributed over the wall with specific surface number densities. As in our previous papers,[7,8] adsorbate-adsorbate interactions are neglected because of the infinitesimal gas concentration in the Henry's law region. The site-to-site interactions are described by the LJ potential. The LJ parameters and properties used in this paper is listed in Table 7.1.[7]

Averaged external wall potentials are obtained by integrating the pairwise LJ potential over the inner spaces of the pores to account for all carbon atoms for a flat plane, a slit-shaped pore, a cylindrical pore, and a spherical cavity[14,15]

For the various geometries, the distance between the centers of the carbon atoms on opposing walls of the pore will be referred to as pore diameter, and R is half of the pore diameter, i.e., the perpendicular distance from the center of a carbon

Table 7.1: LJ parameters and surface carbon number densities for different geometries.

Item	Value	References
Argon	$\sigma_{\mathrm{sf}} = 3.35$ Å	Ref[6,16]
	$\epsilon_{\mathrm{sf}}/\mathrm{k} = 55.0$ K	Ref[6,16]
Carbon	$\sigma_{\mathrm{ss}} = 3.38$ Å	Ref[6,9,16]
	layer spacing = 3.35 Å	Ref[6,9,16]
n_{s}	sphere = 4.10×10^{19} m^{-2}	Ref[7]
	others = 3.82×10^{19} m^{-2}	Ref[7,17]

atom to the center axis of the pore. ρ is the perpendicular distance from the center axis of the pore to the center of a fluid molecule. We assume that adsorption occurs only on the internal surface of the pores, except for graphene which has adsorption on a single side. Furthermore, a small opening is assumed to exist into a spherical nanocavity; this allows gas molecules to pass through the cavity wall while having little effect on the overall solid-fluid potential.

For a planar graphene surface, the external wall potential is given by[14]

$$V_{\text{ext, graphene}} = 8\pi n_{\text{s}}\epsilon_{\text{sf}}\sigma_{\text{sf}}^2 \left[\frac{1}{10}\left(\frac{\sigma_{\text{sf}}}{R}\right)^{10}\left(1-\frac{\rho}{R}\right)^{-10} - \frac{1}{4}\left(\frac{\sigma_{\text{sf}}}{R}\right)^{4}\left(1-\frac{\rho}{R}\right)^{-4}\right] \tag{7.1}$$

where n_{s} is the carbon number density (atoms per unit pore surface area). ϵ_{sf} and σ_{sf} are the solid-fluid well depth potential and the solid-fluid collision diameter and are often evaluated using the Lorentz-Berthelot mixing rules, i.e., $\epsilon_{\text{sf}} = (\epsilon_{\text{ss}}\,\epsilon_{\text{ff}})^{1/2}$ and $\sigma_{\text{sf}} = (\sigma_{\text{ss}} + \sigma_{\text{ff}})/2$. Equation 7.1 has been written using notation that allows easy comparison with pore geometries. For the graphene sheet, the normal distance of a gas molecule from the center of the plane of carbon atoms in the smoothed wall is $R - \rho$.

The remaining potentials are more complicated because of the effects of surrounding walls. For the parallel-sided slit-shaped pore, the external wall potential is given by[7,14,18]

$$\begin{aligned} V_{\text{ext, slit}} = {} & 8\pi n_{\text{s}}\epsilon_{\text{sf}}\sigma_{\text{sf}}^2 \left\{\frac{1}{10}\left(\frac{\sigma_{\text{sf}}}{R}\right)^{10}\left[\left(1-\frac{\rho}{R}\right)^{-10} + \left(1+\frac{\rho}{R}\right)^{-10}\right]\right. \\ & \left. -\frac{1}{4}\left(\frac{\sigma_{\text{sf}}}{R}\right)^{4}\left[\left(1-\frac{\rho}{R}\right)^{-4} + \left(1+\frac{\rho}{R}\right)^{-4}\right]\right\} \end{aligned} \tag{7.2}$$

Similarly, for cylindrical geometry, we have[10,14]

$$\begin{aligned} V_{\text{ext, cyl}} = {} & n_{\text{s}}\pi^2\epsilon_{\text{sf}}\sigma_{\text{sf}}^2 \left\{\frac{63}{32}\left[\frac{R-\rho}{\sigma_{\text{sf}}}\left(1+\frac{\rho}{R}\right)\right]^{-10} \times F\left[-\frac{9}{2}, -\frac{9}{2}; 1; \left(\frac{\rho}{R}\right)^2\right]\right. \\ & \left. -3\left[\frac{R-\rho}{\sigma_{\text{sf}}}\left(1+\frac{\rho}{R}\right)\right]^{-4} \times F\left[-\frac{3}{2}, -\frac{3}{2}; 1; \left(\frac{\rho}{R}\right)^2\right]\right\} \end{aligned} \tag{7.3}$$

where $F[\alpha, \beta; \gamma; z]$ is the hypergeometric series with parameters α, β, and γ.[19] Finally, for a spherical surface, the external wall potential is[15]

$$\begin{aligned} V_{\text{ext, sph}} = 8\pi R^2 n_{\text{s}} \epsilon_{\text{sf}} \Bigg[& - \left(\frac{\sigma_{\text{sf}}}{R}\right)^6 \frac{1}{4\,(\rho/R)} \left(\frac{1}{(1-\rho/R)^4} - \frac{1}{(1+\rho/R)^4} \right) \\ & + \left(\frac{\sigma_{\text{sf}}}{R}\right)^{12} \frac{1}{10\,(\rho/R)} \left(\frac{1}{(1-\rho/R)^{10}} - \frac{1}{(1+\rho/R)^{10}} \right) \Bigg] \end{aligned} \tag{7.4}$$

Equations 7.2 to 7.4 are external wall potentials for single wall carbon nanopores with different geometries. To obtain the external wall potentials for multi-wall carbon surfaces, following Steele[20, 21] and others,[10, 22–24] we sum the single wall potentials layer by layer as described in our previous paper.[8] Thus, the external wall potentials, whether they are for a wall with a single carbon layer or several layers, are obtained by adding together all two body interactions between a gas molecule and all carbon atoms. Finally, limiting values for the infinite layer wall are obtained when the inclusion of additional layers has no effect on results to the accuracy shown. Thus, the external wall potential will depend both on curvature effects as given by the geometry (i.e., equations 7.1–7.4) and on the number of layers included in the summation for the wall.

Following Do et al.,[11, 12] the accessible pore radius is defined as the distance between the center of a pore and the center of a gas molecule located where the external wall potential is zero. Our notation is shown in Fig. 7.1. R_2 is the pore radius, or the distance from the center of the pore to the center of carbon atom on the wall. R_1 is the accessible pore radius, or the distance from the center of the pore to the center of a gas molecule located where the external wall potential is zero.

Our calculations are based on argon. Similar calculations can be performed for other probe molecules.

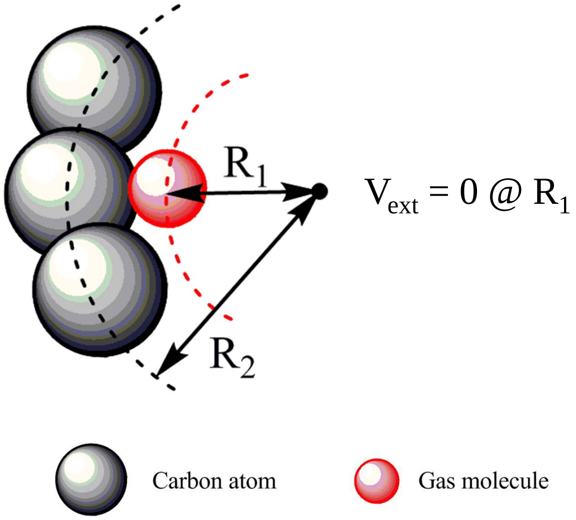

Figure 7.1: Schematic for definition of accessible pore radius.

7.3 Results and Discussion

Accessible pore space for pores with single layer walls

The accessible pore half width or radius for argon adsorbed on graphene and in pores with single layer walls of slit-shaped, cylindrical and spherical geometries were obtained by determining the location where external wall potentials are zero. In solving Equations 7.1–7.4, ρ and R are set to R_1 and R_2, respectively.

Fig. 7.2 shows the width of the inaccessible space next to the wall for a graphene layer and for single walled pores of the three geometries. Results are plotted in a dimensionless way by normalizing with respect to the solid-fluid collision diameter. The x-axis is the dimensionless pore radius. The y-axis is the dimensionless difference between the pore radius and the accessible pore radius or, equivalently, the dimensionless thickness of the inaccessible pore space at the pore wall. This variable indicates how close the center of a gas molecule can approach the center of a carbon atom. As shown in Fig. 7.2, the dimensionless inaccessible space for graphene is constant, always 0.8584, which can be determined from the external wall potential for the graphene, Equation 7.1. Do et al.[24] first reported zero positions for gas adsorbed on flat surfaces with single and multilayer walls. The zero potential position was found at 0.8584 σ_{sf} for a flat surface with single layer wall.

Note that for a gas molecule interacting with a single carbon atom, the zero potential position occurs at $R_2 - R_1 = \sigma_{\text{sf}}$, i.e., at a dimensionless inaccessible pore space of unity. For the graphene sheet, this position is closer to the wall, at 0.8584. This results from the repulsion of the gas molecule by the closest carbon atoms in the graphene sheet being exactly balanced by attraction of the gas molecule by carbon atoms farther away in the graphene sheet.

For the three pore geometries shown in Fig. 7.2, the inaccessible pore space approaches 0.8584 asymptotically as the pore size increases. In this limit, the pore

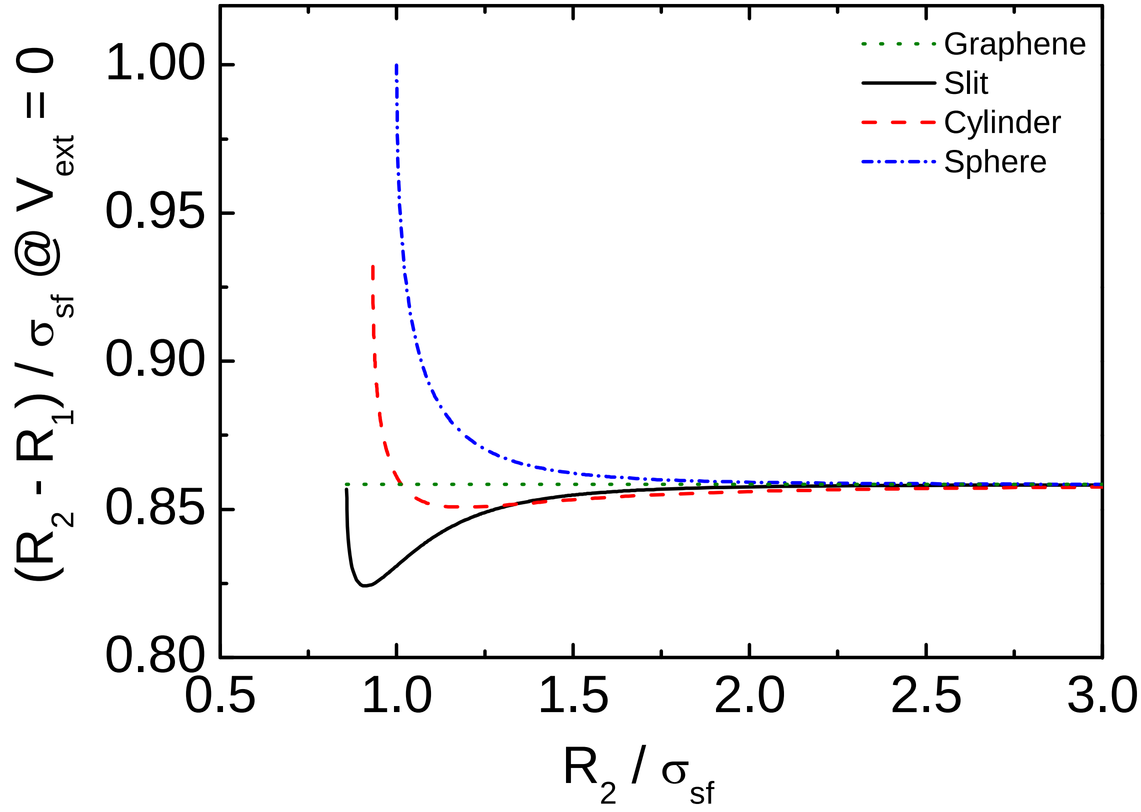

Figure 7.2: Inaccessible pore space for Ar adsorbed on graphene and in pores with slit-shaped, cylindrical, and spherical geometries as a function of pore diameter.

sizes become so large that the differences in surface curvatures for the different geometries disappear and the gas molecule is effectively interacting with a single planar wall. Thus, all systems approach the behavior of the single graphene sheet at very large radii.

The slit-shaped carbon pore with single layer walls is composed of two parallel planes of graphene. In contrast to the results for a single layer of graphene, the inaccessable space for the slit-shaped pore has a minimum in the inaccessible pore space as shown in Fig. 7.2. This minimum is $(R_2 - R_1)/\sigma_{\mathrm{sf}} = 0.8242$ and occurs at a dimensionless pore radius of 0.9157. This minimum can be explained by a superposition effect involving the two walls as illustrated in Fig. 7.3. The pores have two walls, Wall A and Wall B, as indicated by vertical lines. We first consider the gas molecule to be closer to Wall A. Again, the interaction potential between the carbon atoms of the wall and the gas molecule is a integrated LJ potential which is composed of two parts, an attractive potential and a repulsive potential. The attractive potential acts over a longer range than the steeper repulsive potential. As shown in the first diagram of Fig. 7.3, with the walls far apart and the gas molecule close to Wall A, the carbon atoms on Wall B have no significant effect and the gas molecule can penetrate into the carbon wall to a position where the repulsive potential is balanced by the attractive potential giving the dimensionless inaccessible pore space of 0.8584 of the single graphene sheet. As the pore width decreases further, with Wall B moving toward Wall A as shown in the second diagram of Fig. 7.3, the net potential between the gas molecule and Wall B becomes attractive and this can be balanced by a net repulsive potential between the gas molecule and Wall A in order for the total potential determining accessibility to be zero. Thus, the gas molecule at the zero potential boundary will be closer to Wall A than it was in the first diagram. This explains the decrease in the dimensionless inaccessible pore space of the slit-shaped pore from the large pore asymptote. As Wall B continues to approach Wall A, as shown in the third diagram of Fig. 7.3, a limit is reached for the zero potential surface to exist in the pore. Interestingly, this occurs at the inaccessible pore space distance of 0.8584 on each wall that was found for the single graphene sheet. At this location, attractive and repulsive potentials between the gas molecule and each of the walls are in perfect balance. If the gas molecule were to move towards either wall, then the net repulsive potential with that wall would be greater than the net attractive potential with the other wall because of the steepness of the LJ repulsive potential. Thus, the inaccessible space at a pore wall of the smallest accessible slit-shaped pore is identical to the inaccessible space adjoining the graphene sheet. The curve for the single walled slit-shaped begins and ends at $(R_2 - R_1)/\sigma_{\mathrm{sf}} = 0.8584$.

The results for cylindrical and spherical pores are different from that of the slit-shaped pore as shown in Fig. 7.2. The curve for the cylindrical pore has a shallower and broader minimum than the slit-shaped pore, and the curve for the spherical pore does not even have a minimum. These results can be ascribed to the different surface mean curvatures of the various carbon nanopores. Obviously, the spherical surface has the largest mean curvature among the three geometries given the same pore radius. As is apparent from Fig. 7.1, for a fixed pore dimension, a larger surface mean curvature gives a larger number of carbon atoms close to the gas molecule that influence it strongly in 3-D space.[25] Therefore, when the pore radius decreases from a middle range to a small value for a cylindrical pore, in comparison to the slit-shaped pore a larger number of carbon atoms are present nearby to contribute to the repulsive potential at a relatively larger pore dimension. The minimum then, which balances the net attractive and repulsive potentials, occurs at a larger pore dimension than for the slit-shaped pore. In addition, the curve for the cylindrical pore increases sharply when the dimensionless pore radius is less than unity, because the number of carbon atoms that contribute repulsive potentials increases sharply when the pore radius is smaller than σ_{sf}. Similarly, the dimensionless inaccessible pore space continues to

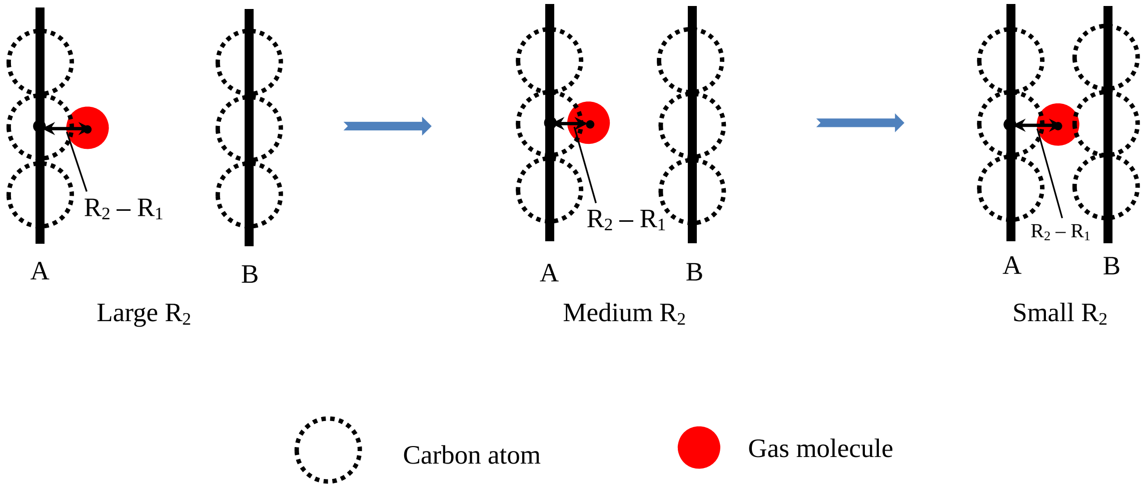

Figure 7.3: Effect of reducing pore radius on accessible volume for slit-shaped pores. Left: walls far apart, $R_2 - R_1 = 0.8584\,\sigma_{\mathrm{sf}}$. Middle: wall B attracting, $R_2 - R_1 < 0.8584\,\sigma_{\mathrm{sf}}$. Right: tightest accessible pore, $R_2 - R_1 = 0.8584\,\sigma_{\mathrm{sf}}$.

increase with a decrease in pore size for the cylindrical pore until it terminates at $R_2/\sigma_{\text{sf}} = 1.0727$, where $(R_2 - R_1)/\sigma_{\text{sf}} = 0.9312$ with the zero potential surface being simply the pore axis.

The spherical pore has an even larger surface mean curvature than the cylindrical pore. As shown in Fig. 7.2, no minimum is found for the inaccessible pore space. As the size of this spherical nanocavity shrinks, the width of this space increases rapidly. The curve terminates at $R_2/\sigma_{\text{sf}} = 1$ at which point $(R_2 - R_1)/\sigma_{\text{sf}} = 1$. At that point, the gas molecule is at zero potential at the center of the spherical cavity. The attractive and repulsive potentials are balanced for interaction with each individual carbon atom forming the spherical nanocavity. The distance of the gas molecule from the wall is exactly that given by the LJ potential at zero potential for the interaction of the gas molecule with a single carbon atom. The spherical pore has the largest width of inaccessible pore space followed by the cylindrical pore and then the slit-shaped pore.

Effect of number of wall layers on the accessible pore space

In addition to considering pores with single layer walls, accessible pore spaces were also investigated for pores with multilayer walls. As mentioned previously, for this case, the position of the zero external wall potential depends also on the spacing between carbon layers.

Results for multilayer slit-shaped, cylindrical, and spherical pores are shown in Figs. 7.4-7.6. Pores with multilayer walls have smaller inaccessible pore spaces compared with pores with single layer walls at fixed pore sizes. This a result of attraction between the gas molecule and carbon atoms in layers beyond the first. Net attractive and repulsive potentials are in balance with the gas molecule being closer to the pore wall. However, layers beyond the second do not cause significant changes in the results. For a particular geometry, curves for pores with two or more layers give almost the same results. This is consistent with a prior result of Do et al.[24] for slit-shaped pores, who also found that the zero position depends on the ratio of the distance between carbon layers to σ_{sf}.

Values of maximum and minimum inaccessible pore spaces for pores with different geometries and numbers of wall layers are summarized in Table 7.2. It is clear that the difference in the maximum and minimum dimensionless inaccessible pore widths between consecutive layers decreases with increasing numbers of layers, as would be expected. For a fixed size pore, the spherical pore has the largest dimensionless inaccessible pore width followed by the cylindrical and slit-shaped pores. The results shows that, for the same R_2, pores with slit-shaped geometry are more accessible than those with cylindrical and spherical geometries.

For pores with slit-shaped and cylindrical geometries, the minimum in the curve for inaccessible pore space occurs at approximately the same value of R_2 for pores with single and multilayer walls. Although the effect is slight and not readily apparent in Fig. 7.6, spherical pores with multilayer walls have very shallow minima, in contrast to the single wall spherical pores which showed no minimum. The outer shells, being curved less than the first shell, help to balance attractive and repulsive forces for a molecule closer to the wall. Evidence of this effect is found further in the termination of the curves at values of R_2/σ_{sf} slightly less than unity.

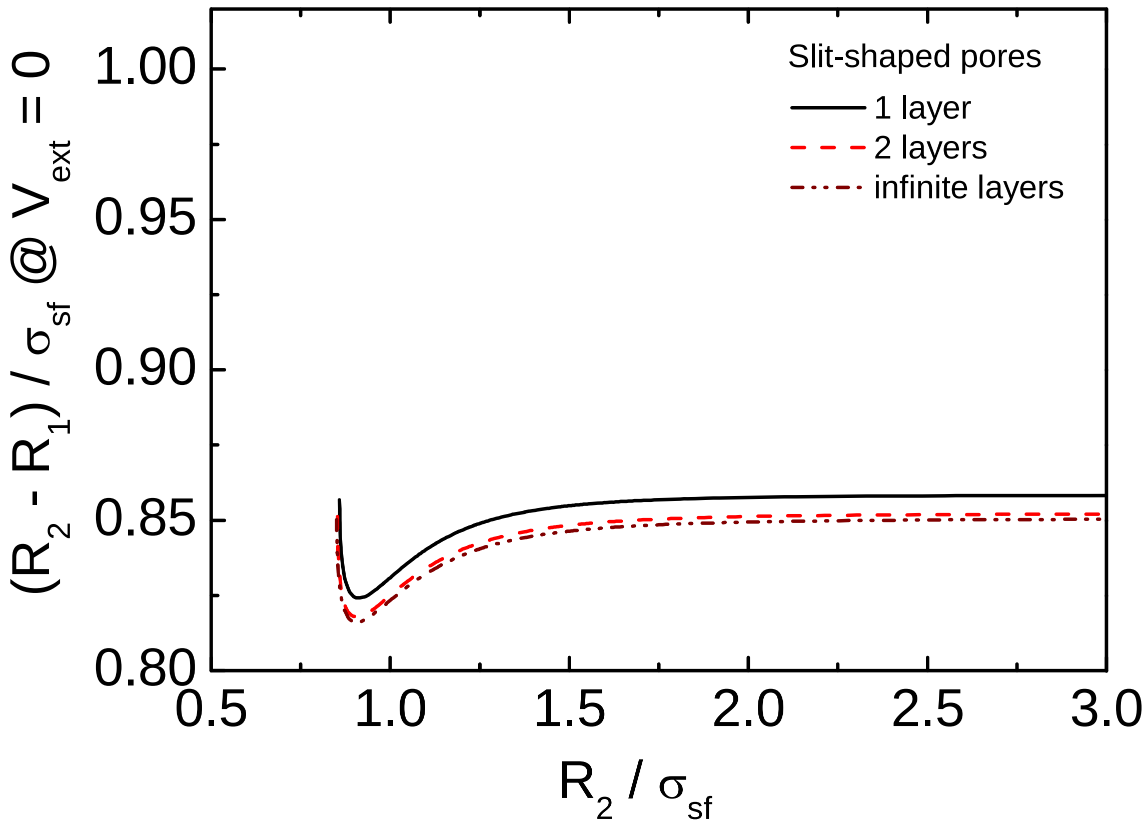

Figure 7.4: Inaccessible pore space for slit-shaped pores with multilayered walls.

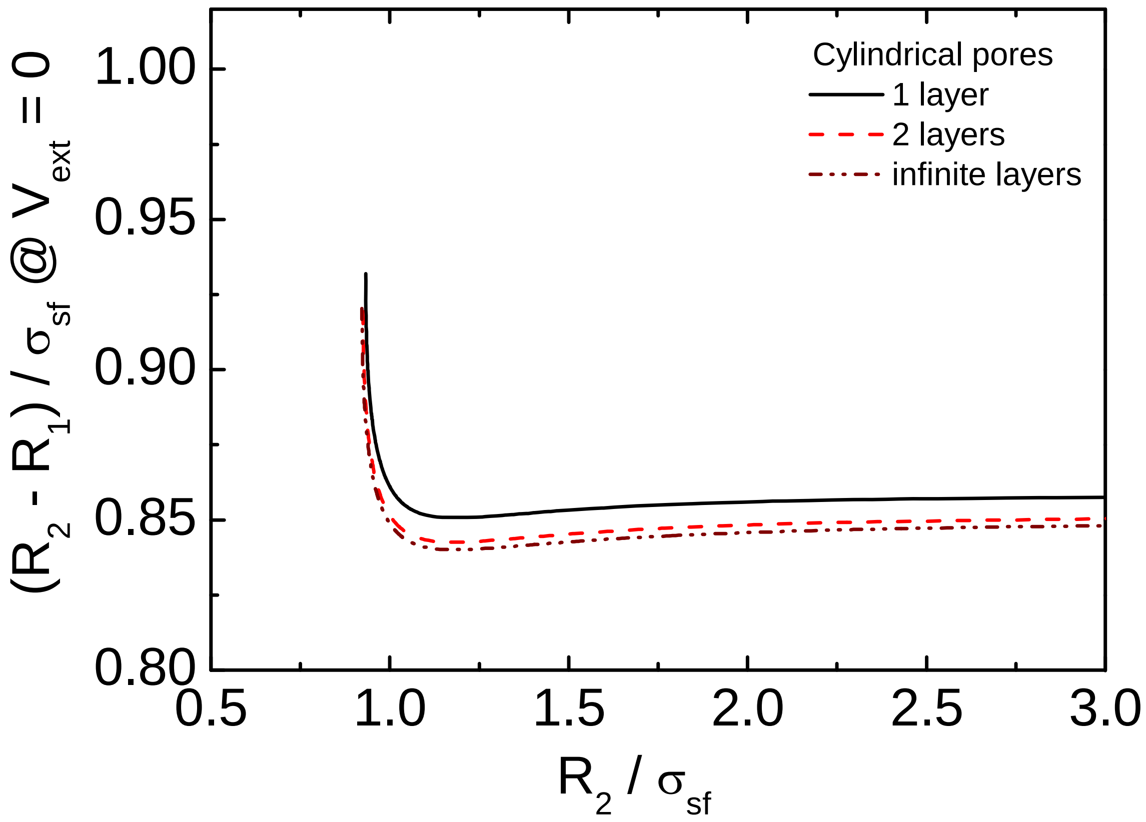

Figure 7.5: Inaccessible pore space for cylindrical pores with multilayered walls.

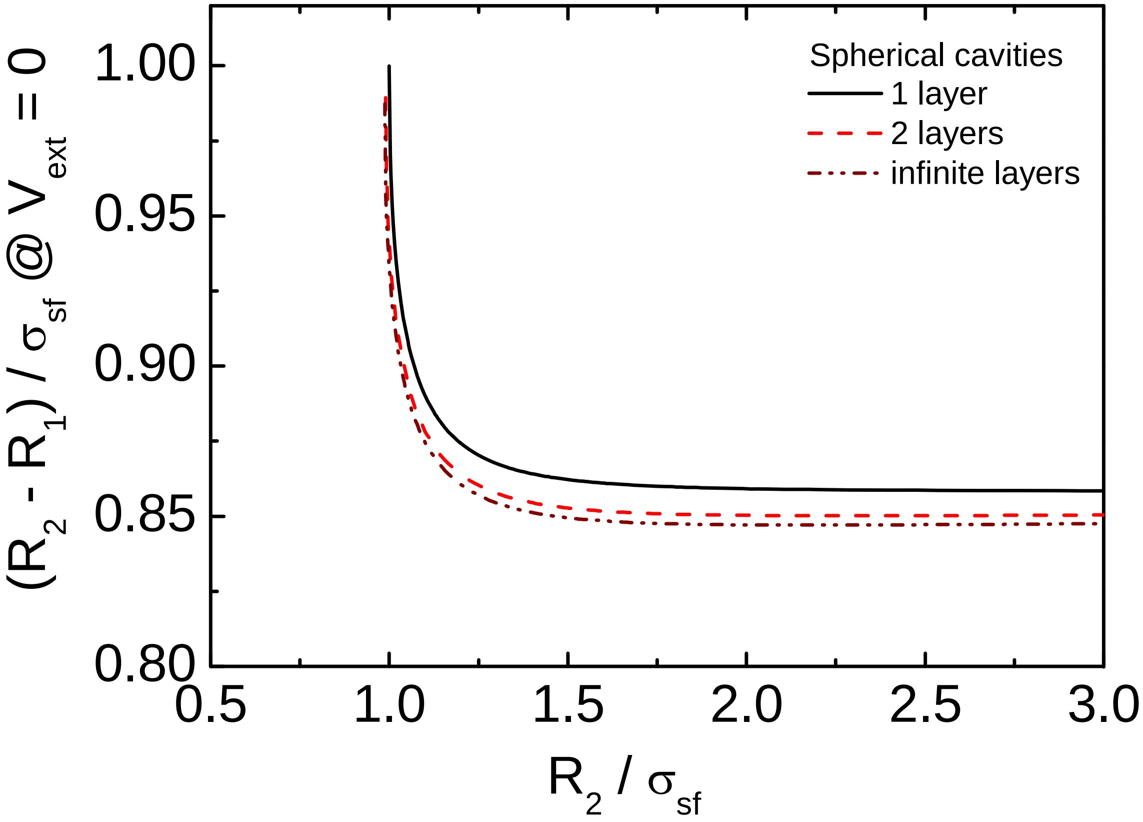

Figure 7.6: Inaccessible pore space for spherical pores with multilayered walls.

Table 7.2: Limiting dimensionless inaccessible pore spaces for pores with different geometries and numbers of wall layers. Values are $(R_2 - R_1)/\sigma_{\mathrm{sf}}$.

Layers of wall	Slit-shaped pore		Cylindrical pore		Spherical pore	
	min	max	min	max	min	max
1	0.8242	0.8584	0.8508	0.9312	0.8584	1.000
2	0.8179	0.8522	0.8426	0.9232	0.8502	0.9894
3	0.8168	0.8512	0.8411	0.9204	0.8484	0.9861
4	0.8164	0.8508	0.8410	0.9188	0.8478	0.9847
∞	0.8161	0.8506	0.8401	0.9187	0.8471	0.9836

7.4 Conclusions

A geometric method was used to study accessible pore space as a function of pore dimension for slit-shaped, cylindrical, and spherical carbon pores. Pores walls with single layers and multiple layers of carbon were considered.

The inaccessible pore space at the pore wall was found to depend on both pore geometry and number of wall layers. Surface mean curvature was found to be quite important in determining the relationship between the accessible pore space and the pore dimension when the pore size is comparable to the size of the adsorbate. In general, pores with small surface mean curvature are more accessible to gas molecule than those with larger surface mean curvature given the same characteristic pore dimension. Slit-shaped pores have less inaccessible pore space at the wall than cylindrical pores, which have less inaccessible space than spherical pores. Pores with multilayer walls have less inaccessible pore space than pores with a single wall. Adding layers to the wall helps to increase the size of the accessible pore space, but this effect is quite small after the second layer for pores of all three geometries.

For very large pores with a single layer wall, the dimensionless accessible pore space is not sensitive to the pore radius and a universal limit for the width of the inaccessible pore space exists for the different geometries because of the diminishing surface mean curvatures of the geometries. In this limit, all pores behave like a single sheet of graphene.

Limits were determined for the smallest pores having accessible space. For the slit-shaped pore with a single wall, the minimum pore half width is 0.8584 σ_{sf}, which is also the width of the inaccessible layer at the wall for a single graphene sheet. In contrast, the minimum radius of a spherical pore with accessible space is σ_{sf}, the Lennard-Jones collision diameter.

References

[1] Steele, W. A. *The interaction of gases with solid surfaces*; Pergamon Press: Oxford, 1974.

[2] Everett, D. H.; Powl, J. C. Adsorption in Slit-Like and Cylindrical Micropores in The Henry's Law Region. *J. Chem. Soc. Faraday Trans. I* **1976**, *72*, 619–636.

[3] Vernov, A.; Steele, W. A. Computer Simulation of Benzene Adsorbed on Graphite. 1. *Langmuir* **1991**, *7*, 3110–3117.

[4] Floess, J. K.; Vanlishout, Y. Calculation of Adsorption Energies in Carbon Micropores. *Carbon* **1992**, *30*, 967–973.

[5] Pikunic, J.; Clinard, C.; Cohaut, N.; Gubbins, K. E.; Guet, J.; Pellenq, J. M.; Rannou, I.; Rouzaud, J. N. Structure Modeling of Porous Carbons: Constrained Reverse Monte Carlo Method. *Langmuir* **2003**, *19*, 8565–8582.

[6] Schindler, B. J.; LeVan, M. D. The Theoretical Maximum Isosteric Heat of Adsorption in The Henry's Law Region for Slit-Shaped Carbon Nanopores. *Carbon* **2008**, *46*, 644–648.

[7] Liu, J.; LeVan, M. D. Isosteric Heats of Adsorption in The Henry's Law Region for Carbon Single Wall Cylindrical Nanopores and Spherical Nanocavities. *Carbon* **2009**, *47*, 3415–3423.

[8] Liu, J.; LeVan, M. D. Henry's Law Constants and Isosteric Heats of Adsorption at Zero Loading for Multi-Wall Carbon Surfaces with Different Geometries. *Carbon* **2010**,*48*, 3454–3462.

[9] Do, D. D.; Nicholson, D.; Do, D. H. On the Henry Constant and Isosteric Heat at Zero Loading in Gas Phase Adsorption. *J. Colloid Interface Sci.* **2008**, *324*, 15–24.

[10] Do, D. D.; Do, H. D.; Wongkblap, A.; Nicholson, D. Henry Constant and Isosteric Heat at Zero-Loading for Gas Adsorption in Carbon Nanotubes. *Phys. Chem. Chem. Phys.* **2008**,*10*, 7293–7303.

[11] Do, D. D.; Herrera, L. F.; Do, D. H. A New Method to Determine Pore Size and Its Volume Distribution of Porous Solids Having Known Atomistic Configuration. *J. Colloid Interface Sci.* **2008**, *328*, 110–119.

[12] Do, D. D.; Herrera, L. F.; Fan, C. Y.; Wongkblap, A.; Nicholson, D. The Role of Accessibility In the Characterization of Porous Solids and Their Adsorption Properties. *Adsorption* **2010**, *16*, 3–15.

[13] Hererra, L.; Fan, C.Y.; Do, D. D.; Nicholson, D. A Novel and Consistent Method (Tri-POD) to Characterize an Arbitrary Volume Solid for Its Accessible Volume, Accessible Geometrical Surface Area and Accessible Pore Size. *Adsorption* **2011**, *17*, 55–68.

[14] Tjatjopoulos, G. J.; Feke, D. L.; Adin Mann, Jr. J. Molecule-Micropore Interaction Potentials. *J. Phys. Chem.* **1988**, *92*, 4006–4007.

[15] Baksh, M. S. A.; Yang, R. T. Model for Spherical Nanocavity Radii and Potential Functions of Sorbated in Zeolites. *AlChE J.* **1991**,*37*, 923–930.

[16] Ravikovitch, P. I.; Nishnyakov, A.; Russo, R.; Neimark, A. V. Unified approach to pore size characterization of microporous carbonaceous materials for N_2, Ar, and CO_2, adsorption isotherms. *Langmuir* **2000**, *16*, 2311–2320.

[17] Do, D. D. *Adsorption Analysis: Equilibria and Kinetics*; Imperial College Press: London, 1998.

[18] Bandosz, T. J.; Biggs, M. J.; Gubbins, K. E.; Hattori, Y.; Iiyama, T.; Kaneko, K.; Pikunic, J.; Thomson, K. T. Molecular Models of Porous Carbons. *Chem. Phys. Carbon* **2003**, *28*, 41–228.

[19] Ryshik, I. M.; Gradstein, I. S. *Table of Integrals, Series, and Products*; Academic Press: New York, 1980.

[20] Steele, W. A. The Physical Interaction of Gases with Crystalline Solids. *Surf. Sci.* **1973**,*36*, 317–352.

[21] Steele, W. A. Molecular Interaction for Physical Adsorption. *Chem. Rev.* **1993**, *93*, 2355–2376.

[22] Do, D. D.; Do, D. H. Adsorption of Carbon Tetrachloride On Graphitized Thermal Carbon Black and In Slit Grahitic Pores: Five-Site versus One-Site Potential Models. *J. Phys. Chem. B* **2006**, *110*, 9520–9528.

[23] Fischer, J. *Fluids at Interfaces. Molecular Based Study of Fluids*; Advances in Chemistry Series 204 Chapter 6. American Chemical Society: Washington, DC, 1983.

[24] Do, D. D.; Do, D. H. Appropriate Volumes for Adsorption Isotherm Studies: The Absolute Void Volume, Accessible Pore Volume and Enclosing Particle Volume. *J. Colloid Interface Sci.* **2007**, *316*, 317–330.

[25] Jiang, J. W.; Wagner, N. J.; Sandler, S. I. A Monte Carlo Simulation Study of The Effect of Carbon Topology on Nitrogen Adsorption on Graphite, A Nanotube Bundle, C_{60} Fullerite, C_{168} Schwarzite, and A Nanoporous Carbon. *Phys. Chem. Chem. Phys.* **2004**, *6*, 4440–4444.

CHAPTER VIII

CONCLUSIONS AND RECOMMENDATIONS

This dissertation includes research on using MOFs to capture carbon dioxide from flue gases generated from coal-fired power plants and research on studying thermodynamic properties of gas adsorption in carbon nanopores with different geometries and number of wall layers. In the carbon dioxide capture study, over 30 MOF candidates were screened for the highest carbon dioxide capacities at the point of interest (POI), 0.1 atm CO_2 and 100 °F. HKUST-1 and Ni/DOBDC were selected as the best candidates for kinetics and water effect studies. Also, simulated flue gas conditioning effects on the carbon dioxide adsorption in HKUST-1 and Ni/DOBDC were investigated. Finally, Ni/DOBDC was modified with pyridine and the modification effects on H_2O and CO_2 adsorption in Ni/DOBDC were studied.

In the thermodynamic properties calculation study, isosteric heats of adsorption and Henry's law constants for six gas molecules adsorbed in carbon nanopores at zero loading were considered. Effects of geometry and number of wall layers on these thermodynamic properties were examined and general plots were developed to estimate pore diameters where maximum heats of adsorption occur for light gases adsorbed in carbon nanopores. An accessible pore volume was proposed to improve the calculation results of adsorption properties. Pore radius, geometry, and number of wall layer effects on the accessible pore radius were investigated as well.

The principal findings of this research are:

Carbon dioxide capture from flue gases by using MOFs

- We found no correlation between CO_2 capacity of a MOF sample and its surface area or pore volume. CO_2 capacities at the POI for most of the MOFs considered follow a similar trend to the average isosteric heats of adsorption.

High CO_2 capacities generally corresponding to high heats of adsorption in the low pressure range.

- The DOBDC series of MOFs with unsaturated metal centers (UMCs) in their structures are very good for CO_2 adsorption, especially in the low pressure range, because UMCs offer extra adsorption sites for CO_2 adsorption and enhance the heat of adsorption.
- CO_2 mass transfer rates for MOF pellets of HKUST-1 and Ni/DOBDC are fast. The CSFR method can distinguish among different mass transfer resistances. Macropore diffusion was determined to be the rate controlling mechanism for CO_2 adsorption in both HKUST-1 and Ni/DOBDC pellets after comparing and analyzing results for pellets with different thicknesses.
- Adsorption equilibria of CO_2, H_2O, and CO_2/H_2O were studied for HKUST-1, Ni/DOBDC, and Mg/DOBDC. Large CO_2 capacities are found at 25 °C and 0.1 atm CO_2 partial pressure. They are 0.55, 3.28, and 5.65 mol/kg for HKUST-1, Ni/DOBDC, and Mg/DOBDC pellets, respectively. Ni/DOBDC and Mg/DOBDC have higher CO_2 capacities than the benchmark zeolites NaX and 5A at 25 °C and 0.1 atm.
- Adsorbed water vapor impacts CO_2 adsorption in the MOFs. A small amount of H_2O does not decrease and may actually increase the CO_2 capacity of HKUST-1. H_2O does not affect CO_2 adsorption on HKUST-1 and Ni/DOBDC samples as much as on 5A and NaX zeolites, and H_2O would be more easily removed from the MOFs by regeneration. Ni/DOBDC and Mg/DOBDC retain substantial CO_2 capacities with moderate H_2O loadings. Considering the less intensive regeneration processes compared with the benchmark zeolites and substantial CO_2 capacities under moist conditions, Ni/DOBDC and Mg/DOBDC may have a promising future for capturing CO_2 from flue gases provided that costs are

not prohibitive. Ni/DOBDC is more stable than Mg/DOBDC although it has a lower CO_2 capacity at 0.1 atm. However, the overall stability of the DOBDC series of MOFs does not appear to be as good as many of the zeolites.

- Pyridine modification decreases the surface area and the carbon dioxide capacities at the POI for Ni/DOBDC. However, pyridine modified Ni/DOBDC has smaller water capacities than unmodified Ni/DOBDC. The selectivity between water and carbon dioxide dramatically decreases from 5260 for regular Ni/DOBDC to 206 for pyridine modified Ni/DOBDC. When the relative humidity is about 45%, pyridine modified Ni/DOBDC has a carbon dioxide capacity of 0.23 mol/kg and unmodified Ni/DOBDC has a carbon dioxide capacity of 0.10 mol/kg at 25 °C and 0.1 atm.

Thermodynamic properties calculation for gases adsorbed in carbon nanopores

- The isosteric heat of adsorption in the Henry's law region can be calculated as a function of pore radius for light gas molecules adsorbed in both carbon single wall cylindrical nanopores and spherical nanocavities .

- General plots have been generated to conveniently predict pore diameters corresponding to the maximum isosteric heats of adsorption for non-polar or weakly polar molecules adsorbed in carbon nanopores. These plots show constant relationships for straightforward estimation of pore diameters at which maximum isosteric heats of adsorption occur.

- The spherical carbon surface is the most attractive surface for gas molecules in the small pore region because of its large surface mean curvature. Differences in surface mean curvature lead to different maximum isosteric heats of adsorption for gas adsorbed in pores with different geometries. The effects of surface curvature disappears gradually as the pore size increases.

- The isosteric heats of adsorption for multi-wall carbon nanopores are higher than those of single wall carbon nanopores given the same pore width. Importantly, the pore widths corresponding to the maximum heats of adsorption do not change significantly for carbon walls with different numbers of layers for the same geometry. Larger surface mean curvature still leads to a larger heat of adsorption for multi-wall carbon surfaces. The first layer of wall contributes most to the maximum heat of adsorption in a multilayer wall. For argon adsorbed on multi-wall carbon surfaces, over 95% of the total maximum heat of adsorption comes from the first two layers of the wall, and over 99% derives from the first seven layers of the wall. Our results for isosteric heats of adsorption and Henry's law constants agree reasonably well with experimental and simulation results in the literature.

- The inaccessible pore space at the pore wall was found to depend on both pore geometry and number of wall layers. Surface mean curvature was found to be quite important in determining the relationship between the accessible pore space and the pore dimension when the pore size is comparable to the size of the adsorbate. In general, pores with small surface mean curvature are more accessible to gas molecule than those with larger surface mean curvature given the same characteristic pore dimension. Adding layers to the wall helps to increase the size of the accessible pore space, but this effect is quite small after the second layer for pores of all three geometries.

- For very large pores with a single layer wall, the dimensionless accessible pore space is not sensitive to the pore radius and a universal limit for the width of the inaccessible pore space exists for the different geometries because of the diminishing surface mean curvatures of the geometries. In this limit, all pores behave like a single sheet of graphene.

- Limits were determined for the smallest pores having accessible space. For the slit-shaped pore with a single wall, the minimum pore radius is 0.8584 σ_{sf}, which is also the width of the inaccessible layer at the wall for a single graphene sheet. In contrast, the minimum radius of a spherical pore with accessible space is σ_{sf}, the Lennard-Jones solid-fluid collision diameter.

There are opportunities for some of this work to be extended. My recommendations for future research are as follows:

Carbon dioxide capture from flue gases by using MOFs

- Compared with zeolites, MOFs have relatively lower hydrothermal stabilities which limits their applications in industry. It may be possible to combine the MOF structures with other stable phases to produce some composite material that take advantage of the MOFs' high gas capacities and the other phases' enhanced stabilities.

- The water effects on carbon dioxide adsorption is much smaller for HKUST-1 and Ni/DOBDC compared with some benchmark zeolites. However, more work is still needed to diminish the water adsorption in MOFs. Non-polar substances can be used to cover the unsaturated metal centers (UMCs) in these MOFs to reduce the water adsorption. In addition, some other post-synthesis research may help to tailor the hydrophilicity/hydrophobicity of MOFs. Organic ligands can be modified with some functional groups which can be activated after synthesis to modify the surface hydrophilicity/hydrophobicity of MOFs.

- The crystal structures of the DOBDC series of MOFs have UMCs which can lead to strong adsorption of gas molecules. Study of gas molecules besides carbon dioxide adsorbed in the DOBDC series of MOFs could be very interesting. Promising candidates for adsorbates include carbon monoxide, ammonia, and nitric oxide.

Thermodynamic properties calculation for gas adsorbed in carbon nanopores

- The LJ potential was used throughout for calculation of the thermodynamic properties for gas adsorption in carbon nanopores. The LJ potential can be replaced by other interaction potentials or combined with other interaction potentials to account for more complex gas adsorption cases, such as polar gas molecules adsorbed in carbon or other materials.
- An accessible pore radius has been proposed for pure gas adsorption in carbon nanopores with different geometries and number of wall layers. It would be interesting to study the accessibility for mixture adsorption and relate the selectivity to the accessible pore radius instead of the pore radius.

APPENDIX A

STABILITY OF MG/DOBDC AND NI/DOBDC

In this appendix, some stability results for Mg/DOBDC and Ni/DOBDC MOFs, which are two promising candidates for CO_2 capture, will be shown in terms of steaming and aging stabilities.

A.1 Steaming effects

According to the results in Chapter 4, the DOBDC series of MOFs are promising for CO_2 capture from flue gas. In order to assess the stability of MOFs as adsorbents for long term usage, steam was used to condition the two DOBDC series MOF samples. Samples were conditioned with 100 °C steam at fixed humidity (5%) for 2h.[1] CO_2 isotherms were measured and compared for the samples before and after the steaming processes.

The 100 °F CO_2 isotherms for Ni/DOBDC powder before and after 5% steaming are displayed in Fig. A.1. The CO_2 capacities for Ni/DOBDC and Mg/DOBDC before and after 5% steaming are summarized in Table A.1. From Fig. A.1, it is clear that the CO_2 capacity at the POI for the steamed Ni/DOBDC is very close to that of the unsteamed sample. Only a 8.4% loss was found in CO_2 capacity at the POI for the steamed Ni/DOBDC powder as shown in Table A.1.

The 100 °F CO_2 isotherms for Mg/DOBDC before and after 5% steaming

Table A.1: Steaming effects on CO_2 adsorption in DOBDC series MOFs

Sample	n_{CO_2}@POI before steaming	n_{CO_2}@POI after steaming	n_{CO_2}@POI loss
Ni/DOBDC p	2.98 mol/kg	2.73 mol/kg	8.4%
Mg/DOBDC p	4.93 mol/kg	2.41 mol/kg	51.1%

* p denotes powder.

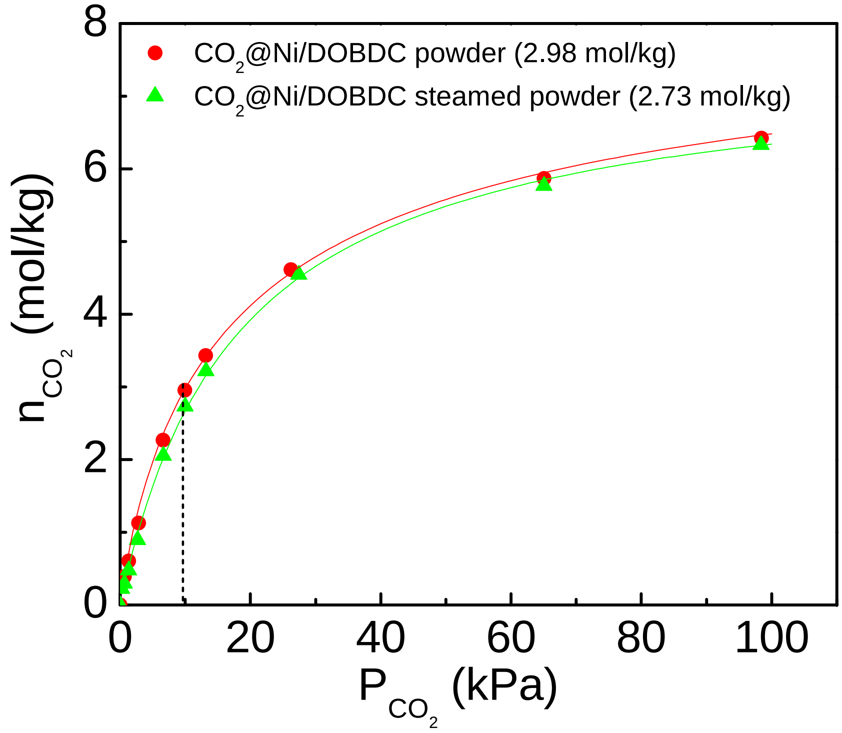

Figure A.1: CO_2 isotherms at 100 °F for Ni/DOBDC powder before and after 5% steaming for 4h.

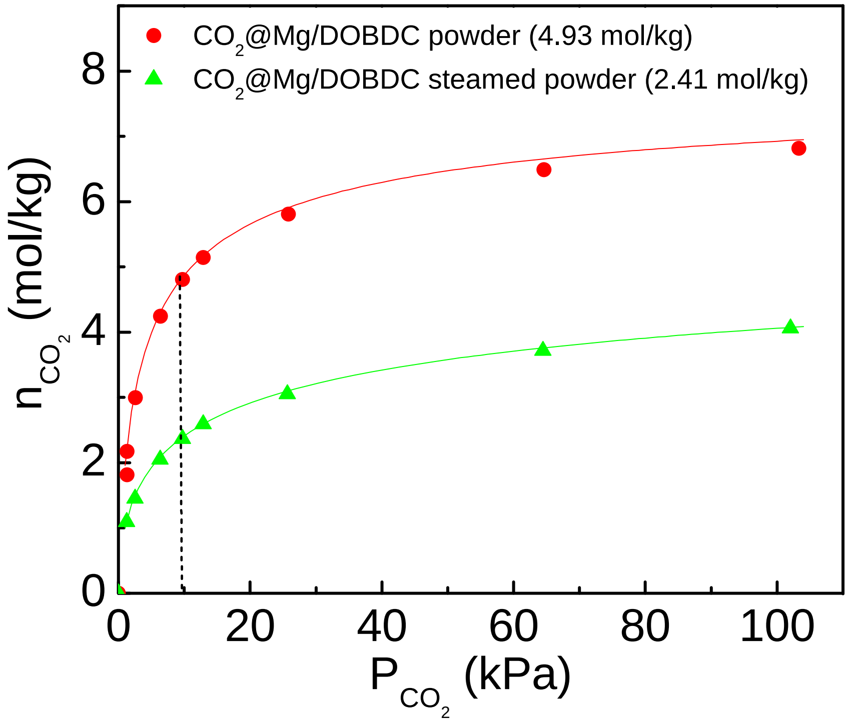

Figure A.2: CO_2 isotherms at 100 °F for Mg/DOBDC powder before and after 5% steaming for 4h.

are displayed in Fig. A.2. In contrast to Ni/DOBDC, Mg/DOBDC lost a significant amount of CO_2 capacity after the 5% steaming process. As shown in Table A.1, a 51.1% loss was found in the CO_2 capacity at the POI for the steamed Mg/DOBDC. Mg/DOBDC has much higher CO_2 capacity at the POI than Ni/DOBDC before steaming. However, the Ni/DOBDC has a higher CO_2 capacity at the POI than Mg/DOBDC after steaming. Therefore, Ni/DOBDC is more stable because it retains its CO_2 capacity better after steaming. A molecular simulation study may help to understand the metal substitution effect.

A.2 Aging effects

Besides the impact on CO_2 capacity caused by steaming, we checked to determine if the two DOBDC series MOFs will lose CO_2 capacity over time with storage. We measured the CO_2 isotherm again for the 2008 Ni/DOBDC sample send to us by UOP in 2010. The aging effect results for 2008 Ni/DOBDC powder are shown in Fig. A.3. The results show that the 2008 Ni/DOBDC maintains its CO_2 capacity, which is about 3.1 mol/kg at the POI, after being stored in a container for about two years. We also measured the CO_2 isotherm again for the 2009 Mg/DOBDC sample in 2010. The 100 °F CO_2 isotherms for the fresh and the aged Mg/DOBDC are compared in Fig. A.4. It is clear that the CO_2 capacity at the POI for aged Mg/DOBDC decreased by about 22.6% compared with the fresh sample, even though the sample had been sealed in its original container and stored inside a desiccator. A longer storage time may cause an even larger relative decrease in CO_2 capacity at the POI for the Mg/DOBDC.

Based on our experimental work, we believe that Ni/DOBDC is more stable than Mg/DOBDC although it has a lower CO_2 capacity at the POI. The overall stability of the DOBDC series of MOFs does not appear to be as good as many of the zeolites.

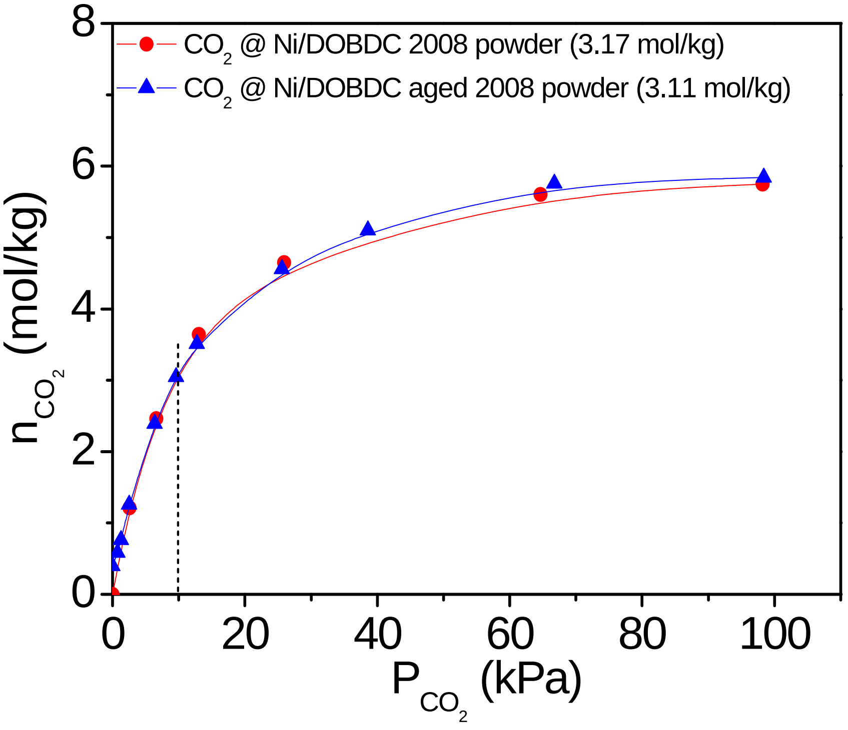

Figure A.3: CO_2 isotherms at 100 °F for fresh Ni/DOBDC powder and aged sample.

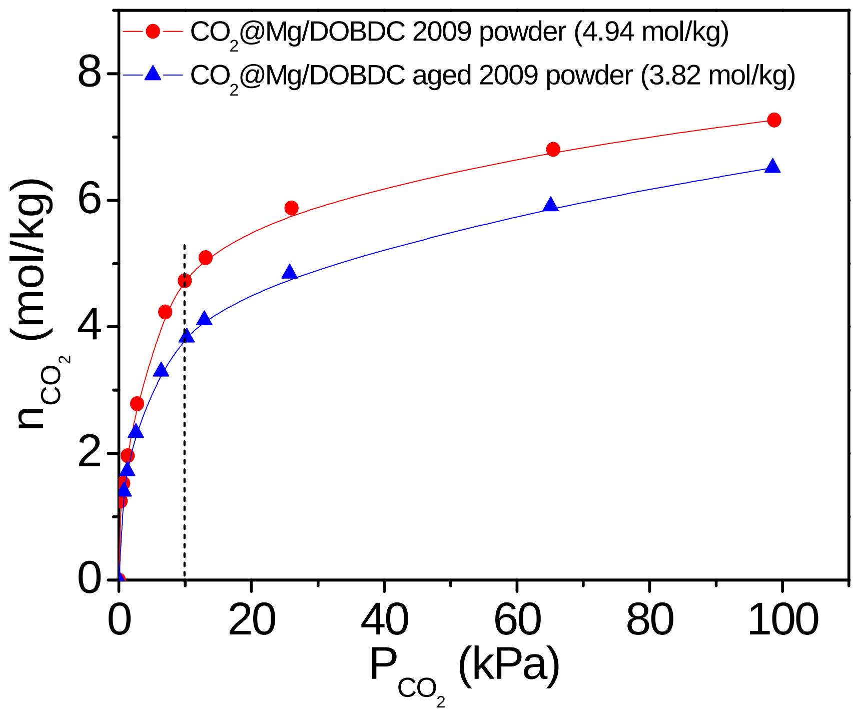

Figure A.4: CO_2 isotherms at 100 °F for fresh Mg/DOBDC powder and aged sample.

References

[1] Low, J. J.; Benin, A. I.; Jakubczak, P.; Abrahamian, J. F.; Faheem, S. A.; Willis, R. R. Virtual High Throughput Screening Confirmed Experimentally: Porous Coordination Polymer Hydration. *J. Am. Chem. Soc.* **2009**, *131*, 15834–15842.

APPENDIX B

PYRIDINE MODIFICATION OF NI/DOBDC

This appendix describes the modification of Ni/DOBDC with pyridine molecules in order to change the hydrophilic surface into a more hydrophobic surface. Ni/DOBDC has a high carbon dioxide capacity at the POI because of the unsaturated metal centers (UMCs), which interact strongly with water molecules. The idea here is to try to cover the polar UMCs with hydrophobic pyridine molecules to reduce water adsorption.

B.1 Pyridine modification and sample characterization

The regular Ni/DOBDC was sent to us by UOP in 2009. The pyridine modification procedure was adopted from the literature.[1,2] 0.8 g of Ni/DOBDC was added to a mixed solvent composed of 48 ml chloroform and 16 ml pyridine. The mixed solution then was stirred for 3 h and then let stand for 24 h in a chemical hood to synthesize the pyridine-modified Ni/DOBDC. The as-synthesized sample was filtered and dried in the hood under ambient condition for later use.

The BET surface areas and pore volumes for the pyridine-modified Ni/DOBDC and unmodified Ni/DOBDC are summarized in Table B.1. Both samples were regenerated at 100 °C for 24 h before measurement. It is clear that the BET surface area decreased from 798 m^2/g to 409 m^2/g before and after modification. The pore volume also decreases from regular Ni/DOBDC to pyridine-modified Ni/DOBDC. The decrease in surface area and pore volume may due to the blocking of pores by pyridine molecules and possibly chloroform molecules.

Table B.1: BET surface areas and porosities for Ni/DOBDC and pyridine-modified Ni/DOBDC

Sample	BET surface area (m^2/g)	Pore volume (cc/g)
Ni/DOBDC	798	0.38
Py-Ni/DOBDC	409	0.18

B.2 Water and carbon dioxide adsorption for pyridine-modified Ni/DOBDC

Carbon dioxide and water adsorption isotherms at room temperature were measured for the pyridine-modified Ni/DOBDC. The results are compared with those of the regular Ni/DOBDC in Fig. B.1 and Fig. B.2. Both the pyridine-modified and the regular sample were regenerated at 150 °C for 12 h before isotherm measurement. In Fig. B.1, the CO_2 capacity at 0.1 atm for pyridine-modified Ni/DOBDC is about 1.64 mol/kg which is 40% less than that of the regular Ni/DOBDC. This capacity loss may be caused by the decreased surface area for the pyridine-modified Ni/DOBDC. In Fig. B.2, it is clear that the pyridine-modified Ni/DOBDC adsorbs much less water than the regular Ni/DOBDC. This can be explained by the increased hydrophobicity of the pyridine-modifed Ni/DOBDC surface or the decreased surface area and pore volume. Therefore, in order to understand whether the pyridine modification can further reduce the water effect on the CO_2 adsorption in Ni/DOBDC, CO_2/H_2O mixture adsorption was studied.

The CO_2 isotherms at 25 °C for pyridine-modified Ni/DOBDC with different amounts of preloaded water are shown as Fig. B.3. Similar to the regular Ni/DOBDC, the CO_2 capacity at 0.1 atm decreased with the increase of preloaded water. However, we noticed that the CO_2 capacities at 0.1 atm for pyridine-modified Ni/DOBDC with 3.4 mol/kg and 10.0 mol/kg preloaded water are very close. This is because water adsorption in pyridine-modified Ni/DOBDC increased at a slower rate from 3.4 to 10.0 mol/kg than initially as shown in Fig. B.2. More importantly, the pyridine-

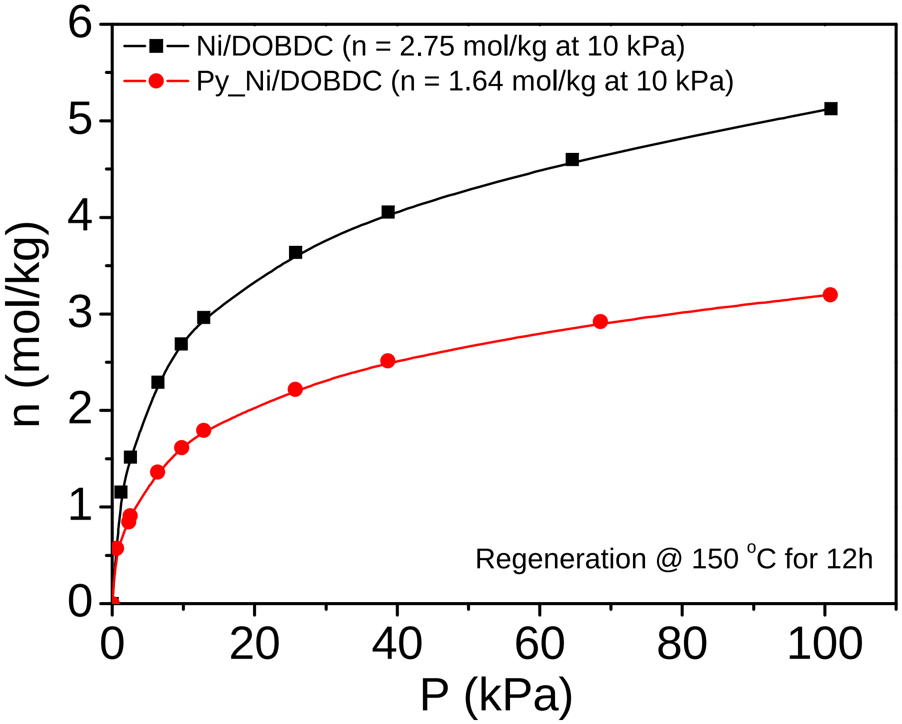

Figure B.1: CO_2 isotherms at 25 °C for Ni/DOBDC and pyridine-modified Ni/DOBDC.

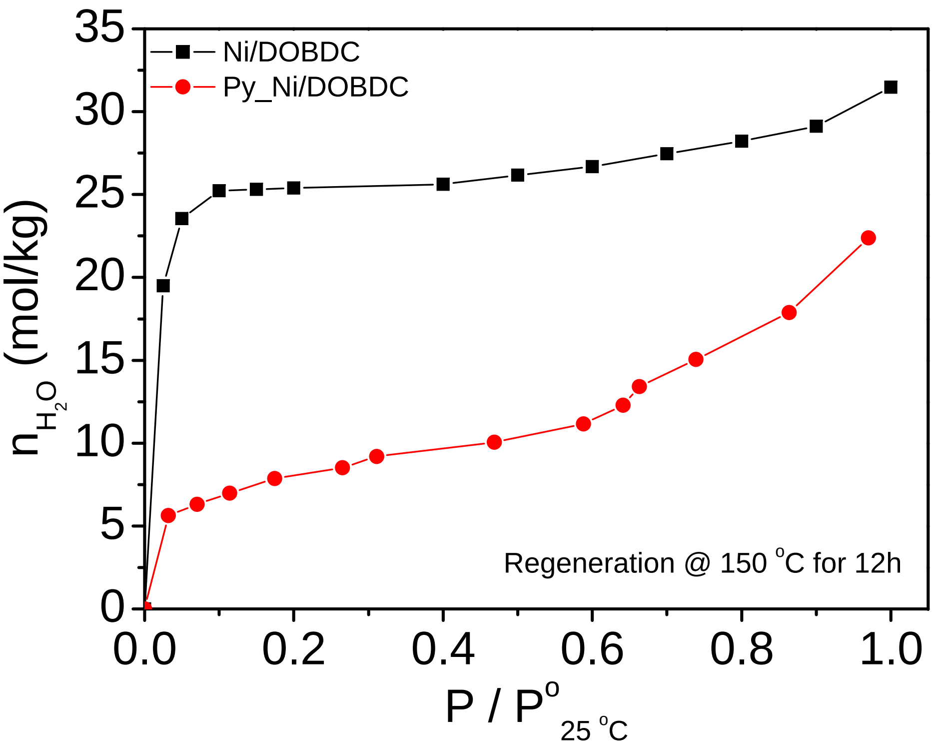

Figure B.2: H_2O isotherms at 25 °C for Ni/DOBDC and pyridine-modified Ni/DOBDC.

modified Ni/DOBDC was not at saturated with water as the regular Ni/DOBDC in the RH range from 10%-45%.

Enhancement in CO_2/N_2 selectivity has been found for a pyridine derivative modified MOF.[2] In this research, selectivities between water and carbon dioxide at 25 °C and 0.1 atm were calculated and compared for regular Ni/DOBDC and pyridine-modified Ni/DOBDC following the equation

$$S_{\mathrm{H_2O/CO_2}} = \frac{n_{\mathrm{H_2O}}/P_{\mathrm{H_2O}}}{n_{\mathrm{CO_2}}/P_{\mathrm{CO_2}}} \tag{2.1}$$

Considering the case of preloaded water at 10 mol/kg, the selectivity between water and carbon dioxide for regular Ni/DOBDC is 5260 while the selectivity between water and carbon dioxide for pyridine-modified Ni/DOBDC is 206. In addition, let us assume that a mixed gas of carbon dioxide and water with a relative humidity (RH) of 45% was flowed through an adsorption bed containing regular Ni/DOBDC or pyridine-modified Ni/DOBDC. The CO_2 capacities at 0.1 atm for regular Ni/DOBDC and pyridine-modified Ni/DOBDC are 0.10 mol/kg[3] and 0.23 mol/kg, respectively. Thus, although the loadings are fairly low, the pyridine-modified material actually has approximately double the CO_2 capacity at the same relative humidity.

In conclusion, the pyridine modification decreased the surface area and pore volume of the regular Ni/DOBDC. With no preloaded water, the pyridine-modified Ni/DOBDC has a smaller CO_2 capacity at 0.1 atm than the unmodified Ni/DOBDC and adsorbs less water compared with the unmodified sample. The selectivity between water and carbon dioxide decreases dramatically for the pyridine-modified Ni/DOBDC compared with the regular Ni/DOBDC. In addition, the CO_2 capacities for Ni/DOBDC at 0.1 atm and 45% RH were found to increase from 0.10 mol/kg to 0.23 mol/kg after pyridine modification.

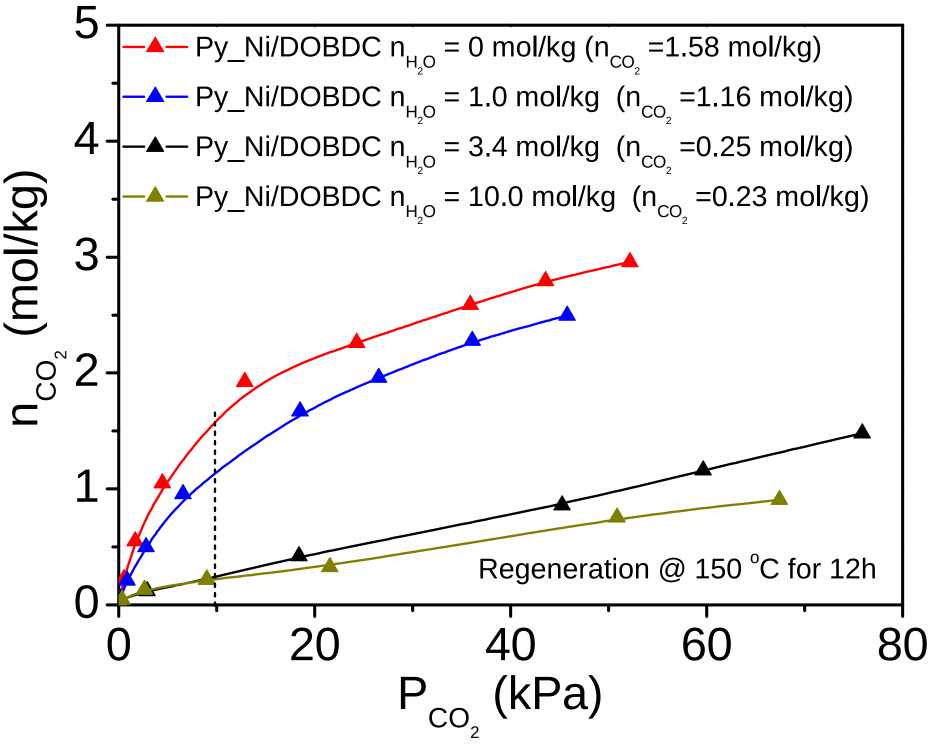

Figure B.3: CO_2 isotherms at 25 °C for pyridine-modified Ni/DOBDC with different amount of preloaded water.

References

[1] Farha, O. K.; Mulfort, K. L.; Hupp, J. T. An Example of Node-Based Postassembly Elaboration of a Hydrogen-Sorbing Metal-Organic Framework Material. *Inorg. Chem.* **2008**, *47*, 10223–10225.

[2] Bae, Y. S.; Farha, O. K.; Hupp, J. T.; Snurr, R. Q. Enhancement of CO_2/N_2 Selectivity in a Metal-Organic Framework by Cavity Modification. *J. Mater. Chem.* **2009**, *19*, 2131–2134.

[3] Liu, J.; Wang, Y.; Benin, A. I.; Jakubczak, P.; Willis, R. R.; LeVan, M. D. CO_2/H_2O Adsorption Equilibrium and Rates on Metal-Organic Frameworks: HKUST-1 and Ni/DOBDC. *Langmuir* **2010**, *26*, 14301–14307.